Quantum Many-Body Dynamics of the Bose-Hubbard System with Artificial and Intrinsic Dissipation

A dissertation submitted to the
Department of Physics of the Kyoto University

presented by
Takafumi Tomita

for the degree of
Doctor of Science

January 22, 2019

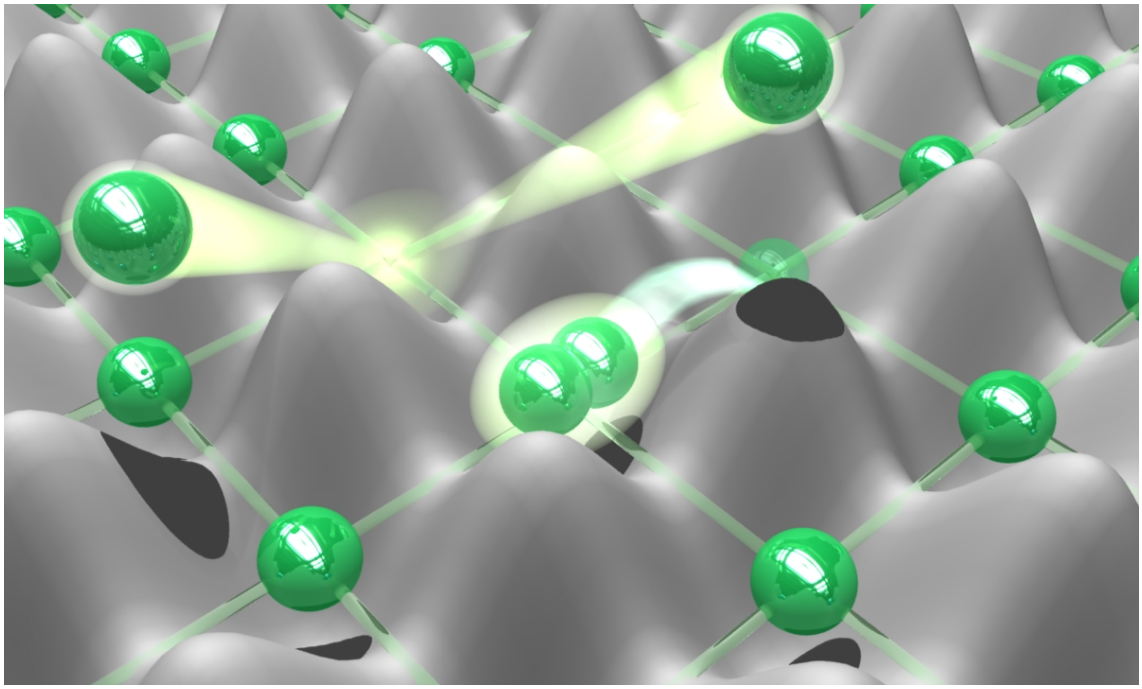

Abstract

Dissipation - coupling to the environment - is ubiquitous in nature and plays an essential role in quantum systems. It can cause decoherence of quantum states; thus, it limits the coherent dynamics. Therefore, protection of the quantum states from the coupling to the environment has been a crucial issue in quantum engineering. On the other hand, dissipation can be used as an efficient tool for the preparation and manipulation of desired quantum states. Therefore, understanding and controlling open quantum many-body systems have become increasingly important.

Thanks to their exquisite controllability, cold-atom quantum simulations have been successfully used to engineer various Hamiltonians of intensive theoretical interest. For these well-isolated and closed quantum many-body systems, various quantum phases are realized, and the transitions among those phases have been successfully observed. In addition, several recent experiments have extended the applicability of quantum simulators to Liouvillian dynamics of open quantum systems by introducing coupling to the environment, namely, dissipation.

In this thesis, we present a series of experimental studies of a Bose-Hubbard system with the dissipation of particle losses using ultracold ytterbium (Yb) atoms in a three-dimensional optical lattice. First, we report the investigation of the dissipative Bose-Hubbard system with two-body inelastic atom loss with controllable strength, which is implemented by introducing a single-photon photo-association (PA) process. The inelastic collision rate, which characterizes the strength of the dissipation, can be controlled by varying the intensity of the PA beam. In the dynamics subjected to a slow ramp-down of the optical lattice, we find that strong on-site dissipation favors the Mott insulating state: the melting of the Mott insulator is delayed, and the growth of the phase coherence is suppressed by the strong dissipation. This can be understood as the quantum Zeno effect, that is, the strong dissipation suppresses the unitary dynamics of the system. The highly controllable dissipation allows us to study the quench dynamics for investigating non-equilibrium quantum dynamics. The experimental results are compared with theoretical analysis and numerical calculation, which quantitatively capture the novel behavior presented in the experiments.

Second, we report the realization of a dissipative Bose-Hubbard system with Yb atoms in the metastable $^3P_2$ state. Because the collision between two metastable atoms induces a change of the internal degrees of freedom, the Yb atoms in the $^3P_2$ state have an intrinsically large inelastic collision rate, which induces dissipation. We fully characterize the system by measuring the scattering length between two $^3P_2$ atoms by developing a new scheme called the double excitation method. In a three-dimensional optical lattice, we investigate the atom loss behavior with the unit-filling Mott insulator as the initial state and find that the atom loss is suppressed by the strong correlation between atoms.

Also, as we decrease the potential depth of the lattice, we observe the growth of the phase coherence and find that the formation of a sizable phase coherence is suppressed by the dissipation.

Contents

Chapter 1

Introduction

1.1 Background of dissipative quantum systems

Dissipative processes are always present in nature. Any realistic system is subjected to a coupling to the environment, which influences the system in a non-negligible way. On the one hand, dissipation causes decoherence of quantum states; thus, it limits the coherent dynamics. Along with the recent growth of artificial quantum systems, especially quantum technologies for storing and manipulating quantum information [1, 2, 3, 4], protection of the quantum states from coupling to the environment has been a crucial issue. On the other hand, the dissipation can be used as an efficient tool for preparation and manipulation of particular quantum states of interest [5, 6]. One of the most primitive examples is optical pumping in atomic physics [7, 8], in which atoms are driven into a desired state with high fidelity using laser driving and spontaneous emission processes. This has led to techniques for high-precision state control for quantum computing with trapped ions [9], which utilize the driving and emission processes for sideband cooling and high-fidelity detection. Such driving processes have been extended to algorithmic cooling in nuclear magnetic resonance (NMR) systems [10, 11], which reduces the entropy of the spins via interaction with the environment to obtain a large number of highly polarized spins.

In recent years, various kinds of quantum systems, including atomic, molecular, and optical (AMO) systems, have been applied to the study of many-body physics, and it has become important to extend previous understanding of open system dynamics in single- and few-body systems to many-body systems. In particular, understanding and controlling non-equilibrium dynamics of correlated quantum many-body systems with dissipation are indeed an imperative issue shared in common among experimental systems in diverse areas of physics. The coherent dynamics competes with various types of dissipative processes, such as particle losses and photon scattering, in many-body systems with ultracold gases [5, 6, 12] and trapped ions [13, 14]. Cavity QED systems are strongly influenced by dissipative coupling to the vacuum modes of the electromagnetic field environment [12, 15]. In the system of an exciton-polariton BEC, the dynamics of a driven-dissipative polariton condensate under an incoherent pumping has been studied [12, 16]. Superconducting circuits offer open quantum systems due to photon leakage and qubit dissipation [17]. In Ref. [18], observation of a dissipative phase transition in microcavity arrays coupled with superconducting qubits was reported.

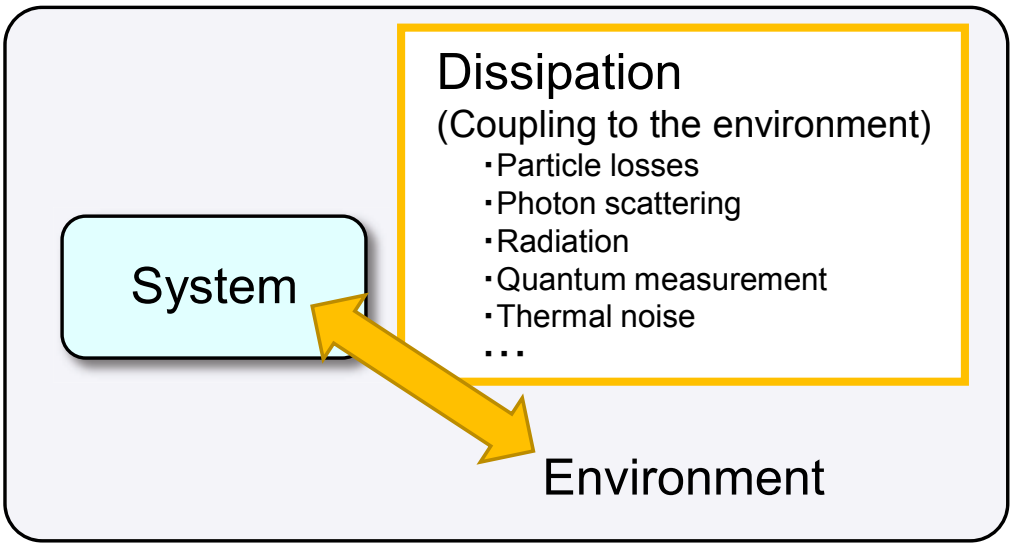

Figure 1.1.1: Schematic of a dissipative (open quantum) system. A quantum system couples to the environment, which leads to the non-unitary dynamics of the system. The quantum state of the system can be controlled by appropriate design of the coupling between the system and the environment.

Along with the development of the experimental study of quantum systems, theoretical treatment for describing the dynamics of open quantum systems has been investigated. The most common approach to describe open quantum systems is the Lindblad master equation [19], which is widely used for the treatment of irreversible and non-unitary processes from the dissipative process and decoherence to the measurement process. As a means of numerically simulating the dynamics of open quantum systems, quantum trajectory techniques have been developed in the field of quantum optics [20, 21, 22, 23, 24, 25] and can be applied to any system where the dynamics is described via the Lindblad master equation. In these techniques, the dynamics is written as a stochastic average over individual trajectories, which can evolve numerically as pure states. The assumptions in the derivation of the master equation, the Born-Markov approximation and the rotating wave approximation, restrict the use of the Lindblad master equation to quantum systems weakly coupled to large reservoirs. While the dynamics of open quantum systems can be described with the Markov approximation in many cases, there are some cases where a large separation between the system and environment timescales can no longer be assumed, leading to non-Markovian behavior. Thus, various techniques have been developed for non-Markovian open quantum systems [26].

The non-unitary dynamics of open quantum systems can be treated by an effective description based on non-Hermitian Hamiltonians under appropriate conditions [22, 5, 27]. For example, a system continuously monitored and conditioned on a null-measurement outcome obeys the dynamics described by a non-Hermitian Hamiltonian [28]. Recently, quantum many-body dynamics in a non-Hermitian Hamiltonian interacting system has been explored [28, 29, 30]. In particular, a system with parity-time ($\mathcal{PT}$) symmetry, which emerges $\mathcal{PT}$-symmetry breaking associated with an exceptional point, has been

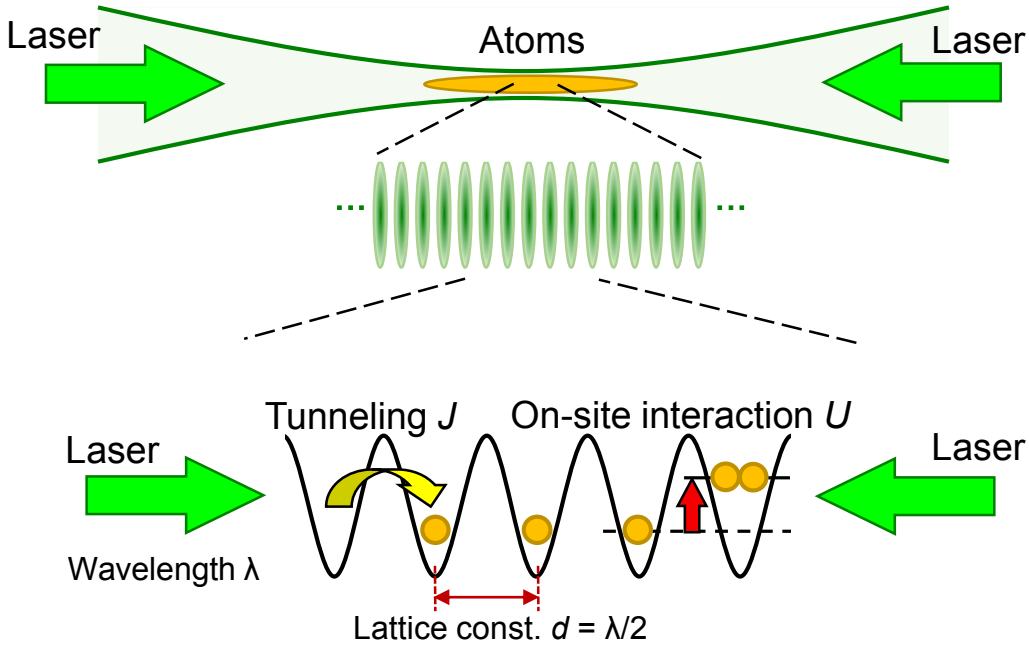

Figure 1.2.1: Schematic of an optical lattice. A periodic potential is generated by counter-propagating laser beams. Because of the interference between two beams with a wavelength of λ, an optical standing wave with a period of $\lambda/2$ is formed, in which atoms are trapped. The dynamics of the ultracold atoms in the optical lattice is well described by the Hubbard model, which consists of the tunneling of atoms between sites with amplitude J and the on-site interaction between atoms at the same site U.

intensively studied [27, 29, 31].

1.2 Quantum simulation with ultracold atoms in an optical lattice

Since the first experimental realization of a Bose-Einstein condensate (BEC) in 1995 [32, 33, 34] and the Fermi degeneracy in 1999 [35], extensive studies have been carried out on ultracold atomic gases. In particular, ultracold quantum gases in an optical lattice provide a unique platform for quantum simulation of strongly correlated quantum many-body systems. In 1998, it was pointed out that the ultracold atoms in an optical lattice accurately implement the Hubbard model [36] (Fig. 1.2.1). The superfluid-to-Mott insulator quantum phase transition was observed [37] for the Bose-Hubbard model in 2002, which demonstrated the ability of a cold-atom quantum simulator with optical lattices. This experiment promoted a series of further experimental studies with interacting bosons [38, 39, 40, 41].

While quantum degeneracy of neutral atoms was first realized with alkali atoms, many other elements have now been brought to quantum degeneracy. Among others, much attention has been paid to alkaline-earth-like (AEL) atoms, such as calcium (Ca), strontium

(Sr), and ytterbium (Yb), which have two valence electrons. Two-electron atoms have emerged as a promising tool in the quantum simulation framework because of their rich internal structure, which can be used to expand the range of possibilities offered by alkali atoms. One of the most important properties of AEL atoms is the presence of the long-lived, electronically excited metastable states $^3P_0$ and $^3P_2$. The transitions connecting these states from the ground $^1S_0$ state is extremely narrow, associated with lifetimes on the order of tens of seconds. Such ultranarrow transitions allow us to realize an optical lattice clock [42] and occupancy-sensitive high-precision spectroscopy [43]. In the field of quantum information processing, various kinds of quantum computing platforms using the metastable states for storing and controlling the quantum state have been proposed [44, 45, 46, 47, 48, 49, 50]. With the interaction between the $^1S_0$ state and the $^3P_0$ state, a two-orbital system is a promising candidate for quantum simulation of the Kondo effect [51, 52, 53, 54, 30] and the scattering properties between the $^1S_0 - ^3P_0$ states have been intensively investigated [55, 56, 57, 58, 59, 60]. Between the $^1S_0$ state and the $^3P_2$ state, Feshbach resonances have been observed [61, 62] and a spin-orbit coupling was implemented [63], which are key ingredients for novel quantum simulations.

1.3 Quantum simulation for open quantum many-body systems

The wide variety of achievements of quantum simulation with ultracold atoms are based on the unique feature that the system is well isolated from the environment. However, several recent experiments have extended the applicability of quantum simulators to Liouvillian dynamics of open quantum systems by introducing coupling to the environment, namely, dissipation. So far, various kinds of theoretical works on the effect of dissipation have predicted novel quantum states engineered by dissipation resulting from photon scattering and particle loss [64, 65, 66, 67, 68, 69, 70, 71, 72, 73, 28].

Pioneering experimental work was reported in Ref. [74], in which a two-body inelastic collision was realized using the intrinsic nature of molecules of ^{87}Rb. In this study, it was revealed that strong inelastic collisions inhibit particle losses because of the quantum Zeno effect [75]. While this study did not approach control of the dissipation strength, suppression of loss was observed in Ref. [76] by controlling the inelastic collision rate via varying the confinement, namely, the lattice depth. One-body dissipation has been introduced in a controlled manner with several methods. The utility of an electron beam has been demonstrated in Ref. [77, 78, 79]. With a well-designed photon scattering process, measurement backaction on the many-body state [80] has been invesitgated. In the case of the three-body loss process, controlling the strength of three-body recombination by Feshbach resonance and realization of a novel metastable many-body state have been demonstrated [81]. While these experiments are basically described by few-body physics, investigations of the effect of dissipation on many-body physics have been recently reported in the context of the study of many-body localization (MBL). In Ref. [82], the thermalization dynamics in the presence of controlled dissipation was explored in a MBL system. Also, the robustness of MBL in the presence of a quantum bath was investigated [83]. These experiments show the potential of the ultracold-atom system for studying open quantum many-body systems with controlled coupling to the environment.

Table 1.3.1: List of realized dissipation with ultracold gases.

Dissipation	Implementation	Group	Year	Ref.
One-body loss	Applying a localized electron beam to the BEC	H. Ott University of Kaiserslautern	2013	[77]
			2015	[78]
			2016	[79]
One-body loss Position measurement	Photon-scattering	I. Bloch MPQ	2017	[82]
Position measurement	Photon-scattering via lattice imaging technique	M. Vengalattore Cornell University	2015	[80]
Two-body loss	Inelastic collision between $^{87}Rb_2$ molecules	G. Rempe MPQ	2008	[74]
Two-body loss	Inelastic collision between KRb molecules	J. Ye NIST	2013	[76]
Two-body loss	Inelastic collision between ^{174}Yb atoms via photoassociation	This work	2017	[84]
Two-body loss	Inelastic collision between ^{174}Yb atoms in the $^3P_2$ state	This work	2018	[85]
Two-body loss	Inelastic collision between ^{173}Yb atoms in the $^3P_0$ state	K. Sengstock Univeristy of Hamburg	2018	[86]
Three-body loss	Three-body recombination by the Feshbach resonance	H.-C. Nägerl University of Innsbruck	2012	[81]
Interaction with a bath	Interaction between two components	I. Bloch MPQ	2018	[83]

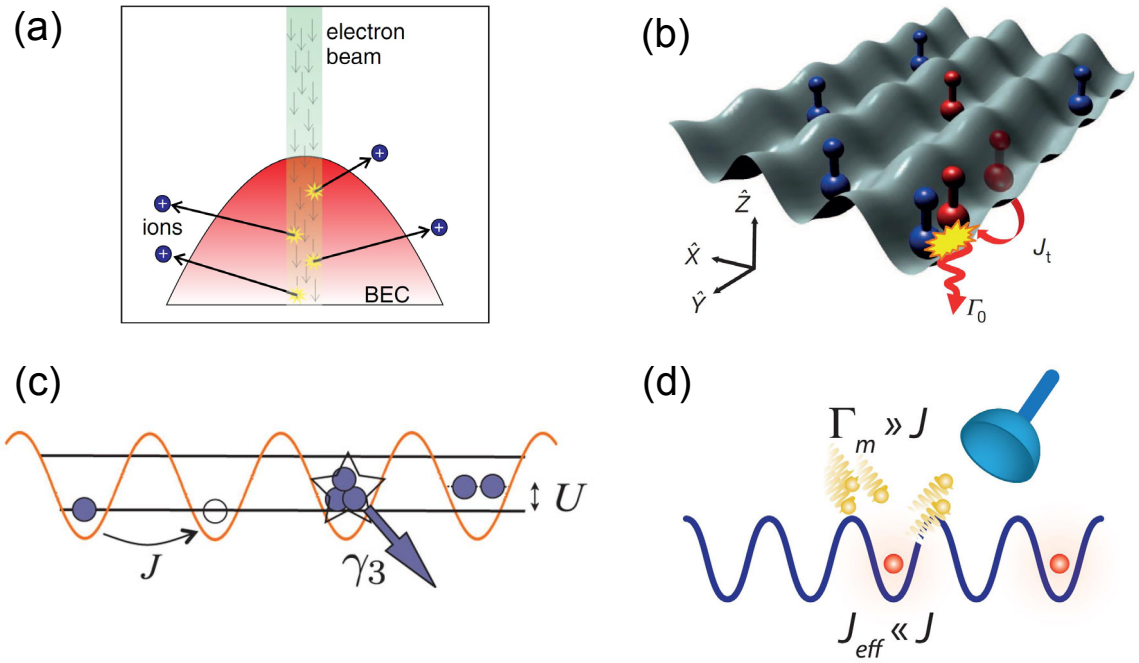

Figure 1.3.1: Dissipation implemented in quantum many-body systems with ultracold gases. (a) Localized electron beam applied to a BEC. Figure adapted from Ref. [77]. (b) Two-body inelastic collision between polar molecules in an optical lattice. Figure adapted from Ref. [76]. (c) Three-body recombination in an optical lattice. Figure adapted from Ref. [87]. (d) Position measurement via photon scattering. Figure adapted from Ref. [80].

Different from these rather artificial ways of introducing dissipation, a system of two-electron atoms naturally realizes a dissipative system because of the intrinsic strong inelastic collisions in the metastable $^3P_2$ state [88, 89, 90, 91] and the $^3P_0$ state [89, 92, 93, 94] of AEL atoms. Because the collision between two metastable atoms induces a change in the internal degrees of freedom, the atoms in the metastable state have an intrinsic large inelastic collision rate, which induces dissipation. In the case of the $^3P_0$ state of ^{173}Yb, a novel quantum state was observed in the atom loss behavior, which is consistent with the generation of a highly entangled Dicke state [86].

1.4 This thesis

In this thesis, we present a series of experiments with a Bose-Hubbard system with artificial and intrinsic two-body dissipation (Fig. 1.4.1). Because the two-body interaction is fundamental and crucial for the emergence of novel quantum states and many-body physics such as quantum phase transitions, it is important to investigate the effect of two-body dissipation on quantum many-body systems such that the strength of dissipation can be widely controlled.

First, we report an investigation of a Bose-Hubbard system using ultracold atoms in a three-dimensional (3D) optical lattice, in which we introduce engineered dissipation of the two-body particle losses. By exploiting the highly controllable nature of the dissipation

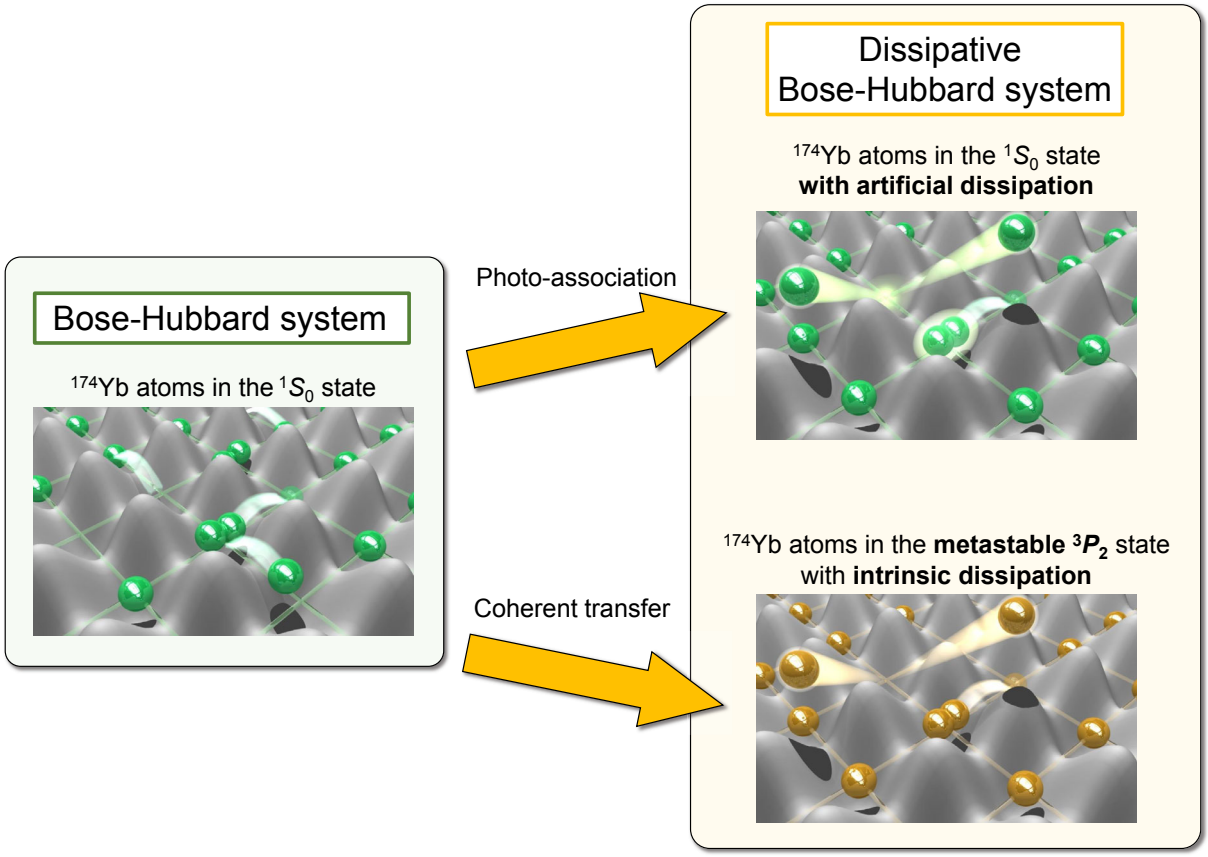

Figure 1.4.1: Schematic of our work. We realize a dissipative Bose-Hubbard system in two different manners: introducing artificial dissipation via the photo-association technique (upper right) and coherently transferring the internal state of the atoms into the metastable $^3P_2$ state (lower right).

that we introduce, we successfully reveal the effect of the dissipation on the quantum phase transition from a Mott insulator to a superfluid state in a systematic manner. In particular, in the ramp-down dynamics across the crossover from the Mott insulator to the superfluid states, we observe that the melting of the Mott state is delayed and the growth of the phase coherence is suppressed because of the strong dissipation. The highly controllable on-site dissipation allows us to study the quench dynamics as a novel method of initial state preparation, providing a new way to investigate non-equilibrium quantum dynamics.

Second, we report an experimental study of the dynamics of the dissipative $^3P_2$ state of bosonic ytterbium atoms ^{174}Yb in an optical lattice. We fully characterize the system by measuring the scattering length between two $^3P_2$ atoms by developing the double-excitation method. To overcome the difficulty of forming a BEC in the dissipative metastable state, we first create a BEC in the ground state $^1S_0$ and form a unit-filling Mott insulator in the 3D optical lattice. Then, we coherently transfer the Mott insulator in the $^1S_0$ state into the $^3P_2$ state, resulting in the successful formation of the Mott insulator in the dissipative $^3P_2$ state. With this Mott insulator as an initial state, we investigate the stability of the system and find that the atom loss is suppressed by the

strong correlation, which is attributed to both the on-site interaction and the inelastic loss. Also, this novel scheme for initial state preparation enables us to observe the growth of the phase coherence as we decrease the lattice depth, otherwise impossible to create, and we quantitatively reveal that the formation of a sizable phase coherence is suppressed by the dissipation.

Outline

This thesis is organized as follows.

- Chapter 2 introduces theoretical background for the dissipative Bose-Hubbard system.
- Chapter 3 gives the details of our experimental apparatus and procedures used for dissipative Bose-Hubbard experiments with ytterbium atoms.
- Chapter 4 reports a series of experiments with the dissipative Bose-Hubbard system with artificial dissipation induced by photo-association. We present the result of the investigation of the effect of the dissipation on the quantum phase transition of the Bose-Hubbard system.
- Chapter 5 describes the dissipative Bose-Hubbard system with intrinsic dissipation with the metastable state of the ytterbium atoms.
- Chapter 6 briefly summarizes the works presented in this thesis and provides some directions for future studies.

Chapter 2

Theoretical background

In this chapter, we introduce the theoretical background for a dissipative Bose-Hubbard system. First, we briefly summarize a band structure in an optical lattice. Then, we introduce the Bose-Hubbard model and describe the quantum phase transition between the superfluid state and the Mott insulating state. In Section 2.3, we present the theoretical treatment of dissipative systems. Finally, we describe the theory of photo-association.

2.1 Ultracold atoms in an optical lattice

An optical lattice offers a unique platform for quantum simulation of quantum many-body physics. It is generated by interfering counter-propagating laser beams, which form a standing wave of light. Using a laser far-detuned from atomic resonances, atoms feel an optical dipole force proportional to the intensity of the laser. Therefore, the standing wave of light creates the perfect periodic potential.

A three-dimensional (3D) cubic lattice is constructed using the three one-dimensional lattices orthogonal to each other. When the wavelength of the lattice beam is λ, the lattice potential is expressed as:

$$V_L(x) = -(V_{0x}\cos^2(k_L x) + V_{0y}\cos^2(k_L y) + V_{0z}\cos^2(k_L z)) \tag{2.1.1}$$

where $k_L = 2\pi/\lambda$ is the wavevector of the lattice and $V_{0\alpha}$ $(\alpha = x, y, z)$ is the potential depth of each axis. The lattice spacing d is half of the lattice wavelength $d = \lambda/2$. The lattice depth is often expressed with units of recoil energy $E_R = \hbar^2 k_L^2/2m$, where m is the atomic mass. It is convenient to describe the lattice depth V_0 by the reduced lattice depth parameter $s = V_0/E_R$.

2.1.1 Bloch bands

For simplicity, we first consider the one-dimensional system. The state of a single particle in the optical lattice is given by the Schrödinger equation:

$$\hat{H}\psi_q^{(n)}(x) = E_q^{(n)}\psi_q^{(n)}(x), \tag{2.1.2}$$

where $\hat{H}$ is the Hamiltonian

$$\hat{H} = \frac{\hat{p}^2}{2m} + V(x), \tag{2.1.3}$$

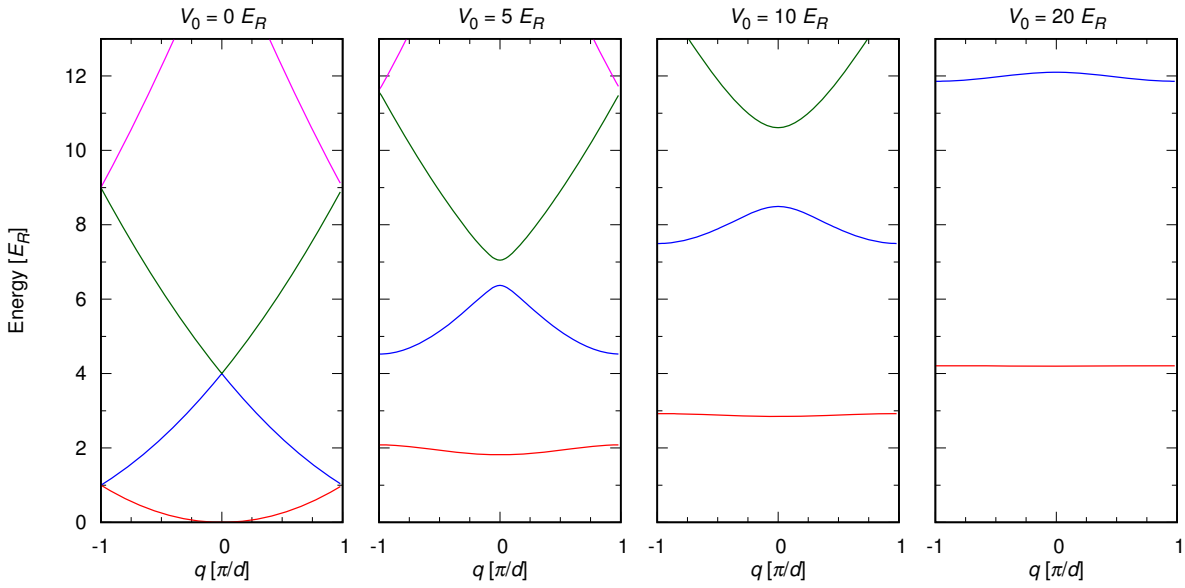

Figure 2.1.1: Band structure for one-dimensional lattice at lattice depths of $V_0 = 0, 5, 10, 20 E_R$.

where $V(x)$ is a periodic potential $V(x) = V(x + d)$ with lattice spacing d.

The solutions of this equation are the so-called Bloch function, which, according to Bloch's theorem, can be written as the product of a plane wave and a function with the same periodicity as the potential

$$\psi_q^{(n)}(x) = e^{iqx} u_q^{(n)}(x), \tag{2.1.4}$$

where

$$u_q^{(n)}(x + d) = u_q^{(n)}(x). \tag{2.1.5}$$

Introducing Eq. (2.1.4) into Eq. (2.1.3) leads to the Schrödinger equation for $u_q^{(n)}(x)$:

$$\left[\frac{(p + \hbar q)^2}{2m} + V(x)\right] u_q^{(n)}(x) = E_q^{(n)} u_q^{(n)}(x) \tag{2.1.6}$$

where q is the quasi-momentum of the state and n is the band index.

The band structure can be obtained by expressing the periodic functions $V(x)$ and $u_q^{(n)}$ in the form of a Fourier sum

$$V(x) = \sum_l V_l e^{i2k_L lx}, \tag{2.1.7}$$

$$u_q^{(n)}(x) = \sum_l c_l^{(n,q)} e^{i2k_L lx}. \tag{2.1.8}$$

The potential of the optical lattice can be written as

$$V(x) = -V_{0x}\cos^2(k_L x) = -\frac{V_{0x}}{4}(e^{i2k_L lx} + e^{-i2k_L lx} + 2). \tag{2.1.9}$$

Thus, we obtain

$$\sum_{l'} H_{i,i'}^{(q)} c_{l'}^{(n,q)} = E_q^{(n)} c_l^{(n,q)}, \tag{2.1.10}$$

where

$$H_{ll'}^{(q)} = E_R \times \begin{cases} (2l + q/k_L)^2 + s/2 & l = l', \\ s/4 & |l - l'| = 1, \\ 0 & \text{otherwise.} \end{cases} \tag{2.1.11}$$

The eigenenergies and eigenstates can be obtained by diagonalizing each submatrix $H^{(q)}$. Figure 2.1.1 shows the band structure for a one-dimensional lattice with various lattice depths.

2.1.2 Wannier state

We express the state localized at each lattice site by transforming the Bloch state.

$$|i, n\rangle = \frac{1}{\sqrt{N_{\text{site}}}} \sum_q e^{-iqx_i} |q, n\rangle, \tag{2.1.12}$$

where x_i is the position of the lattice site i.

The Wannier function is represented by

$$w_n(x - x_i) = \langle x|i, n\rangle = \frac{1}{\sqrt{N_{\text{site}}}} \sum_q e^{-iqx_i} \psi_q^{(n)}(x). \tag{2.1.13}$$

Wannier functions obey the orthonormality relation for all bands n and sites i. In a deep lattice, the lattice potential can be approximated by a harmonic potential with the frequency $\hbar\omega_{\text{lat}} = 2\sqrt{s}E_R$. Also, the Wannier function for the lowest band can be approximated to the following Gaussian function:

$$w_0(x - x_i) \simeq \left(\frac{m\omega_{\text{lat}}}{\pi\hbar}\right)^{1/4} \exp\left[-\frac{m\omega_{\text{lat}}}{2\hbar}(\boldsymbol{r} - \boldsymbol{r_i})^2\right]. \tag{2.1.14}$$

However, the harmonic oscillator approximation is not suited for typical experimental parameters, as shown in Fig. 2.1.2. The true Wannier function decays exponentially rather than in a Gaussian manner and always has nodes to guarantee the orthogonality relation. Thus, the harmonic oscillator approximation should not be used for the calculation of Hubbard parameters, especially inter-site quantities such as the tunneling amplitude.

In a 3D lattice system, the Wannier function is simply extended to

$$w_{n_x,n_y,n_z}(\boldsymbol{r} - \boldsymbol{r_i}) = w_n(x - x_i) w_n(y - y_i) w_n(z - z_i). \tag{2.1.15}$$

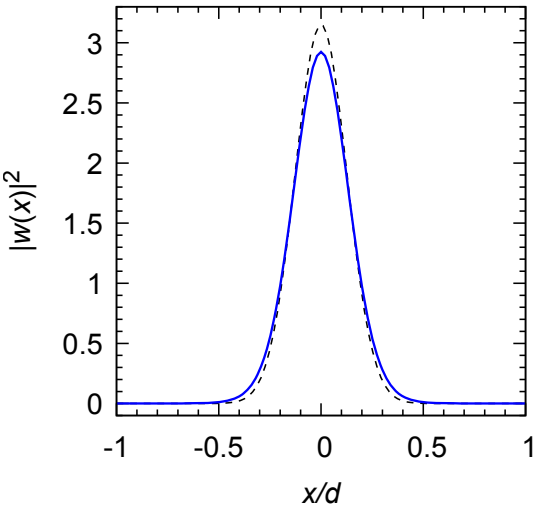

Figure 2.1.2: Wannier function for the lowest band at a lattice depth of $V_0 = 10E_R$. The dashed line represents the result of harmonic approximation Eq. (2.1.14).

2.2 Bose-Hubbard model

Here, we consider the many-body physics of bosonic atoms in an optical lattice $V_L(\boldsymbol{r})$. We start from the many-body Hamiltonian for bosons interacting via an interacting potential $V_{\text{int}}(\boldsymbol{r}-\boldsymbol{r'})$

$$\hat{H} = \int d\boldsymbol{r}\hat{\Psi}^\dagger(\boldsymbol{r})\left(-\frac{\hbar^2\nabla^2}{2m} + V_L(\boldsymbol{r})\right)\hat{\Psi}(\boldsymbol{r}) + \frac{1}{2}\int d\boldsymbol{r}d\boldsymbol{r'}\hat{\Psi}^\dagger(\boldsymbol{r})\hat{\Psi}^\dagger(\boldsymbol{r'})V_{\text{int}}(\boldsymbol{r}-\boldsymbol{r'})\hat{\Psi}(\boldsymbol{r})\hat{\Psi}(\boldsymbol{r'}) \tag{2.2.1}$$

where $\hat{\Psi}^\dagger(\boldsymbol{r})$ and $\hat{\Psi}(\boldsymbol{r})$ are creation and annihilation operators, respectively, of bosonic atoms at position $\boldsymbol{r}$ and satisfy the commutation relation

$$\left[\hat{\Psi}(\boldsymbol{r}), \hat{\Psi}^\dagger(\boldsymbol{r'})\right] = \delta(\boldsymbol{r}-\boldsymbol{r'}). \tag{2.2.2}$$

At sufficiently low temperature, the interaction between atoms are dominated by s-wave collision. In such a situation, the asymptotic scattering wavefunction resulting from the true interaction potential can be reproduced by the following delta-function contact potential:

$$V_{\text{int}}(\boldsymbol{r}-\boldsymbol{r'}) = \frac{4\pi\hbar^2 a}{m}\delta(\boldsymbol{r}-\boldsymbol{r'}), \tag{2.2.3}$$

where a is the s-wave scattering length.

Below, we consider the lowest band $n = 0$ and use the Wannier function for the lowest band: $w(\boldsymbol{r}-\boldsymbol{r_i}) = w_0(\boldsymbol{r}-\boldsymbol{r_i})$. Because the Wannier function for all sites $\boldsymbol{r}_i$ forms a complete basis, the annihilation operator $\hat{\Psi}(\boldsymbol{r})$ can be expanded in the form

$$\hat{\Psi}(\boldsymbol{r}) = \sum_{n,i} w(\boldsymbol{r}-\boldsymbol{r_i})\hat{a}_i. \tag{2.2.4}$$

Here, $\hat{a}_i$ is the annihilation operator for particles at the lattice site i, which satisfies the commutation relation

$$\left[\hat{a}_i, \hat{a}_j^\dagger\right] = \delta_{i,j}. \tag{2.2.5}$$

For a deep lattice, the dominant terms are given by the nearest neighbor tunneling process and the on-site interaction. Finally, we obtain the Hamiltonian [95, 96, 36]

$$\hat{H} = -J\sum_{\langle i,j\rangle}(\hat{a}_i^\dagger \hat{a}_j + \text{h.c.}) + \frac{U}{2}\sum_i \hat{n}_i(\hat{n}_i - 1) + \sum_i(\epsilon_i - \mu)\hat{n}_i. \tag{2.2.6}$$

Here, we add the confining potential ϵ_i and the chemical potential μ.

The on-site interaction U is given by

$$U = \frac{4\pi\hbar^2 a}{m}\int d\boldsymbol{r}|w(\boldsymbol{r} - \boldsymbol{r_i})|^4 \tag{2.2.7}$$

The tunneling amplitude between nearest neighboring sites i and j is given by

$$J = -\int d\boldsymbol{r} w^*(\boldsymbol{r} - \boldsymbol{r_i})\left(-\frac{\hbar^2\nabla^2}{2m} + V_L(\boldsymbol{r})\right)w(\boldsymbol{r} - \boldsymbol{r_j}). \tag{2.2.8}$$

For a deep optical lattice, these parameters have the approximate expression

$$U \simeq \sqrt{\frac{8}{\pi}}kaE_R\left(\frac{V_{0x}V_{0y}V_{0z}}{E_R^3}\right)^{3/4}, \tag{2.2.9}$$

$$J_\alpha \simeq \frac{4}{\sqrt{\pi}}\left(\frac{V_{0\alpha}}{E_R}\right)^{3/4}\exp\left[-2\left(\frac{V_{0\alpha}}{E_R}\right)^{1/2}\right], \tag{2.2.10}$$

where J_α ($\alpha = x, y, z$) is the tunneling amplitude along the α axis. We note that these expressions should not be used in the experimental regime such as $V_0 < 30E_R$. Instead, we use numerically calculated U and J for the analysis.

2.2.1 Quantum phase transition of the Bose-Hubbard system

The important property of the Bose-Hubbard model is the existence of a quantum phase transition between a superfluid phase and a Mott insulator phase [96] at the critical point $(J/U)_c$. We discuss the limiting cases, which describe the two possible phases in the ground state of the Bose-Hubbard model.

Superfluid state

In the non-interacting limit $U/J = 0$, the ground state is a Bose-Einstein condensate (BEC) where all N atoms are in the $\boldsymbol{q} = \boldsymbol{0}$ in the lowest Bloch band

$$|\Psi\rangle_{U/J=0} = \frac{1}{\sqrt{N!}}\left(\frac{1}{\sqrt{N_L}}\sum_i \hat{a}_i^\dagger\right)^N|0\rangle, \tag{2.2.11}$$

where N_L is the number of lattice sites. In particular, in a large system and a large particle-number limit, the ground state cannot be distinguished from a product of coherent states

$$|\Psi\rangle_{U/J=0} \propto \prod_i\left[\exp\left(\sqrt{\frac{N}{N_L}}\hat{a}_i^\dagger\right)|0\rangle_i\right]. \tag{2.2.12}$$

As a result, the on-site number probability distribution follows a Poisson distribution.

In the three-dimensional system, the ground state has long-range phase coherence, namely, the condensate has the same phase everywhere and the first-order correlator $\langle\hat{a}_i^\dagger\hat{a}_j\rangle$ remains finite as $|i - j| \to \infty$.

Mott insulating state

In the limit of zero tunneling $J/U = 0$, the tunneling term can be neglected and the ground state is given by

$$|\Psi\rangle_{J/U=0} = \left[\prod_i \frac{1}{\sqrt{m!}}(\hat{a}_i^\dagger)^m\right]|0\rangle, \tag{2.2.13}$$

where m is the occupation number. For a given chemical potential μ, the occupation number m is determined by minimizing the energy. As a result, $m_i(\mu)$ has a step-wise dependence on μ, where $m_i(\mu)$ increases by one at integer values of μ/U, resulting in the imcompressibility $\partial n/\partial\mu = 0$ in the region, where μ takes non-integer values. Low-energy excitation consists of a particle-hole pair, and this leads to the excitation gap of U, which is called the Mott gap.

In an experimental situation, the harmonic trap potential modifies the chemical potential. Thus, the Mott insulating state forms a wedding-cake-shaped number distribution (Fig. 2.2.1 (b)).

Mean field analysis

Between these two situations, there is a quantum phase transition at $J/U = (J/U)_c$, where the excitation gap closes. Here, we describe the phase boundary between the superfluid state and the Mott insulating state within a mean field approximation [96, 97, 98]. We expand the bosonic operator as $\hat{a}_i = \psi + (\hat{a}_i - \psi)$ and neglect the higher-order terms of $(\hat{a}_i - \psi)$. Here, $\psi = \langle\hat{a}_i\rangle$ is called the superfluid order parameter. We assume that ψ is real and the system is homogeneous. Under these approximations, the Hamiltonian Eq. (2.2.6) becomes

$$H_{\mathrm{MF}} \simeq JzN_L\psi^2 + \frac{U}{2}\sum_i \hat{n}_i(\hat{n}_i - 1) - \mu\sum_i \hat{n}_i - Jz\psi\sum_i(\hat{a}_i + \hat{a}_i^\dagger), \tag{2.2.14}$$

where N_L is the number of lattice sites and z is the coordination number.

For sufficiently small J, we can apply a perturbation expansion to the second order. The ground state energy E_0 is given by

$$E_0/N_L = Jz\psi^2 + \frac{U}{2}m(m-1) - \mu m - (Jz\psi)^2\left[\frac{m}{U(m-1)-\mu} - \frac{m+1}{Um-\mu}\right], \tag{2.2.15}$$

where m is the occupation number. If the second-order coefficient of J is positive, the energy E_0 is minimized for $\psi = 0$, which corresponds to the Mott insulating state. Conversely, if the second-order coefficient is negative, the energy is minimized for $\psi \neq 0$, corresponding to the superfluid state. Thus, the phase transition occurs at the point where

$$Jz + (Jz)^2\left[\frac{m}{U(m-1)-\mu} - \frac{m+1}{Um-\mu}\right] = 0 \tag{2.2.16}$$

Figure 2.2.1 shows the phase diagram for the superfluid - Mott insulator transition obtained by mean field analysis.

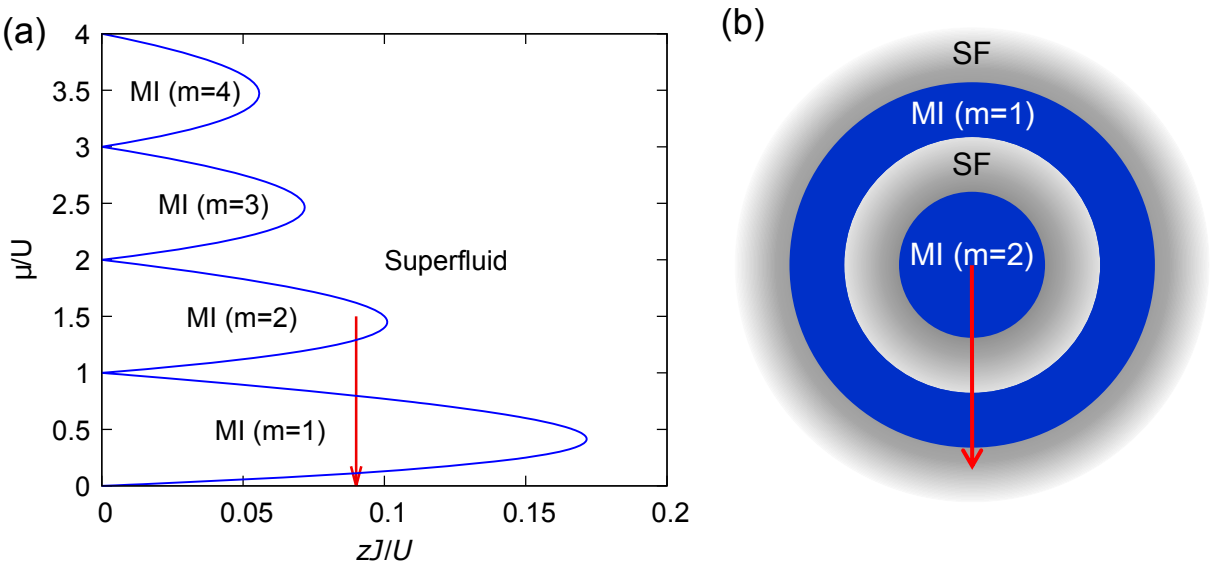

Figure 2.2.1: (a) Phase diagram for the superfluid - Mott insulator (MI) transition obtained by mean field analysis. (b) Mott shell structure of the atoms in the optical lattice with the harmonic trap potential. In a real experiment in which the external harmonic trap is superimposed on an optical lattice, the local chemical potential takes a spatially dependent value, with the result that a series of Mott insulator and superfluid regions appears on going toward the edge of the cloud, as indicated by the red arrow.

The experimentally observed critical point corresponds to the tip of the Mott lobe, that is, the point at which the following conditions are satisfied:

$$\frac{\partial}{\partial \mu}\left(\frac{Jz}{U}\right)_c = 0. \tag{2.2.17}$$

From this condition, we obtain the critical point:

$$\left(\frac{zJ}{U}\right)_c = 1 + 2m - 2\sqrt{m^2+m}. \tag{2.2.18}$$

For the singly occupied state $m = 1$, $(zJ/U)_c = 3 - 2\sqrt{2} \simeq 0.1716$, which is first obtained in Ref. [96]. Conversely, for a quantum Monte-Carlo calculation of the phase diagram yield for the $m = 1$ state and a 3D cubic lattice ($z = 6$),r the result $(zJ/U)_c = 0.2045$ [99], which means that the mean field analysis underestimates the critical point.

Experimental observation of the superfluid-Mott insulator transition

The superfluid - Mott insulator transition in an optical lattice was first experimentally observed in Ref. [37] by detecting the sudden disappearance of the long-range phase coherence in a three-dimensional optical lattice. This is done by observing multiple matter-wave interference pattern of atoms after free expansion of the atoms, which is the so-called Time-of-Flight (TOF) method, and the vanishing of the interference when increasing the interaction. The transition can also be observed by adiabatically ramping down the lattice

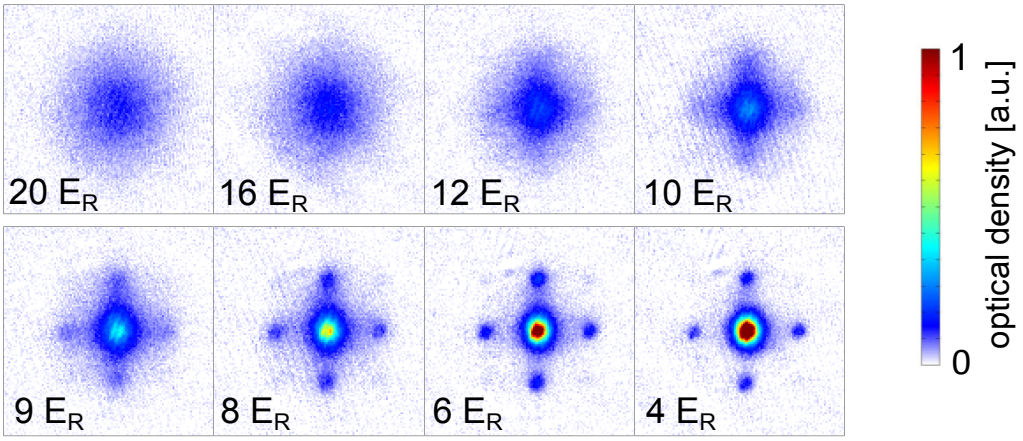

Figure 2.2.2: Absorption images of the multiple matter-wave interference patterns of ^{174}Yb atoms after a TOF of 8 ms. We ramp down the lattice adiabatically from 20 E_R.

after preparing the Mott insulting state, with the result that the Mott insulator is melted and the phase coherence grows, as shown in Fig. 2.2.2.

When the lattice depth is deep and the interaction can be neglected, the density distribution $n(\boldsymbol{r}, t)$ after the TOF can be expressed as [100, 101]

$$n(\boldsymbol{r}, t) = \left(\frac{m}{\hbar t}\right)^3 \left|\tilde{w}\left(\frac{m\boldsymbol{r}}{\hbar t}\right)\right|^2 \mathcal{S}\left(\boldsymbol{k} = \frac{m\boldsymbol{r}}{\hbar t}\right), \tag{2.2.19}$$

where $\tilde{w}(\boldsymbol{k})$ is the Fourier transform of the Wannier function, which determines the envelope of the density distribution and

$$\mathcal{S}(\boldsymbol{k}) = \sum_{i,j} \exp\left[i\boldsymbol{k} \cdot (\boldsymbol{r_i} - \boldsymbol{r_j})\right] \langle \hat{a}_i^\dagger \hat{a}_j \rangle \tag{2.2.20}$$

describes the quasimomentum distribution characterizing the phase coherence, that is, the interference pattern of the TOF absorption image.

More detailed properties, such as critical exponents [41] and a non-local order in a 1D lattice [102], have been investigated previously.

2.3 Description of the dissipative system

The unitary dynamics of a quantum system is given by the von Neumann equation in the Schrödinger picture

$$\frac{d\hat{\rho}}{dt} = -\frac{i}{\hbar}\left[\hat{H}, \hat{\rho}\right], \tag{2.3.1}$$

where $\hat{H}$ is a Hamiltonian of the system and $\hat{\rho}$ is a density matrix. However, it does not include irreversible processes such as spontaneous emission, particle losses, and the measurement process, all of which are described by non-unitary processes. This generally occurs in the treatment of open quantum systems: systems coupled to the environment that we do not track. Here, we discuss the theoretical treatment of open quantum systems.

2.3.1 Master equation in Lindblad form

To derive an equation of motion for the behavior of a system in the presence of dissipation resulting from the coupling to the environment, we make three approximations. By considering the total system including the interaction between the system and the environment and then eliminating the degrees of freedom of the environment under the approximations, we obtain a master equation.

The first approximation is that the frequency scale associated with the dynamics induced by the system-environment coupling is small compared with the relevant system and environment dynamical frequency scale. In other words, the coupling between the system and the environment is so weak that the influence of the system on the environment is small. This assumption is called the *Born approximation*.

We also assume that the environment returns rapidly to equilibrium in a manner essentially unaffected by its coupling to the system, so that the environment is unchanged in time, and the dynamics of the system is not affected by its coupling to the environment at earlier times, which means that the time evolution of the system does not depend on the history of the system. This assumption is called the *Markov approximation*.

Finally, we assume that the terms that are oscillating much faster than the system frequency scale are neglected. This assumption is called the *Rotating wave approximation*.

With these assumptions, the dynamics of the system in the presence of dissipation resulting from the coupling to the environment is described by the master equation in Lindblad form [19]:

$$\frac{d\hat{\rho}}{dt} = -\frac{i}{\hbar}[\hat{H}, \hat{\rho}] + \frac{1}{2}\sum_j \gamma_j(-\hat{L}_j^\dagger \hat{L}_j \hat{\rho} - \hat{\rho}\hat{L}_j^\dagger \hat{L}_j + 2\hat{L}_j \hat{\rho} \hat{L}_j^\dagger). \tag{2.3.2}$$

Here, operators $\hat{L}_j$ are called Lindblad operators and describe the dissipative dynamics that occur at the rates γ_j.

The approximations for the derivation of the Eq. (2.3.2) are justified in our experiment because the environment consists of a continuum of modes that quickly dephase. As a result, the environment returns to the vacuum state on a time scale that is much faster than all time scales in the system of interest.

Strictly speaking, the system Hamiltonian $\hat{H}$ is in general modified compared with the unperturbed system Hamiltonian resulting from the coupling between the system and the environment [103]. In our study, which focuses on the two-body inelastic collision, calculation of the value of the shift is difficult because of the complexity of the collision channels [104]. This modification of the Hamiltonian is beyond the scope of our work.

We can rewrite Eq. (2.3.2) as follows:

$$\frac{d\hat{\rho}}{dt} = -\frac{i}{\hbar}(\hat{H}_{\text{eff}}\hat{\rho} - \hat{\rho}\hat{H}_{\text{eff}}^\dagger) + \sum_j \gamma_j \hat{L}_j \hat{\rho} \hat{L}_j^\dagger, \tag{2.3.3}$$

where

$$\hat{H}_{\text{eff}} = H - \frac{i}{2}\sum_j \gamma_j \hat{L}_j^\dagger \hat{L}_j \tag{2.3.4}$$

is the non-Hermitian effective Hamiltonian. The last term of Eq. (2.3.3) is often called the *quantum jump term* or *recycling term*, as it represents stochastic quantum jumps and recycles the population that is lost from certain states caused by the non-Hermitian effective

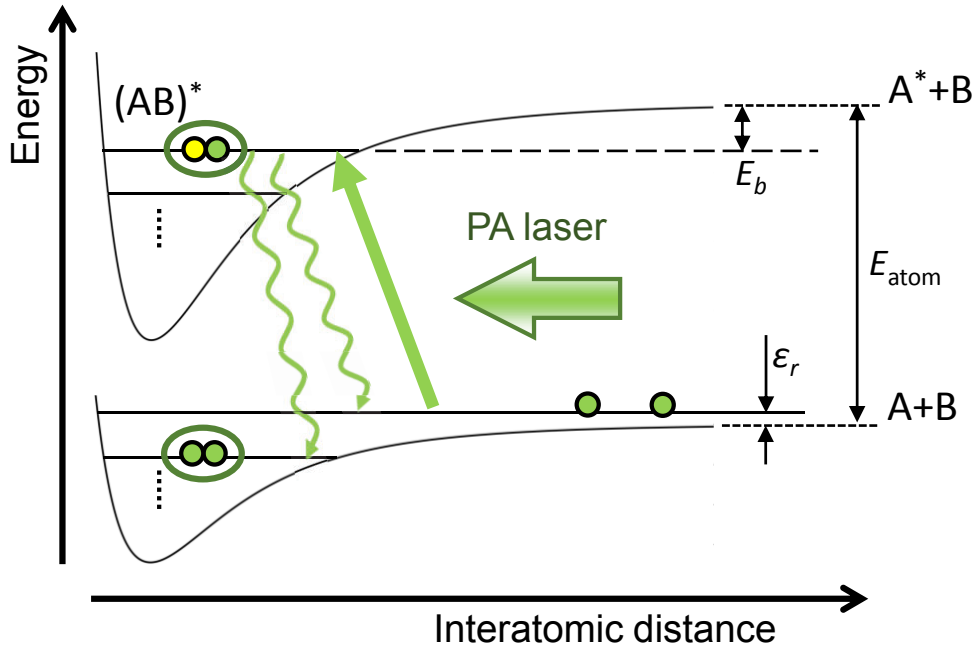

Figure 2.4.1: Schematic of the PA process. Two potential energy curves are shown as a function of the interatomic distance. ε_r is the relative kinetic energy. E_{atom} is the energy required to excite one atom (here, atom A), and E_b is the binding energy of the molecular vibrational level.

Hamiltonian, placing it in other states. The quantum jump term can be neglected under an appropriate condition [22, 5, 27], and the dynamics of the system can be described by the non-Hermitian Hamiltonian. For example, the system continuously monitored and conditioned on a null-measurement outcome obeys the dynamics described by the non-Hermitian Hamiltonian [28]. In the description of the Kondo effect in an ultracold-atom system considering the loss of impurities, the dynamics around a surviving impurity is described by the non-Hermitian Kondo Hamiltonian [30].

2.4 Photo-association

To implement the two-body inelastic atom loss with controllable strength, we introduce a single-photon photo-association process for ultracold Yb atoms in a 3D optical lattice. Here we describe the general theory of photo-association.

Photo-association (PA) [105, 106, 107, 108, 109] is the process in which two colliding atoms absorb a photon to form an electronically excited molecule [110]:

$$A + B + \gamma \rightarrow (AB)^*. \tag{2.4.1}$$

The molecules formed by the PA process immediately dissociate into the electronically ground molecular state or two ground-state atoms.

2.4.1 Photo-association rate

Here, we describe the rate of the PA process, which is a key parameter for engineering the dissipation in our experiment.

The PA rate coefficient has the following form [111, 112, 113, 110]:

$$K_{\mathrm{PA}} = \frac{\pi\hbar}{\mu k_r}\sum_l (2l+1)\frac{\hbar(\Gamma_{\mathrm{nat}}+\Gamma_o)\hbar\Gamma_b(\varepsilon_r,l)}{[\varepsilon_r + h\nu - h\nu_0 - S_b(\varepsilon_r)]^2 + (\hbar\Gamma_{\mathrm{tot}}/2)^2}. \tag{2.4.2}$$

Here, μ is the reduced mass, k_r is the wave number of the relative motion, $\varepsilon_r = (\hbar k_r)^2/2\mu$ is the relative kinetic energy, and l is the total angular momentum of the two-atom system. The bound state has a finite linewidth

$$\Gamma_{\mathrm{tot}} = \Gamma_{\mathrm{nat}} + \Gamma_b(\varepsilon_r, l) + \Gamma_o. \tag{2.4.3}$$

Γ_{nat} is the natural linewidth of the excited state. $\Gamma_b(\varepsilon_r, l)$ represents the stimulated decay into the entrance channel, which is given in the two-state approximation by

$$\Gamma_b(\varepsilon_r, l) = 2\pi|V_b(\varepsilon_r, l)|^2. \tag{2.4.4}$$

$V_b(\varepsilon_r, l)$ is the optical coupling strength between the bound state $|b\rangle$ and the collisional state $|\varepsilon_r, l\rangle$:

$$V_b(\varepsilon_r, l) = \sqrt{\frac{2\pi I}{c}}\,\langle b|\,\boldsymbol{d}\cdot\boldsymbol{e}\,|\varepsilon_r, l\rangle\,, \tag{2.4.5}$$

where $\boldsymbol{e}$ is the polarization vector of the PA light with intensity I, c is the speed of light, and $\boldsymbol{d}$ is the molecular electric dipole moment. Γ_o is the decay rate caused by any other processes that lead to decay of the bound state. ν is the PA laser frequency, and $\nu_0 = (E_{\mathrm{atom}} - E_b)/h$ (see Fig. 2.4.1) is the energy difference between the excited bound state and the ground collisional state. $S_b(\varepsilon_r)$ is the light shift of the resonance position given by

$$S_b(\varepsilon_r) = \sum_{l'}\mathcal{P}\int\frac{|V_b(\varepsilon_r', l')|^2}{\varepsilon_r - \varepsilon_r'}d\varepsilon_r', \tag{2.4.6}$$

where $\mathcal{P}$ is a partial part integral over the continuum $\varepsilon_r' > 0$ and a summation over the discrete bound state for $\varepsilon_r' < 0$. In the experiment, the effect of the intensity-dependent shift is kept small by tuning the laser frequency to the peak of the line:

$$\varepsilon_r + h\nu - h\nu_0 - S_b(\varepsilon_r) = 0. \tag{2.4.7}$$

When we consider only the s-wave scattering under sufficiently low temperature and assume that $\Gamma_{\mathrm{nat}} \gg \Gamma_o$, Eq. (2.4.2) can be written as

$$K_{\mathrm{PA}} = \frac{4\pi\hbar}{\mu} l_{\mathrm{opt}}(I, \varepsilon_r)\frac{1}{2}\frac{(\hbar\Gamma_{\mathrm{nat}})^2}{[\varepsilon_r + h\nu - h\nu_0 - S_b(\varepsilon_r)]^2 + (\hbar\Gamma_{\mathrm{nat}}/2)^2}, \tag{2.4.8}$$

where

$$l_{\mathrm{opt}}(I, \varepsilon_r) \equiv \frac{\Gamma_b(\varepsilon_r, l=0)}{2k_r\Gamma_{\mathrm{nat}}} \tag{2.4.9}$$

is the optical length [114, 110], which is independent of the collisional energy in the regime $\varepsilon_r \to 0$ and varies linearly with the intensity I. The optical length characterizes

the strength of an optical Feshbach resonance, namely, the ability of light to change the scattering length of ground state atoms as follows [114, 110]:

$$a = a_{\mathrm{bg}} + l_{\mathrm{opt}}(I, \varepsilon_r)\frac{[\varepsilon_r + h\nu - h\nu_0 - S_b(\varepsilon_r)](\hbar\Gamma_{\mathrm{nat}})}{[\varepsilon_r + h\nu - h\nu_0 - S_b(\varepsilon_r)]^2 + (\hbar\Gamma_{\mathrm{nat}}/2)^2}, \tag{2.4.10}$$

where a and a_{bg} are the scattering length in the presence of light and the background scattering length, respectively.

From Eq. (2.4.8), K_{PA} in the resonance condition $\varepsilon_r + h\nu - h\nu_0 - S_b(\varepsilon_r) = 0$ is represented as

$$K_{\mathrm{PA}} = \frac{8\pi\hbar}{\mu} l_{\mathrm{opt}}(I, \varepsilon_r). \tag{2.4.11}$$

Specifically, when two atoms have the same mass ($\mu = m/2$), K_{PA} is written as

$$K_{\mathrm{PA}} = \frac{16\pi\hbar}{m} l_{\mathrm{opt}}(I, \varepsilon_r). \tag{2.4.12}$$

For the ${}^1S_0 - {}^3P_1$ PA lines between the homonuclear bosonic isotopes of Yb, which are used in our experiment, the optical lengths can be systematically calculated [115, 116]. Thus we can estimate the PA rate via Eq. (2.4.12). The details are described in Section 3.5.1.

Chapter 3

Experimental setup

In this chapter, we describe the experimental setup and procedure for producing quantum degenerate gases of ytterbium in optical lattices. First, the general properties of Yb atoms are introduced, followed by cooling processes. The excitation to the metastable state is described in Section 3.4. As for probing, we use absorption imaging and fluorescence imaging, as described in Section 3.6.

3.1 Properties of Ytterbium (Yb)

3.1.1 Isotopes and scattering lengths

Ytterbium (Yb) is a rare-earth metal in the Lanthanide series. There are seven stable isotopes of Yb: five bosons (^{168}Yb, ^{170}Yb, ^{172}Yb, ^{174}Yb, ^{176}Yb), and two fermions (^{171}Yb, ^{173}Yb). The natural abundance and nuclear spin of the stable isotopes are shown in Table 3.1.1. After the first realization of a BEC of ^{174}Yb in 2003 [117], BECs of ^{170}Yb, ^{176}Yb, and ^{168}Yb and Fermi degeneracies of ^{173}Yb and ^{171}Yb have been realized [118, 119, 120, 121]. Because ^{172}Yb has a large negative scattering length, a BEC of ^{172}Yb cannot be stable. In addition, various kinds of quantum gas mixtures of Yb isotopes have been realized [119, 122], which open up new quantum phases.

Table 3.1.1: Natural abundance and nuclear spin of Yb atom [123]

Isotope	Natural abundance [%]	Nuclear spin [$\hbar$]
^{168}Yb	0.13	0
^{170}Yb	3.05	0
^{171}Yb	14.3	1/2
^{172}Yb	21.9	0
^{173}Yb	16.1	5/2
^{174}Yb	31.8	0
^{176}Yb	12.7	0

Table 3.1.2: s-wave scattering lengths for combinations of Yb isotopes in [nm] unit [127]

	^{168}Yb	^{170}Yb	^{171}Yb	^{172}Yb	^{173}Yb	^{174}Yb	^{176}Yb
^{168}Yb	**13.33**	6.19	4.72	3.44	2.04	0.13	-19.0
^{170}Yb		**3.38**	1.93	-0.11	-4.30	-27.4	11.08
^{171}Yb			**−0.15**	-4.46	-30.6	22.7	7.49
^{172}Yb				**−31.7**	22.1	10.61	5.62
^{173}Yb					**10.55**	7.34	4.22
^{174}Yb						**5.55**	2.88
^{176}Yb							**−1.28**

Because of the differences in the reduced mass, each isotopic combination of Yb has a different s-wave scattering length. The scattering length between two ground $^1S_0$ state atoms has been precisely measured via photo-association (PA) spectroscopy [124, 125, 126] and estimated for all pairs of isotopes using the mass scaling law [127], as shown in Table 3.1.2.

3.1.2 Energy level

The ground-state electronic configuration [1] is [Xe] $4f^{14}6s^2$. The electronic structure is determined by the two valence electrons in the 6s-shell; thus, it is similar to that of alkaline-earth metals. These two electrons arrange a spin singlet with total spin $S = 0$ or a spin triplet with total spin $S = 1$, which forms two manifolds and a transition. Figure 3.1.1 is a diagram of the low-lying energy levels of Yb used for experiments in this thesis.

3.1.3 Transition properties

We describe the properties of important transitions used in our experiments.

$^1S_0 \leftrightarrow {}^1P_1$ (399 nm)

The $^1S_0 \leftrightarrow {}^1P_1$ is a strong electric dipole (E1) transition whose natural linewidth is 29 MHz. The wavelength of the transition is 398.9 nm. This transition is used for Zeeman slowing, absorption imaging, fluorescence imaging, and atom blast. This transition is essentially cyclic, with a very small branching ratio of roughly 10^{-7} to the $^3D_1$ and $^3D_2$ states [128].

$^1S_0 \leftrightarrow {}^3P_1$ (556 nm)

The $^1S_0 \leftrightarrow {}^3P_1$ is an intercombination transition whose natural linewidth is 182 kHz, and the wavelength of the transition is 555.8 nm. The transitions between two separate

[1] $1s^2 2s^2 2p^6 3s^2 3p^6 3d^{10} 4s^2 4p^6 4d^{10} 5s^2 5p^6 4f^{14} 6s^2$

Table 3.1.3: Basic properties of the ${}^1S_0 \leftrightarrow {}^1P_1$ and ${}^1S_0 \leftrightarrow {}^3P_1$ transitions [129, 130, 131].

Parameter		${}^1S_0 \leftrightarrow {}^1P_1$	${}^1S_0 \leftrightarrow {}^3P_1$	Unit
wavelength	λ	398.9	555.8	nm
Lifetime	τ	5.5	873	ns
Linewidth	$\frac{\Gamma}{2\pi} = \frac{1}{2\pi\tau}$	29	0.182	MHz
Saturation intensity	$I_s = \frac{\pi h c \Gamma}{3\lambda^3}$	59	0.139	mW/cm^2
Recoil energy	E_R/k_B	344	178	nK
Recoil velocity	$v_R = \frac{\hbar k}{m}$	5.73	4.13	μm/ms
Doppler cooling limit	$T_D = \frac{\hbar\Gamma}{2k_B}$	690	4.37	μK

spin manifolds are forbidden as electric dipole (E1) transitions in the pure LS-coupling scheme because of the spin selection rule $\Delta S = 0$. However, the heavy atom is not accurately described by the LS-coupling scheme, and the spin-orbit interaction mixes some ${}^1P_1$ wavefunction into the wavefunction for the term that has been labelled ${}^3P_1$. This transition is used for the magneto-optical trap (MOT) and the PA.

The basic properties of the ${}^1S_0 \leftrightarrow {}^1P_1$ and ${}^1S_0 \leftrightarrow {}^3P_1$ transitions are described in Table 3.1.3.

${}^1S_0 \leftrightarrow {}^3P_2$ (507 nm)

The ${}^1S_0 \leftrightarrow {}^3P_2$ is an ultranarrow transition whose wavelength is 507.4 nm. In the bosonic isotopes, this line is a magnetic quadrupole (M2) transition whose natural linewidth is 10.6 mHz [132], i.e., the lifetime of the ${}^3P_2$ state is 15 s. We note that in the case of fermionic isotopes, the linewidth of this transition is expected to be slightly broader than that of bosonic isotopes because of the hyperfine mixing effect (Table 3.1.4). The ultranarrow transition enables occupancy-sensitive high-resolution spectroscopy [43]. The Yb atoms in the ${}^3P_2$ state have a magnetic field sensitivity with a magnetic moment of $3\mu_B$, which enables site-resolved addressing of atoms in an optical lattice with a magnetic gradient [45, 47].

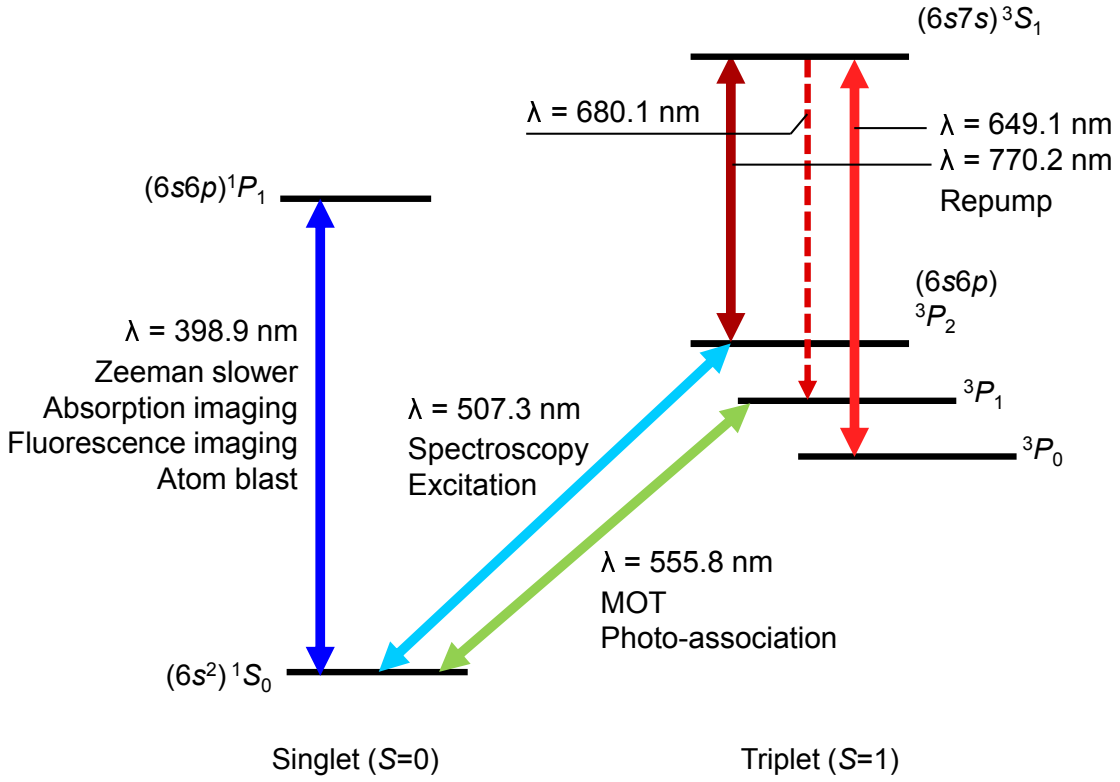

Figure 3.1.1: Low-lying energy levels of Yb and their major applications.

Table 3.1.4: Basic properties of the ${}^1S_0 \leftrightarrow {}^3P_2$ transition [132, 133].

Parameter		${}^1S_0 \leftrightarrow {}^3P_2$		Unit
		Boson	Fermion	
wavelength	λ	507.35		nm
Lifetime	τ	15	6.3 (^{171}Yb)	s
			7.2 (^{173}Yb)	s
Linewidth	$\frac{\Gamma}{2\pi} = \frac{1}{2\pi\tau}$	10.6	25 (^{171}Yb)	mHz

Table 3.1.5: Basic properties of the ${}^3P_0 \leftrightarrow {}^3S_1$, ${}^3P_1 \leftrightarrow {}^3S_1$ and ${}^3P_2 \leftrightarrow {}^3S_1$ transitions. The radiative decay rate $\Gamma^{(s)}$ is calculated from the reduced matrix elements $\langle {}^3S_1 | \, |\boldsymbol{d}| \, | {}^3P_J \rangle$ given in Ref. [132] with the relation $\Gamma^{(s)} = \omega_J^3/(9\pi\varepsilon_0\hbar c^3)| \langle {}^3S_1 | \, |\boldsymbol{d}| \, | {}^3P_J \rangle \, |^2$ [134], where $\omega_J/(2\pi)$ is the transition frequency.

Parameter		${}^3P_0 \leftrightarrow {}^3S_1$	${}^3P_1 \leftrightarrow {}^3S_1$	${}^3P_2 \leftrightarrow {}^3S_1$	Unit
wavelength	λ	649.1	680.1	770.2	nm
Radiative decay rate	$\Gamma^{(s)}$	9.7	27	38	MHz
Branching ratio		0.13	0.36	0.51	
Saturation intensity	$I_s = \dfrac{\pi hc\Gamma^{(s)}}{3\lambda^3}$	0.74	1.8	1.7	$\mathrm{mW/cm^2}$
Recoil energy	E_R/k_B	131	119	92.8	nK
Recoil velocity	$v_R = \dfrac{\hbar k}{m}$	3.53	3.37	2.98	μm/ms

${}^3P_2 \leftrightarrow {}^3S_1$ (770 nm) and ${}^3P_0 \leftrightarrow {}^3S_1$ (649 nm)

For detection of the atoms in the excited ${}^3P_2$ state, we apply a repumping laser. The atoms in the ${}^3P_2$ are repumped back to the ${}^1S_0$ state using repumping lasers of 770 nm and 649 nm, which are resonant to the ${}^3P_2 - {}^3S_1$ and ${}^3P_0 - {}^3S_1$ transitions, respectively. The ${}^3P_2$ atoms absorbing a 770-nm photon are excited to the ${}^3S_1$ state. Then, the ${}^3S_1$ atoms that decay into the ${}^3P_J$ states ($J = 0, 1, 2$). The atoms which decay to the ${}^3P_1$ state return to the ${}^1S_0$ state by emitting 556-nm photon. The atoms that decay to the ${}^3P_0$ and ${}^3P_2$ state are again excited to the ${}^3S_1$ state absorbing 649-nm and 770-nm photons, respectively (see Fig. 3.1.1). The basic properties of these transition are shown in Table 3.1.5.

3.1.4 Inelastic collisions between metastable atoms

Because collisions between two metastable atoms induces a change in the internal degrees of freedom, atoms in the metastable state have an intrinsically large inelastic collision rate. The inelastic collision rate between ^{174}Yb atoms in the ${}^3P_2$ state is measured in Ref. [91] with a thermal gas. In the measurement of the ${}^3P_2 - {}^3P_2$ inelastic collision rate at low magnetic field and low temperature, no spin dependence is observed, which is consistent with fine structure changing processes (J-changing collisions) or principal quantum number changing (PQNC) processes, rather than the m-changing collision. The

average of the inelastic collision coefficients is $\beta_{ee} = 4 \times 10^{-17}\mathrm{m}^3/\mathrm{s}$. We note that the loss rate for a BEC is reduced by a factor of 2 compared with a thermal gas because of the difference in the value of the pair correlation function.

3.2 Cooling processes

At room temperature, Yb is a solid with a low vapor pressure. To vaporize Yb, we heat the Yb oven up to approximately 400 °C. To achieve quantum degeneracy of atom gases, Yb atoms are cooled down to a few tens of nK. This is achieved by the all-optical method explained below.

3.2.1 Zeeman slower

The atoms emitted from the oven at approximately 400 °C go through a Zeeman slower, where they are decelerated by a counter-propagating laser beam. We use the ${}^1S_0 \leftrightarrow {}^1P_1$ transition with a wavelength of 399 nm. Basically, the resonance frequency of atoms in an atomic beam is shifted because of the Doppler effect, depending on the atomic velocity. In a Zeeman slower system, such frequency shifts are compensated by a gradually varied external magnetic field. We adopted a so-called "increasing field type" Zeeman slower, in which the magnetic field becomes stronger as the deceleration proceeds. The slowing laser is obtained by frequency doubling of a Ti:sapphire laser of 798 nm (MBR-110, Coherent Inc). A ring cavity with a $Ba_2B_2O_4$ (BBO) crystal is used for the second harmonic generation with an output power of 100 $\sim$ 150 mW. The laser frequency is locked to a transfer cavity (RG-91T, Burleigh Instruments Inc) stabilized by 556-nm light that is locked to a stable ultra-low expansion (ULE) cavity.

3.2.2 Magneto-Optical Trap (MOT)

Atoms slowed by the Zeeman slower are trapped in a magneto-optical trap (MOT). The MOT consists of three pairs of two counter-propagating lasers with circular polarization and a quadrupole magnetic field. We use the narrow ${}^1S_0 \leftrightarrow {}^3P_1$ intercombination transition with a wavelength of 556 nm, whose Doppler cooling limit is $T_D = 4.4\mu$K. The laser system consists of a fiber laser at 1111 nm (Boostik Y10-PM, Koheras), a ULE cavity for frequency stabilization, and a wave-guide second harmonic generator (SHG, NTT Electronics). To load atoms into a far-off resonant trap, the atomic density is increased by a compressed MOT scheme, where the magnetic field gradient is ramped up. Subsequently, the intensity and the detuning of the MOT laser are decreased for cooling. Typically, 4×10^6 ^{174}Yb atoms are captured at a loading time of 8 s, for example.

3.2.3 Far-Off Resonance Trap (FORT)

Atoms in the MOT are transferred to a far-off resonant trap (FORT) for further cooling to quantum degeneracy. This is formed by crossing two laser beams with wavelengths of 532 nm (Verdi-V10/V-18, Coherent Inc.) at their focusing points. The polarization of the two beams is the same. Evaporative cooling is performed by gradually decreasing the intensity of the two laser beams. This enables us to selectively evaporate high-velocity

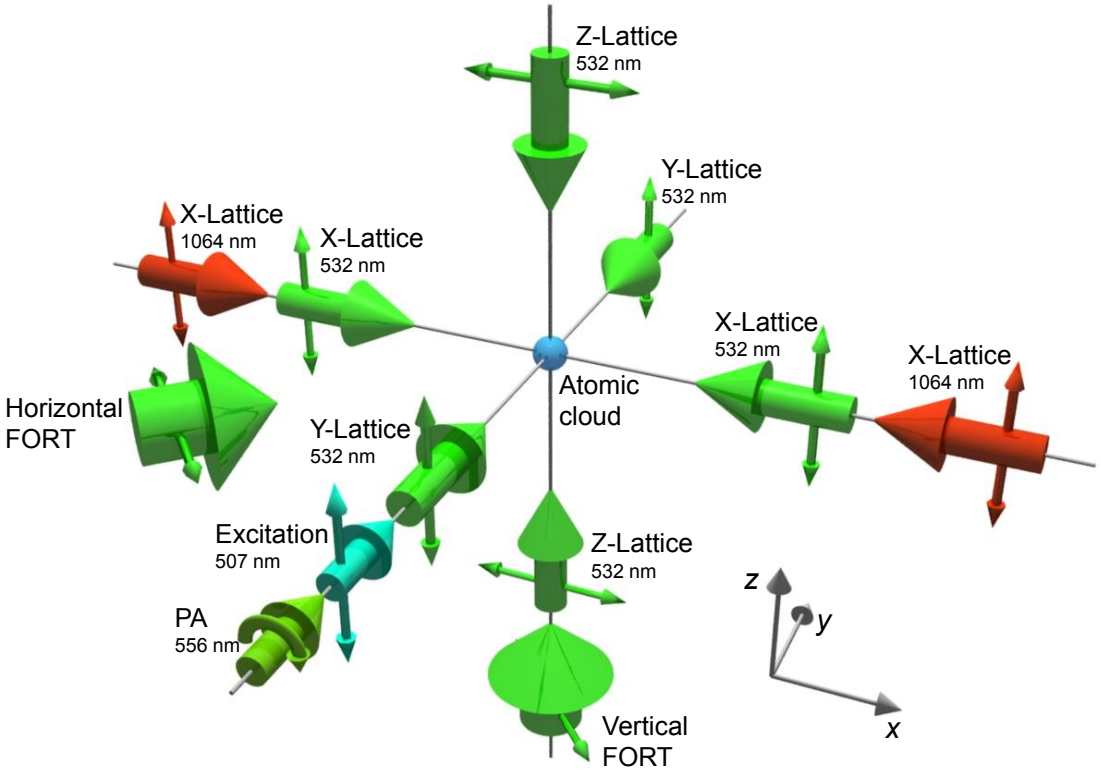

Figure 3.3.1: Schematic view of the laser configuration for the experiments. Thin arrows represent the polarization of the lasers. The magnetic field is applied along the y-axis for the PA experiment and the z-axis for excitation to the $^3P_2$ state.

atoms, which results in achieving a lower temperature for the remaining atoms. Using thees processes, we obtain quantum degenerate gases of Yb.

3.3 Optical lattice

3.3.1 532 nm lattice

Our 3D optical lattice is formed by three mutually orthogonal laser beams with wavelengths of 532 nm. The light transmitted through the acousto-optic modulator (AOM) for intensity control of the horizontal FORT is divided into three beams and used for the optical lattices. Each beam is diffracted by AOMs for intensity stabilization, and + or − 1st-order beams are coupled to the optical fibers. The laser intensity is stabilized by monitoring the laser power using photo diodes after the fibers and sending the feedback signal to the AOMs.

3.3.2 1064 nm lattice

In our experiment, a 1064-nm lattice in the x axis is used for forming an optical superlattice. Our 1064-nm lattice exists in the x, z-axis. Output from a fiber amplifier (NuAMP, Nufern) with a seed light (Mephisto S, Innolight) is divided to two beams and used for 1064-nm lattices. Each beam is diffracted by AOMs for intensity stabilization, and + or − 1st-order beams are coupled to the optical fibers. The laser intensity is stabilized by monitoring the laser power using photo diodes after the fibers and sending the feedback signal to the AOMs.

By superimposing the 1064-nm lattice onto the 532-nm lattice, we construct an optical superlattice along the x-axis, the potential of which is written as

$$V(x) = V_{1064}\cos^2(k_{1064}x) + V_{532}\cos^2(2k_{532}x + \phi) \tag{3.3.1}$$

where ϕ is the relative phase between the 1064-nm lattice and the 532-nm lattice. The details of the lock and control of the relative phase ϕ are described in Ref. [135].

3.4 Excitation

3.4.1 507-nm excitation laser

We perform the excitation from the $^1S_0$ state to the $^3P_2$ state with a laser whose wavelength is 507 nm. We generate the 507-nm light by frequency-doubling of the 1014-nm light from an external cavity laser diode (ECLD). The frequency of the 1014-nm light is first locked to a pre-stabilizer cavity and locked to a ULE cavity with a high finesse. The 1014-nm light is amplified by a tapered amplifier and 507-nm light is generated through a waveguide SHG module.

3.4.2 Adiabatic rapid passage (ARP)

To coherently transfer the atoms in the $^1S_0$ state to the $^3P_2$ state, we use adiabatic rapid passage (ARP) with a frequency-swept pulse [136]. This scheme is more robust than the π-pulse excitation with respect to the fluctuation of the frequency and the intensity of the excitation laser. Here, we briefly describe the fundamental principle of the ARP based on a two-level system.

Under the rotating wave approximation, the Hamiltonian of a two-level system coupled to a field is written as

$$\hat{H}(t) = \frac{\hbar}{2}\begin{pmatrix} -\Delta(t) & \Omega \\ \Omega & \Delta(t) \end{pmatrix}. \tag{3.4.1}$$

where $\Delta(t) = \omega(t) - \omega_0$ is the detuning and Ω is the Rabi frequency. Diagonalizing the Hamiltonian Eq. 3.4.1, we obtain the eigenvalues

$$E_+ = \frac{\hbar}{2}\sqrt{\Delta(t)^2 + \Omega^2} \tag{3.4.2}$$

$$E_- = -\frac{\hbar}{2}\sqrt{\Delta(t)^2 + \Omega^2} \tag{3.4.3}$$

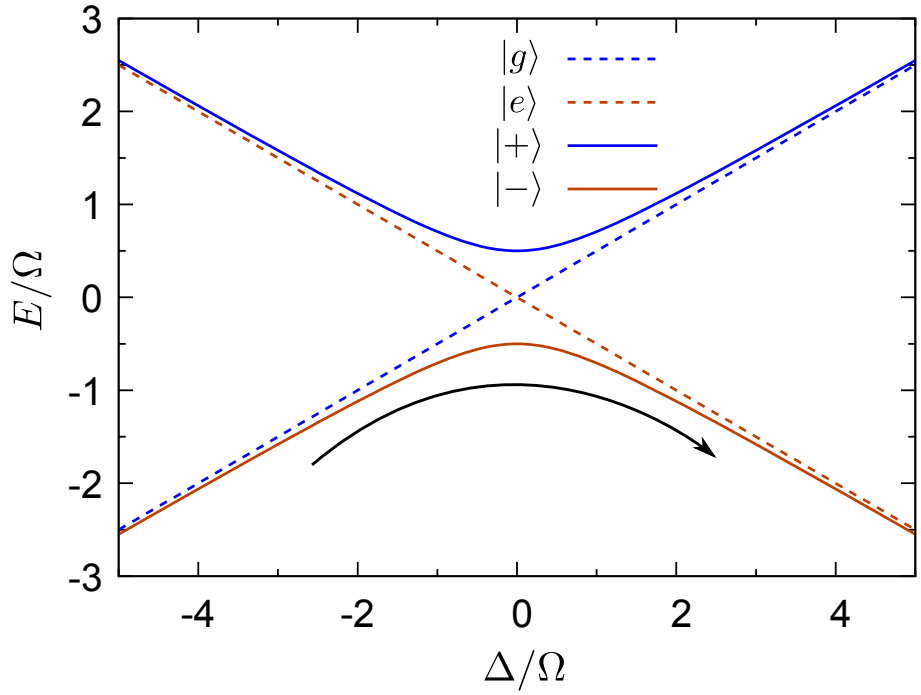

Figure 3.4.1: Energy levels as a function of detuning Δ. The solid and dashed lines represent energy levels with and without coupling Ω, respectively. By mixing the two states, the atom adiabatically passes from $|g\rangle$ to $|e\rangle$ (black arrow).

and the corresponding eigenstates

$$|+\rangle = \sin\theta(t)|g\rangle + \cos\theta(t)|e\rangle \tag{3.4.4}$$
$$|-\rangle = \cos\theta(t)|g\rangle - \sin\theta(t)|e\rangle, \tag{3.4.5}$$

where

$$\theta \equiv \arctan\left(-\frac{\Omega}{\Delta(t)}\right) \tag{3.4.6}$$

and $|g(e)\rangle$ is a bare atomic ground (excited) state.

The frequency is first tuned well below the resonance ($\Delta \ll -\Omega$) and swept through the resonance. If the process is performed adiabatically, the state is transferred into the excited state (Fig. 3.4.1). Using the Landau-Zener formula, the excited state population is given by [134]

$$P_e(t \to \infty) = 1 - \exp\left(-\frac{\pi\Omega^2}{2\left|\frac{d\Delta}{dt}\right|}\right) \tag{3.4.7}$$

in the limit $t \to \infty$. Here, we see that the entire population adiabatically follows the dressed state and makes the transition in the limit of a strong field and slow sweep ($\Omega^2 \gg |d\Delta/dt|$).

The frequency of the excitation laser is swept by controlling the RF signal for the switching AOM via the original oscillator with a voltage-controlled crystal oscillator (VCXO, NV7050SA-74.1758M, Nihon Dempa Kogyo).

3.4.3 Repumping laser

We use the $^3P_2 \leftrightarrow {}^3S_1$ transition with a wavelength of 770 nm and the $^3P_0 \leftrightarrow {}^3S_1$ transition with a wavelength of 649 nm to repump atoms in the $^3P_2$ state to the $^1S_0$ state. The 770-nm light is generated by an ECLD and locked to an ULE. The 649-nm light is generated by an ECLD and locked to the same ULE as that for the 770-nm light.

3.5 Photo-association

Photo-association (PA) is performed with the $^1S_0 \leftrightarrow {}^3P_1$ transition with a wavelength of 556 nm. We select the PA transition line with the binding energy of -3683.2 MHz. The laser system consists of a fiber laser at 1111 nm (Orange one, Menlo systems), a ULE cavity for frequency stabilization, and a wave guide SHG (NTT Electronics). To avoid splitting of the resonance, we use circularly polarized light (Fig. 3.3.1).

3.5.1 Optical lengths for the $^1S_0 - {}^3P_1$ PA lines

In Chapter 2, we introduced the optical length, which characterizes the strength of an optical Feshbach resonance and the PA rate. In our experiment, we use the $^1S_0 - {}^3P_1$ PA line to implement the dissipation.

The optical lengths for the $^1S_0 - {}^3P_1$ PA lines between the homonuclear bosonic isotopes of Yb are calculated by Ref. [115, 116], as shown in Table 3.5.1.

3.5.2 Selection of the PA transition line for artificial dissipation

To systematically investigate the effect of the dissipation on the quantum many-body physics, it is necessary to apply a wide range of dissipation strengths. Because the intensity of the PA laser that can be applied is limited, we choose the appropriate PA transition line that introduces larger inelastic collision rate.

We calculate the PA rate from the optical lengths of the molecular states [115, 116] based on Eq. 2.4.12. Figure 3.5.1 is the PA rate K_{PA}, which shows that K_{PA} is larger for smaller detuning Δ, i.e., the binding energy. However, if we choose a molecular state with a small detuning, the atoms suffer from severe photon scattering by the PA laser. We evaluate the effect of the photon scattering by dividing K_{PA} by the photon scattering rate R_{ph}, which reveals that the molecular state of the vibrational quantum number of $v' = 16$ with the detuning $\Delta/h = -3683.2$ MHz of ^{174}Yb is the most appropriate except for the states of ^{168}Yb and ^{172}Yb. ^{168}Yb and ^{172}Yb are not appropriate for our experiment because of the small abundance and the negative scattering length, respectively.

In the calculation from the optical length, K_{PA} of the molecular state of the vibrational quantum number of $v' = 16$ with the detuning $\Delta/h = -3683.2$ MHz of ^{174}Yb is 2.12×10^{-11} cm^{3}s^{-1} for the intensity of 1 W/cm^2. We note that the one-body loss caused by photon scattering can be neglected with respect to this transition because the detuning is much larger than the natural linewidth of the atomic transition.

Table 3.5.1: Optical lengths $l_{\text{opt}}(I = 1\ \text{W/cm}^2, \varepsilon_r \to 0)$ for the $^1S_0 - {}^3P_1$ PA lines as a function of the binding energy E_b for the bosonic isotopes of Yb [115, 116]. a_0 is the Bohr radius.

^{168}Yb		^{170}Yb		^{172}Yb		^{174}Yb		^{176}Yb	
E_b/h [MHz]	l_{opt}/a_0	E_b/h [MHz]	l_{opt}/a_0	E_b/h [MHz]	l_{opt}/a_0	E_b/h [MHz]	l_{opt}/a_0	E_b/h [MHz]	l_{opt}/a_0
-1.4	425489.9	-1	1037724.1	-0.7	3989748.7	-1.6	563800.5	-1.1	1118874.8
-3.9	96663	-2.9	286922.6	-2.2	1439663	-4.2	163715.1	-3.1	344375.7
-9.3	23168.4	-7.2	95071.4	-5.5	644032.4	-9.7	54796.2	-7.5	126929.2
-19.6	5120	-15.6	35719.9	-12.4	334324.6	-20.1	20145.9	-16	53210.4
-38.1	784.9	-31	14672.2	-25.1	192899	-38.5	7850.3	-31.2	24510.7
-69.2	12.8	-57.3	6412.4	-47.1	120146.9	-69.1	3140.7	-57	12091.9
-119.1	107.9	-99.9	2912.9	-83.3	79063.5	-117.8	1245.3	-98.5	6254.6
-195.8	335.8	-166.1	1342.7	-140.2	54016.4	-192.3	465.6	-162.6	3326.6
-310.1	509.8	-265.4	609.7	-226.4	37704.8	-302.5	149.8	-258.3	1783.2
-475.6	596.4	-410.4	260.8	-352.9	26442.5	-461.3	32.9	-397.1	941.6
-709.7	601.3	-616.6	97	-534.1	18264.4	-684.9	1.3	-593.8	475.5
-1034.3	538.7	-903.9	25.9	-787.9	12102.6	-993.7	4.2	-866.7	219.8
-1476.5	425.2	-1296.9	2.2	-1136.6	7402.7	-1413	17.1	-1238.9	86.1
-2070.3	283.4	-1826.5	1.4	-1608.1	3921.8	-1973.9	27.5	-1738.5	24.1
-2857.2	143.9	-2530.4	8.9	-2236.9	1586.3	-2715	29.3	-2400.7	2.5
-3888.6	42.1	-3455.2	14.7	-3065.3	342.9	-3683.2	21.8	-3268.1	0.5
-5227.2	1.1	-4658	13.6	-4145	0.2	-4936.3	9.9	-4393	3.9
-6949.7	10.6	-6208.5	6.9	-5539.5	146.3	-6544.1	1.3	-5839.2	5.1
-9149	26.6	-8191.2	0.9	-7325.7	285.9	-8591.6	0.6	-7683.7	2.9
-11937.4	16.7	-10708.6	0.5	-9596.7	182.8	-11180.7	3.4	-10019.7	0.4

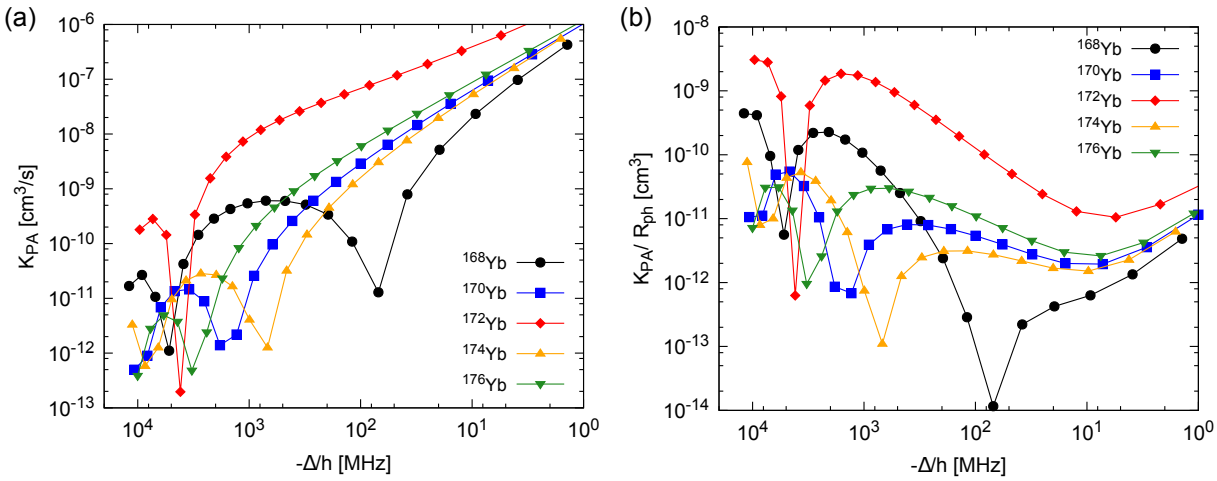

Figure 3.5.1: (a) PA rates K_{PA} and (b) $K_{\mathrm{PA}}/R_{\mathrm{ph}}$ as a function of the detuning Δ of the resonance from the atomic transition for the several bosonic isotopes of Yb with the laser intensity of 1 W/cm^2. The PA rate is calculated from the optical lengths [115, 116].

3.6 Imaging system

3.6.1 Absorption image

Absorption imaging is performed with the ${}^1S_0 \leftrightarrow {}^1P_1$ transition with a wavelength of $\lambda_{\mathrm{probe}} = 399$ nm, which consists of an ECLD with a wavelength of 798 nm, a tapered amplifier, and a waveguide SHG.

The intensity distribution of the probe light after passing through the atomic cloud with density distribution $n(\boldsymbol{r})$ is given by

$$I(x,y) = I_0(x,y)\exp\left(-\sigma_{\mathrm{res}}\int n(\boldsymbol{r})dz\right), \tag{3.6.1}$$

where I_0 is the intensity distribution without the atomic cloud and

$$\sigma_{\mathrm{res}} = \frac{3\lambda_{\mathrm{probe}}^2}{2\pi} \tag{3.6.2}$$

is the absorption cross section for a resonant light. This intensity distribution is projected on the CCD surface with a magnification ratio A:

$$\tilde{I}(x,y) = \frac{1}{A^2}I_0\left(\frac{x}{A},\frac{y}{A}\right)\exp\left[-\sigma_{\mathrm{res}}n\left(\frac{x}{A},\frac{y}{A}\right)\right] \tag{3.6.3}$$

By measuring the intensity $\tilde{I}_0 = A^{-2}I_0(x/A, y/A)$ without atoms, the effect of I_0 can be removed. Therefore the density distribution is given by

$$n\left(\frac{x}{A},\frac{y}{A}\right) = -\frac{1}{\sigma_{\mathrm{res}}}\ln\left(\frac{\tilde{I}(x,y)}{\tilde{I}_0(x,y)}\right). \tag{3.6.4}$$

In actual images, the obtained position (x, y) is discretized by CCD pixels as (x_i, y_j), where (i, j) is the index used to label a CCD pixel. To eliminate noise such as stray light,

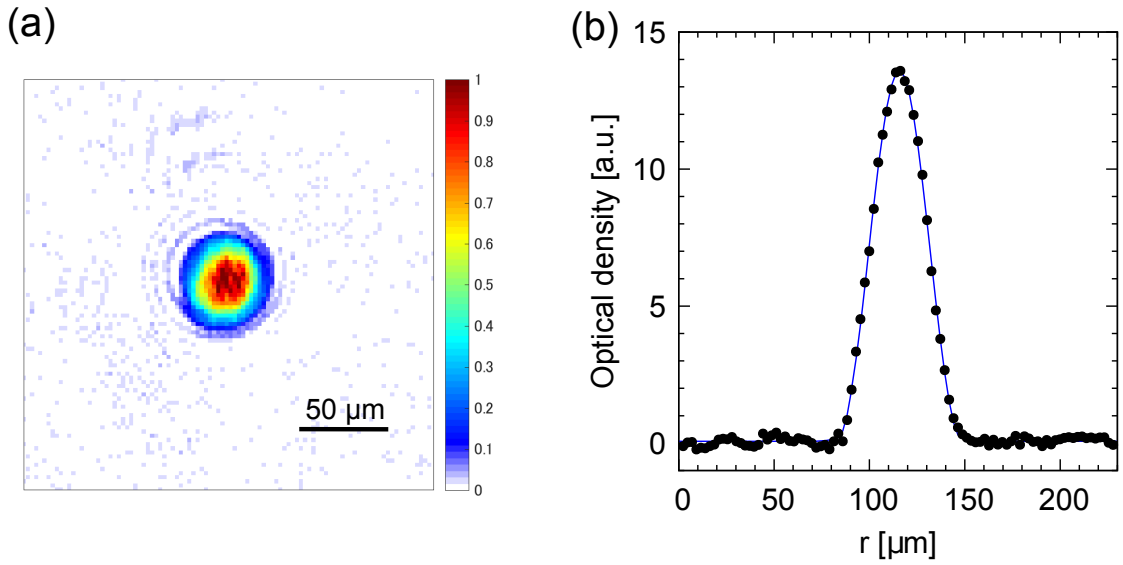

Figure 3.6.1: (a) Absorption image of the BEC of ^{174}Yb. The atom number is 1.4×10^4, and the TOF time is 14 ms. (b) Integrated optical density. The black curve is the fitting of the bimodal distribution.

dark current from a CCD pixel, and thermal noise, we take an image of the dark frame D_{x_i,y_j} in addition to the image T_{x_i,y_j} with an atomic cloud and a probe light and a flat image F_{x_i,y_j} with the probe light but the atomic cloud. For each CCD pixel, $n(x_i/A, y_j/A)$ is given by

$$n\left(\frac{x_i}{A}, \frac{y_j}{A}\right) = -\frac{1}{\sigma_{\text{res}}} \ln\left(\frac{T_{x_i,y_j} - D_{x_i,y_j}}{F_{x_i,y_j} - D_{x_i,y_j}}\right). \tag{3.6.5}$$

The total atom number N can be calculated by accumulating $n(x_i/A, y_j/A)$ over all the CCD pixels:

$$N = \frac{\Delta s}{A^2} \sum_{i=1}^{m} \sum_{j=1}^{n} n\left(\frac{x_i}{A}, \frac{y_j}{A}\right), \tag{3.6.6}$$

where (m, n) is the number of CCD pixels in the horizontal and vertical direction, respectively, and Δs is the CCD pixel size.

Bose-Einstein condensation

The density distribution of a BEC released from a harmonic trap can be derived from the Gross-Pitaevskii

$$\left[-\frac{\hbar^2}{2m}\nabla^2 + V(\boldsymbol{r}) + g|\phi(\boldsymbol{r})|^2\right]\psi(\boldsymbol{r}) = \mu\psi(\boldsymbol{r}), \tag{3.6.7}$$

where $g = 4\pi\hbar^2/m$ is the effective interaction between two particles with the scattering length a and $\psi(\boldsymbol{r})$ is an order parameter. For sufficiently large clouds, an accurate expression for the ground-state energy is obtained by neglecting the kinetic energy term in Eq. 3.6.7 (Thomas-Fermi approximation); therefore, the density $|\psi(\boldsymbol{r})|^2$ is given by

$$n(\boldsymbol{r}) = \max\left[\frac{\mu - V(\boldsymbol{r})}{g}, 0\right]. \tag{3.6.8}$$

For an anisotropic 3D harmonic trap

$$V(\boldsymbol{r}) = \frac{1}{2}m(\omega_x^2 x^2 + \omega_y^2 y^2 + \omega_z^2 z^2), \tag{3.6.9}$$

the density is written as

$$n(\boldsymbol{r}) = \frac{\mu m}{4\pi\hbar^2 a} \max\left[1 - \left(\frac{x^2}{R_x^2} + \frac{y^2}{R_y^2} + \frac{z^2}{R_z^2}\right), 0\right], \tag{3.6.10}$$

where

$$R_{\alpha,0} = \sqrt{\frac{2\mu}{m\omega_\alpha^2}} \quad (\alpha = x, y, z). \tag{3.6.11}$$

and μ becomes

$$\mu = \frac{\hbar\bar{\omega}}{2}\left(15Na\sqrt{\frac{m\bar{\omega}}{\hbar}}\right)^{2/5}, \tag{3.6.12}$$

where $N = \int d\boldsymbol{r} n(\boldsymbol{r})$ is the total number of atoms and $\bar{\omega} \equiv (\omega_x\omega_y\omega_z)^{1/3}$.

The density distribution of a BEC after ballistic expansion for a duration t can be represented as

$$n(\boldsymbol{r}, t) = \frac{15N_{\mathrm{BEC}}}{8\pi R_x(t)R_y(t)R_z(t)} \max\left[1 - \left(\frac{x^2}{R_x^2(t)} + \frac{y^2}{R_y^2(t)} + \frac{z^2}{R_z^2(t)}\right), 0\right] \tag{3.6.13}$$

Here,

$$R_\alpha(t) = R_{\alpha,0}\sqrt{1 + \omega_\alpha^2 t^2} \quad (\alpha = x, y, z). \tag{3.6.14}$$

Integrating Eq. 3.6.13 one- and two-dimensionally gives the following 2D and 1D density distributions

$$n_{\mathrm{TF}}(x, y, t) = \frac{5N_{\mathrm{BEC}}}{2\pi R_x(t)R_y(t)}\left[\max\left[1 - \left(\frac{x^2}{R_x^2(t)} + \frac{y^2}{R_y^2(t)}\right), 0\right]\right]^{3/2}, \tag{3.6.15}$$

$$n_{\mathrm{TF}}(x, t) = \frac{15N_{\mathrm{BEC}}}{16R_x(t)}\left[\max\left[1 - \frac{x^2}{R_x^2(t)}, 0\right]\right]^2. \tag{3.6.16}$$

For fitting of the density distribution of the atomic cloud, we often use the bimodal function, which is a sum of the Thomas-Fermi distribution and the thermal Gaussian distribution. Figure 3.6.1 (a) is a typical absorption image of a BEC of ^{174}Yb, and Fig. 3.6.1 (b) is the result of the bimodal fitting to the 1D optical density.

3.6.2 Fluorescence imaging

For detection of a small number of atoms, we perform fluorescence imaging. We construct a MOT system with the $^1S_0 \leftrightarrow {}^1P_1$ transition. The fluorescence from the atoms in the MOT is detected by an EMCCD camera (iXon, Andor). We integrate the fluorescence counts during the MOT, which is proportional to the number of atoms (Figure 3.6.2). To suppress counts from stray light, we use an interference filter.

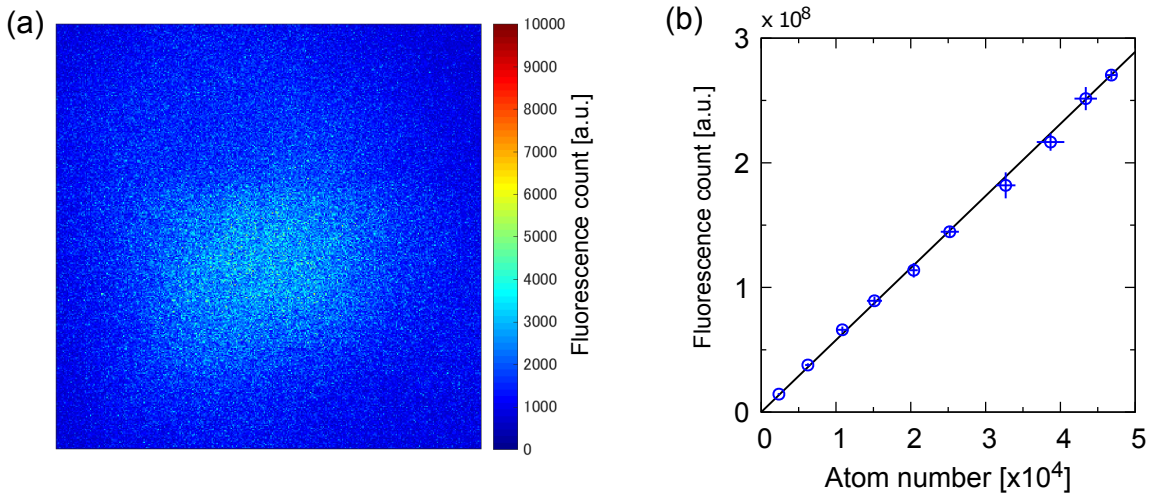

Figure 3.6.2: (a) Typical fluorescence image of the atomic cloud. (b) Atom number - Fluorescence count correspondence. We obtain the atom number with the absorption image and the corresponding fluorescence count by varying the atom loading time from 1.5 to 8 s. The linear fitting (black line) shows the linear correspondence between the atom number and the fluorescence count. We note that this correspondence depends on the intensity of the MOT light, quantum efficiency, and exposure time of the EMCCD camera.

Chapter 4

Observation of the Mott insulator to superfluid crossover of a driven-dissipative Bose-Hubbard system

In this chapter, we report a systematic investigation of a Bose-Hubbard system with artificial on-site two-body loss via the photo-association process dissipation. Especially, we reveal the effect of the dissipation on the Mott insulator - superfluid quantum phase transition. First, we describe the engineering of the dissipation in Section 4.1. After explaining the theoretical model in Section 4.2, we report the stability of atoms with the dissipation in Section 4.3. In Section 4.4, we describe the effect of the dissipation on the quantum phase transition both on theoretical and experimental sides. The theoretical calculations were carried out by Dr. Ippei Danshita.

4.1 Engineering two-body dissipation

To implement two-body inelastic atom loss with controllable strength, we introduce a single-photon photo-association (PA) process for ultracold Yb atoms in a 3D optical lattice. The PA beam drives the intercombination transition of ${}^1S_0 \leftrightarrow {}^3P_1$, by which two atoms in doubly-occupied sites are photoassociated into the ${}^1S_0 + {}^3P_1$ molecular state and immediately dissociated into the two ground-state atoms (see Fig. 4.1.1). This process gives high kinetic energy to the dissociated atoms, which thus results in the escape from the lattice. In this way, the PA laser induces the two-body inelastic collision loss between the two atoms occupying the same site.

4.1.1 Measurement of the inelastic collision rate

We measure the inelastic collision coefficient by applying the PA laser to the atoms in the 3D optical lattice. Based on the calculation, we chose the molecular state of $v' = 16$ with $\Delta/h = -3683.2$ MHz (see Section 3.5.2). The resonance frequency of the PA transition is shifted with varying the intensity of the PA laser due to the light shift. Thus, we adjust the laser frequency to the resonance for each intensity.

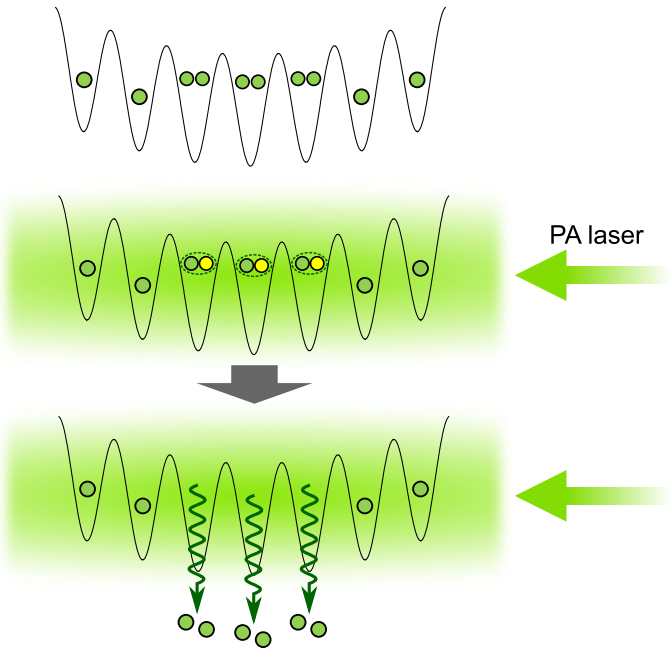

Figure 4.1.1: Schematic of the introduced inelastic two-body collision. When there are singly- and doubly-occupied sites in the lattice (top), the atoms in the doubly-occupied sites are converted into molecules by applying the PA laser (middle), and then escape from the lattice due to the high kinetic energy given by the dissociation (bottom).

The lattice depth is $V_0 = 14\ E_R$, which is deep enough to suppress the tunneling in the timescale of this measurement. We adjust the total atom number so that there are singly- and doubly- occupied sites. The atoms in the doubly-occupied sites are converted into the molecules by applying the PA laser and then escape from the lattice due to the high kinetic energy given by the dissociation. When the molecular loss rate Γ_{M} is much larger than the strength of atom-molecular coupling g ($\hbar\Gamma_{\mathrm{M}} \gg g$), the number of the atoms in the doubly-occupied sites exponentially decays (see Appendix B). By measurement, we confirm that this condition is satisfied (Fig. 4.2.1). The decay rate corresponds to the inelastic collision rate induced by the PA process Γ_{PA}. Thus, the remaining atom number $N(t)$ decreases as

$$N(t) = N_1 + N_2 \exp\left(-\Gamma_{\mathrm{PA}} t\right). \tag{4.1.1}$$

We measure the atom number with the fluorescence detection and observe the exponential decay of the atom number (Fig. 4.1.2 (a)) and extract the inelastic collision rate Γ_{PA} with varying the intensity of the PA rate (Fig. 4.1.2 (b)). The inelastic collision coefficient β_{PA} is determined through the relation

$$\Gamma_{\mathrm{PA}} = \beta_{\mathrm{PA}} \int |w(\boldsymbol{r})|^4 d\boldsymbol{r}, \tag{4.1.2}$$

where $w(\boldsymbol{r})$ is the Wannier function of the lowest band. The dashed line in Fig 4.1.2 indicates the linear fit to the low intensity data with a slope of $2.10(7)\times10^{-11}$ cm^{3}s^{-1}/(Wcm^{-2}), which well agrees with the theoretical calculation of the PA rate of $K_{\mathrm{PA}} = 2.12 \times 10^{-11}$ cm^{3}s^{-1}/(Wcm^{-2}) [116]; this means that the kinetic energy given by the single PA process is large enough for the escape of the atoms from the lattice potential.

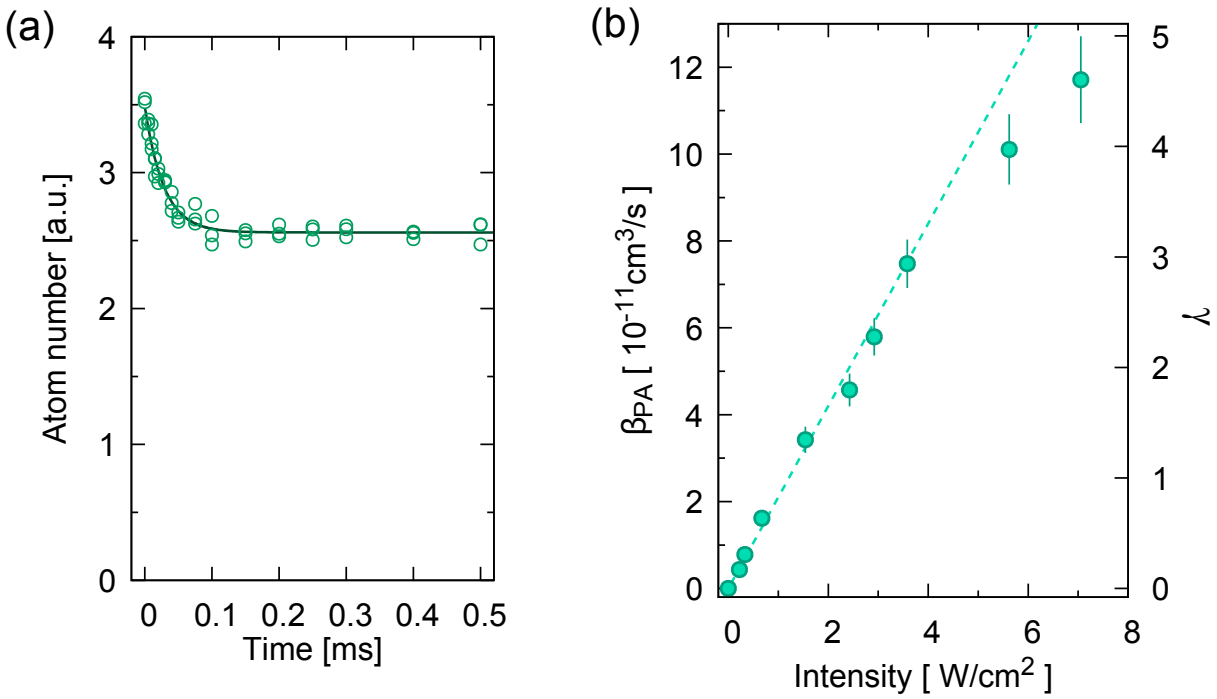

Figure 4.1.2: (a) Time evolution of remaining atom number in a 3D optical lattice for the measurement of the inelastic collision rate $\Gamma_{\rm PA}$. The lattice depth is set to $V_0 = 14\ E_R$. The offset corresponds to the remaining atoms in the singly-occupied sites N_1. This data is taken with the intensity of the PA laser of 2.92 W/cm^2. (b) The inelastic collision coefficient $\beta_{\rm PA}$ as a function of the intensity of the PA laser. The dashed line in Fig 4.1.2 indicates the linear fit to the low intensity data with a slope of $2.10(7) \times 10^{-11}$ cm^{3}s^{-1}/(Wcm^{-2}), which well agrees with the theoretical calculation of the PA rate of $K_{\rm PA} = 2.12 \times 10^{-11}$ cm^{3}s^{-1}/(Wcm^{-2}) [116]. Note that a saturating behavior is observed at the highest intensity, the behavior of which is reported in other experiments performed in a harmonic trap [137, 138, 139, 140]. The scale on the right in (b) indicates the dimensionless dissipation strength γ.

In this way, we can realize controllable strength of inelastic collision up to $\beta_{\rm PA} \sim 1.2 \times 10^{-10}$ cm^3/s corresponding to $\Gamma_{\rm PA} \sim$70 kHz in the lattice depth of $V_0 = 14\ E_R$. In order to characterize the strength of the dissipation, we introduce the dimensionless dissipation strength

$$\gamma = \hbar\Gamma_{\rm PA}/U, \tag{4.1.3}$$

which does not depend on the lattice depth. We can control the dissipation strength up to $\gamma \sim 5$.

4.2 Theoretical model

In this section, we describe the theoretical model of this system. The system of bosonic atoms in a sufficiently deep optical lattice coupled coherently to the $^1S_0 + {}^3P_1$ molecular state via the PA laser is well described by the Markovian master equation for the coupled

atom-molecule mixture model [141] with a one-body molecular loss term. By adiabatically eliminating the molecular degrees of freedom on the basis of a second-order perturbation theory for the master equation [142, 143], we derive the effective master equation (see Appendix A for details),

$$\hbar\frac{d}{dt}\hat{\rho}_{\rm eff} = -i\left[\hat{H}_{\rm eff}, \hat{\rho}_{\rm eff}\right] + L_2(\hat{\rho}_{\rm eff}), \tag{4.2.1}$$

where

$$\hat{H}_{\rm eff} = \sum_j \frac{U}{2}\hat{n}_{{\rm A},j}(\hat{n}_{{\rm A},j}-1) - \sum_{\langle j,k\rangle} J\left(\hat{a}_j^\dagger \hat{a}_k + {\rm h.c.}\right), \tag{4.2.2}$$

$$L_2(\hat{\rho}_{\rm eff}) = \frac{\hbar\Gamma_{\rm PA}}{4}\sum_j \left(-\hat{a}_j^\dagger\hat{a}_j^\dagger\hat{a}_j\hat{a}_j\hat{\rho}_{\rm eff} - \hat{\rho}_{\rm eff}\hat{a}_j^\dagger\hat{a}_j^\dagger\hat{a}_j\hat{a}_j + 2\hat{a}_j\hat{a}_j\hat{\rho}_{\rm eff}\hat{a}_j^\dagger\hat{a}_j^\dagger\right), \tag{4.2.3}$$

and

$$\Gamma_{\rm PA} = \frac{8g^2}{\hbar^2\Gamma_{\rm M}}. \tag{4.2.4}$$

$\hat{a}_j$ denotes the annihilation operator of atoms at site j and $\hat{n}_{{\rm A},j} = \hat{a}_j^\dagger\hat{a}_j$. $\langle j,k\rangle$ represents nearest-neighboring pairs of lattice sites. This model is nothing but the single-component Bose-Hubbard model with a two-body loss term [143], where J, and $\Gamma_{\rm PA}$ denote the tunneling amplitude, and the strength of the two-body inelastic collision induced by the PA. In Eq. (4.2.4), g and $\Gamma_{\rm M}$ denote the strengths of the atom-molecule coupling and the one-body molecular loss, respectively. While g is controllable by varying the intensity of the PA laser, $\Gamma_{\rm M}$ is fixed for a specific molecular state.

The effective master equation (4.2.1) is valid only when $\hbar\Gamma_{\rm M} \gg \max(|g|, |D|, |W|, |U|, J)$, where D and W denote the detuning of the PA coupling and the on-site interaction between an atom and a molecule, respectively. $\Gamma_{\rm M}$ can be determined by measuring the PA rate as a function of $(D-U)$, which is theoretically described as

$$\tilde{\Gamma}_{\rm PA} = \frac{8g^2}{\hbar^2\Gamma_{\rm M}}\left[1 + 4\left(\frac{D-U}{\hbar\Gamma_{\rm M}}\right)^2\right]^{-1}. \tag{4.2.5}$$

In Fig. 4.2.1, we show measured $\tilde{\Gamma}_{\rm PA}$ as a function of $(D-U)$. Fitting the data to Eq. (B.0.10), we determine $\Gamma_{\rm M} = 2\pi\times185(13)$ kHz $= 1.16(8)$ MHz. On the other hand, g can be estimated from the experimentally determined $\Gamma_{\rm M}$ and $\Gamma_{\rm PA}$, resulting in $g/\hbar \sim 100$ kHz at most. Therefore, we can confirm that the condition $\hbar\Gamma_{\rm M} \gg g$ is satisfied, as well as the condition $\hbar\Gamma_{\rm M} \gg \max(|D|, |U|, |W|)$ because $D/\hbar$, $U/\hbar$ and $W/\hbar$ are at most a few 10 kHz in our experiment.

4.3 Stability of the atoms with a unit-filling initial state

First, we investigate the stability of the atoms with a unit-filling initial state at a fixed lattice depth. Here, the strength of the dissipation is varied in a wide range from the

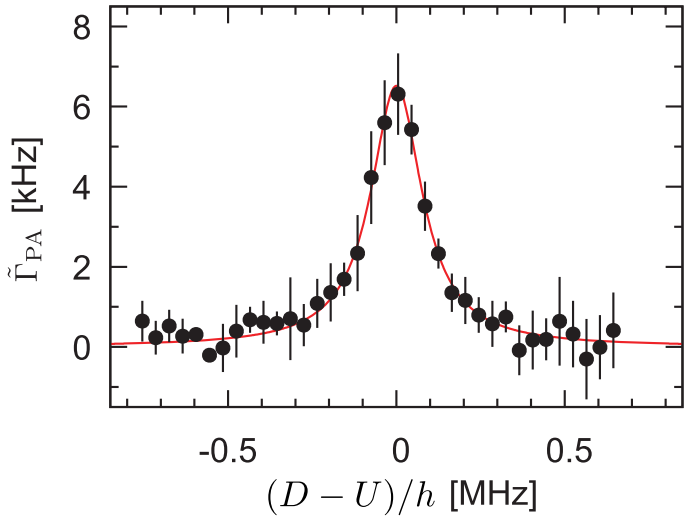

Figure 4.2.1: Measurement of the one-body molecular loss $\tilde{\Gamma}_{\mathrm{PA}}$. The black points represent the loss rate while the red curve is the fit of Eq. (B.0.10).

weak region, in which the dissipation acts as perturbation, to the strong region, in which it exceeds any other energy scale. In contrast to the previous works, in which the experiments were done only in the limited range of the dissipation strength [74, 76], the wide range of our engineered dissipation enables us to observe a crossover between qualitatively different roles of the dissipation.

4.3.1 Measurement of the two-body loss rate

In contrast to the measurement of β_{PA} shown in Fig. 4.1.2, this measurement is done at a shallow lattice depth of $V_0 = 8\ E_R$, in which the tunneling rate $6J/\hbar$ is 4.7 kHz. Thus, in the absence of dissipation, atoms can tunnel to neighboring sites in a timescale of this measurement, so that we can investigate how the atom tunneling, which is the only mechanism causing doubly-occupied sites, is modified by the dissipation. In our experiment, we first adiabatically load a BEC of 1.0×10^4 atoms into a 3D optical lattice with $V_0 = 15\ E_R$, in which the state is a singly-occupied Mott insulator. Subsequently, we ramp down the lattice to $V_0 = 8\ E_R$ in 0.2 ms, and apply the PA laser at the same time. The initial atom number at each site is at most unity, confirmed by the absence of the atom loss using the PA laser and also the occupancy-sensitive high-resolution laser spectroscopy [43].

The measured two-body loss rate κ is shown in Fig. 4.3.1. The values of κ are determined by fitting of the two-body loss function

$$N(t) = \frac{N(0)}{1 + \kappa t} \tag{4.3.1}$$

to the data [74].

For weak dissipation, the two-body loss rate κ grows as Γ_{PA} increases, which reflects the increase of the detection rate of tunneling. For strong dissipation, however, the two-body loss rate decreases when Γ_{PA} increases. Namely, atom loss is suppressed by the strong

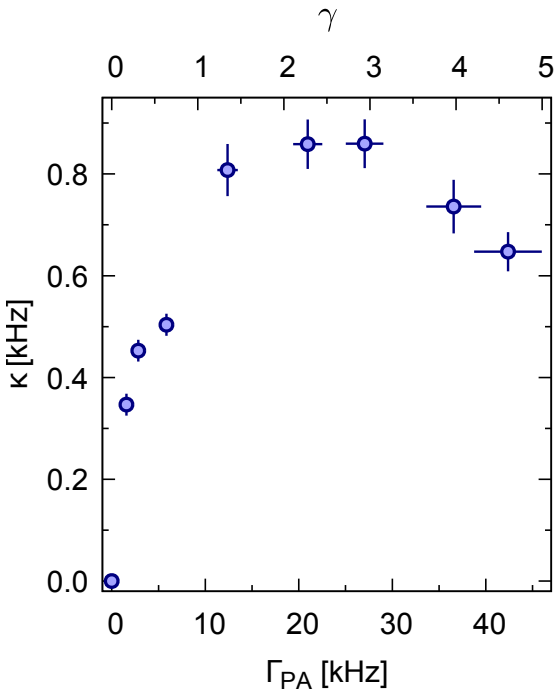

Figure 4.3.1: Inelastic collision rate Γ_{PA} dependence of the two-body loss rate κ for atoms initially prepared in a Mott insulating state with singly occupied sites. The scale in the top of the figure indicates the dimensionless dissipation strength γ.

on-site dissipation. This counter-intuitive behavior is a manifestation of the continuous quantum Zeno effect [75], that is, the strong two-body inelastic collision plays a role of the strong measurement and suppresses the coherent process of tunneling.

4.3.2 Numerical simulation of the loss dynamics

We numerically simulate the loss dynamics with the unit-filling initial state with the Gutzwiller variational approach [144, 145, 36], the detail of which is described in Appendix C. After preparing the superfluid state at $V_0 = 5E_R$, we ramp up the lattice to create the Mott insulating state at $V_0 = 15E_R$. Right after the preparation of the Mott insulating state, we ramp down the lattice depth to $V_0 = 8E_R$ in 0.2 ms. The time evolution of the atom number after this sudden ramp down is fitted to Eq. 4.3.1.

We see from Fig. 4.3.2 that when γ increases, κ initially increases but starts to decrease around $\gamma = 1$. A similar behavior is also seen in the experiment as shown in Fig. 4.3.1.

From the comparison between the theory and experiment in a wide range of dissipation strength, we confirm that the measured loss behavior correctly captures the theoretical prediction.

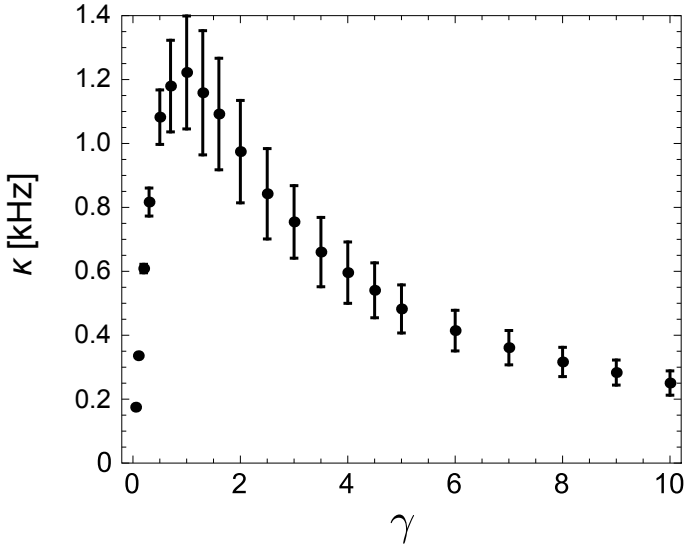

Figure 4.3.2: Numerical calculation of κ as a function of the dissipation strength γ. κ is extracted by the fitting to the time evolution of the atom density starting from the Mott insulating state with unit filling.

4.3.3 Unexpectedly large atom loss for strong intensity of PA laser

We note that we observe unexpectedly large atom loss for much higher intensity of PA laser, which prevents the suppression of the two-body loss rate for the strong dissipation region over $\gamma \sim 5$ from clear observation. Therefore, in our experiment, we restrict the region of the dissipation strength under $\gamma \sim 5$.

Here, we discuss the possible origin of the unexpectedly large atom loss rate κ observed for much higher intensity of PA laser corresponding to $\gamma > 5$. This additional atom loss which is not taken into account in the present theory prevents the suppression of two-body loss rate from clear observation, and is also observed in the ramp-down dynamics in the deep lattice region. For $V_0 = 20\ E_R$, the measured loss rate is about 30 Hz, while the loss rate expected from the theory is about 3 Hz. We confirm that this loss is not attributed to the photon scattering: the photon scattering rate we measure is about 3 Hz for intensity $I \sim 30$ W/cm^2.

The observed additional loss can be explained by the Raman-assisted tunneling [146] due to the PA laser. Because of the difference of the polarizability between the $^1S_0$ state and the $^3P_1$ state, there is a finite overlap of the Wannier functions of the two atoms placed at the neighboring sites in which one atom is $^1S_0$ state and the another atom is $^3P_1$ state. Therefore, the neighboring sites can be coupled though the $^3P_1$ state as the intermediate state.

The overlap between the $^1S_0$ atom and $^3P_1$ state atom placed at the neighboring sites

f_{N} is described as

$$f_{\mathrm{N}} = \left| \int w_g^*(\boldsymbol{r}) w_e(\boldsymbol{r}-\boldsymbol{d}) d\boldsymbol{r} \right| \tag{4.3.2}$$

$$= \left| \int w_{g,x}^*(x) w_{e,x}(x-d) dx \int w_{g,y}^*(y) w_{e,y}(y) dy \int w_{g,z}^*(z) w_{e,z}(z) dz \right|, \tag{4.3.3}$$

where g and e indicate the internal state $^1S_0$ and $^3P_1$, respectively, and d is the lattice constant. The overlap between the $^1S_0$ atom and $^3P_1$ state atom placed at the same site f_0 is described as

$$f_0 = \left| \int w_g^*(\boldsymbol{r}) w_e(\boldsymbol{r}) d\boldsymbol{r} \right| \tag{4.3.4}$$

$$= \left| \int w_{g,x}^*(x) w_{e,x}(x) dx \int w_{g,y}^*(y) w_{e,y}(y) dy \int w_{g,z}^*(z) w_{e,z}(z) dz \right|. \tag{4.3.5}$$

As shown in Fig. 4.3.3, when the PA laser is applied, two transitions $\Omega_1 = \Omega_0 f_0$, $\Omega_2 = \Omega_0 f_{\mathrm{N}}$ and the detuning from the atom transition $\Delta = 2\pi \times 3.6832$ GHz lead to Raman coupling between two neighboring sites, which has the Rabi frequency

$$\Omega_R = \frac{\Omega_1 \Omega_2}{2\Delta} = \frac{(\Omega_0 f_0)(\Omega_0 f_{\mathrm{N}})}{2\Delta} = \frac{\Omega_0^2}{2\Delta} f_0 f_{\mathrm{N}}. \tag{4.3.6}$$

From the calculation, for $\gamma \sim 5$ in the lattice depth of $V_0 = 20\ E_R$, the effective tunneling amplitude $J_{\mathrm{eff}} = J + \Omega_R$ is 3.8 times larger than J. This enhancement amounts to the two-body loss rate $\kappa \sim 50$ Hz, which is consistent with the observation. To avoid the effect of this additional loss, we restrict the region of the dissipation strength under $\gamma \sim 5$ in this work.

4.4 Effect of the dissipation on the quantum phase transition

We next investigate the effect of the on-site dissipation on the quantum phase transition from the Mott insulator to the superfluid [37], which is the main topic of the present work. Specifically, starting with a singly-occupied Mott insulating state, we analyze the dynamics of the atoms subjected to the PA laser during a ramp-down of the lattice depth. The ramp-down speed is $-2\,E_{\mathrm{R}}/\mathrm{ms}$, which is much slower than the case of the two-body loss measurement discussed above.

Before presenting the experimental observation, we show the theoretically analyze of the dynamics by assuming a homogeneous system and solving the effective master equation (4.2.1) within the Gutzwiller mean-field approximation [69, 70] in order to obtain some insights on the problem.

4.4.1 Theoretical analysis

An important effect of the dissipation on the quantum phase transition is that it explicitly breaks the conservation of the particle number of the system. Since the superfluid-Mott

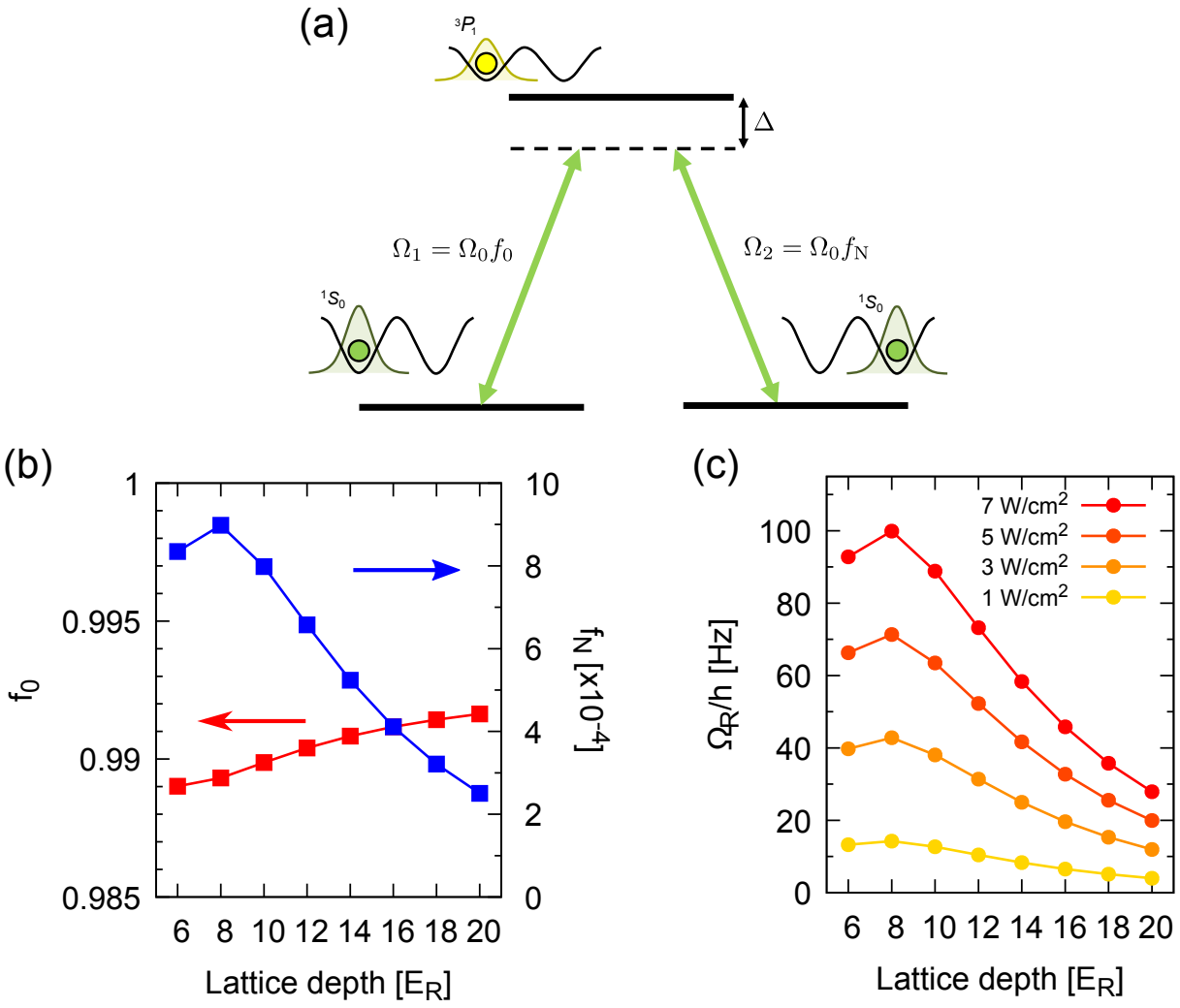

Figure 4.3.3: Raman assisted tunneling. (a) Schematic of the Raman process. $\Delta = 2\pi \times 3.6832$ GHz is the detuning from the atomic $^1S_0 \leftrightarrow {}^3P_1$ transition. (b) Overlap of the Wannier functions f_0 and f_N. The red and blue squares indicate f_0 and f_N, respectively. (c) Rabi frequency of the Raman coupling as a function of the lattice depth and the intensity of the PA laser.

insulator transition without the dissipation ($\gamma = 0$) is originated from the U(1) symmetry associated with the particle-number conservation, the introduction of finite γ changes the transition to a crossover. Notice, however, that the two-body loss term does not explicitly break the U(1) symmetry. Indeed, the master equation (4.2.1) is invariant under the U(1) transformation, $\hat{a}_j \to \hat{a}_j e^{i\varphi}$, where φ is an arbitrary constant.

Another important effect is that the two-body loss term makes the "superfluid" state at unit filling so dissipative that it cannot carry dissipationless superflow. In this sense, even a small loss term immediately breaks the superfluidity. However, one can distinguish such a lossy gas with delocalized atoms and long-range coherence from the Mott insulating state and study the crossover from the latter state to the former in the dynamics subjected to a slow ramp-down of the lattice depth. Hereafter, for convenience we use the term "superfluid" to describe the former state.

In order to theoretically characterize this crossover, we present some important properties of the crossover phenomenon that are independent of either the preparation procedure the initial Mott insulating state or the ramp-down speed with in the Gutzwiller approximation.

Crossover from the Mott insulator to the superfluid

Specifically, we focus on the growth rate of the superfluid order parameter amplitude during a slow increase of the tunneling amplitude. The time sequence of the tunneling amplitude is given by

$$J(t) = \frac{J_{\rm fin} - J_{\rm ini}}{\tau} t + J_{\rm ini}, \tag{4.4.1}$$

while the other parameters are fixed to be time-independent, where τ denotes the total evolution time.

We set the initial and final values of the tunneling amplitude as $zJ_{\rm ini}/U = 0$ and $zJ_{\rm fin}/U = 0.5$. At $zJ/U = zJ_{\rm ini}/U$ at unit filling, the ground state is the Mott insulating state, i.e., $\rho^{\rm gs}_{l,m} = \delta_{l,2}\delta_{m,2}$ in the local density matrix description (see Appendix C). As an initial state of the dynamics, we add small random noise terms to the ground state $\rho^{\rm gs}_{l,m}$ as

$$\rho_{l,m}(t=0) = \rho^{\rm gs}_{l,m} + \epsilon^{\rm re}_{l,m} + i\epsilon^{\rm im}_{l,m}, \tag{4.4.2}$$

where $\epsilon^{\rm re}_{l,m}$ and $\epsilon^{\rm im}_{l,m}$ are assumed to be independent random variables with zero average and a box distribution from $-\varepsilon$ to ε. In the absence of the noise terms ($\varepsilon = 0$), the system remains in the initial state and the evolution towards the "superfluid" state can not be captured because $\rho^{\rm gs}_{l,m}$ is a time-independent solution of the effective master equation Eq. 4.2.1 within the Gutzwiller approximation.

In Fig. 4.4.1 (a), we show the time evolution of the amplitude of the superfluid order parameter $|\psi|^2$ for several values of the noise strength ε. We see that $|\psi|^2$ significantly depends on ε. In contrast, as shown in Fig. 4.4.1 (b), we find that there is a time region where the rate of the exponential growth in $|\psi|^2$

$$G \equiv \frac{d}{dt} \ln |\psi|^2 \tag{4.4.3}$$

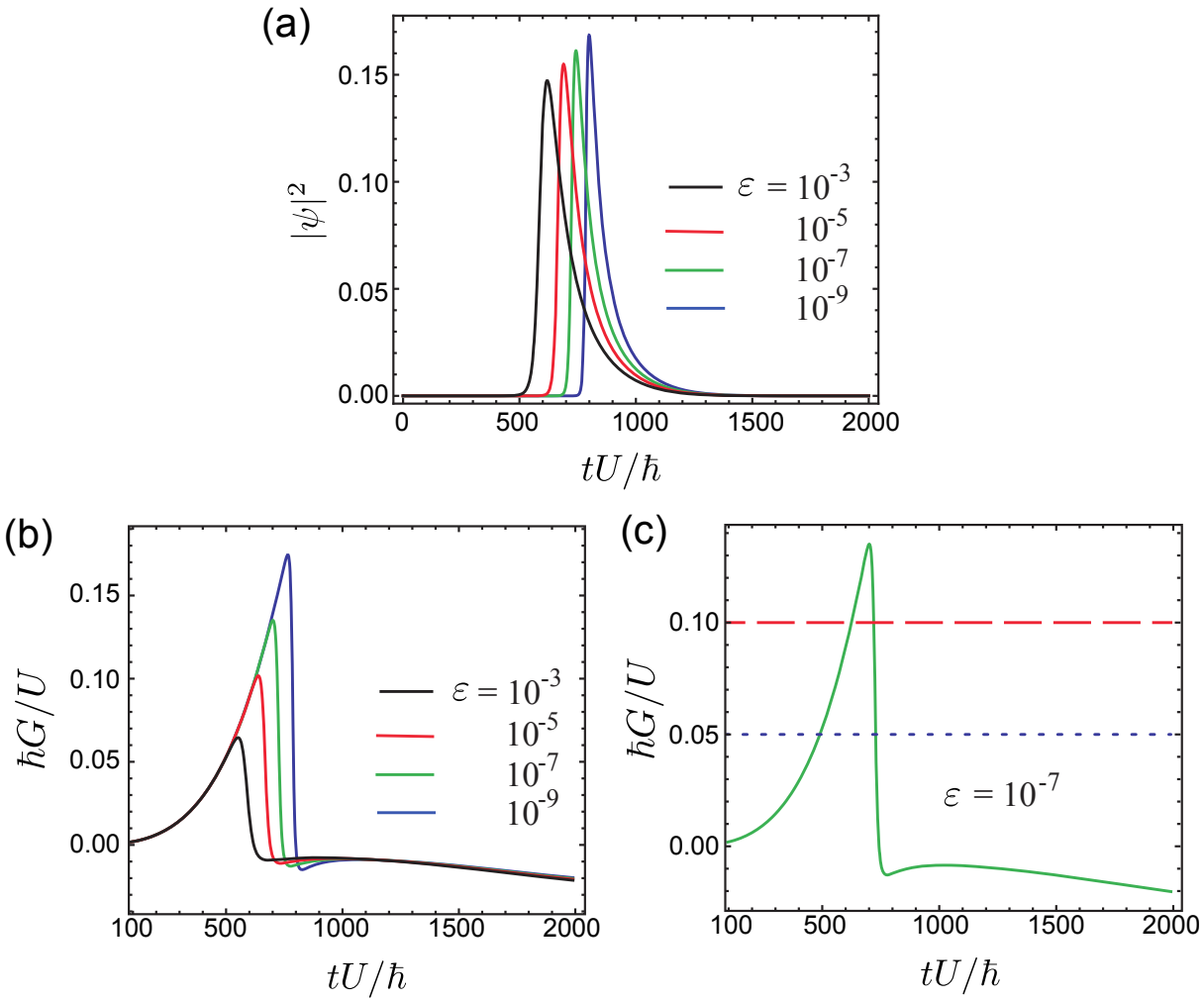

Figure 4.4.1: Time evolution of the amplitude of the superfluid order parameter and its growth rate. (a) Time evolution of $|\psi|^2$. (b), (c) Growth rate $G = \frac{d}{dt} \ln |\psi|^2$ during the linear ramp-up of the tunneling J, where $\tau U/\hbar = 2000$, $zJ_{\mathrm{ini}}/U = 0.0$, $zJ_{\mathrm{fin}}/U = 0.5$, and $\gamma = 1$. The red dashed line and the blue dotted line in (c) represent $\hbar G/U = 0.1$ and 0.05, respectively.

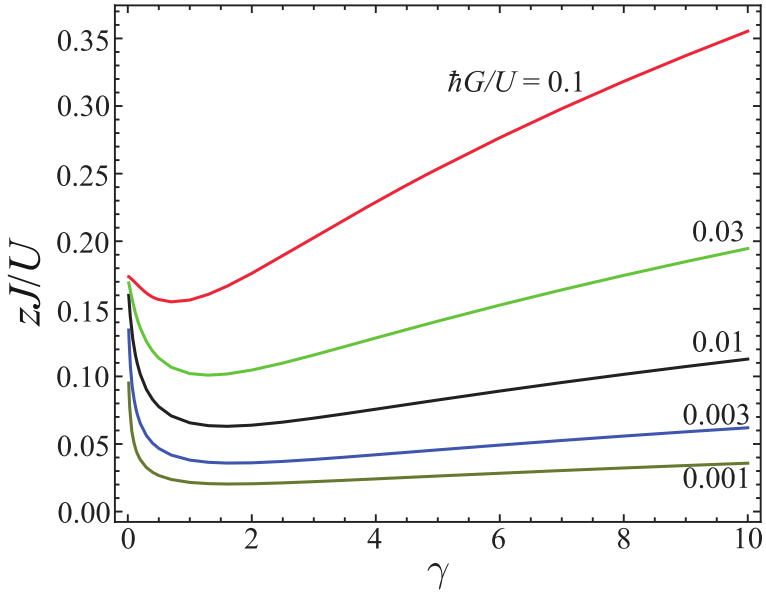

Figure 4.4.2: Contour plot of $G = \frac{d}{dt} \ln |\psi|^2$ in the $(\gamma, zJ/U)$-plane. While we take $zJ_{\rm ini}/U = 0.0$, $zJ_{\rm fin}/U = 0.5$, and $\tau U/\hbar = 10000$, the contour plot is independent of these parameters as long as τ is sufficiently large.

increases and is independent of ε. Notice that G in such a time region is also independent of τ as long as τ is sufficiently large. We use the values of G in the time region to characterize the time scales of the crossover from the Mott insulator to the "superfluid" that are independent of either ε or τ. As indicated in Fig. 4.4.1 (c), for given γ we determine the value of zJ/U at which G in the universal time region takes a certain value, e.g., $\hbar G/U = 0.1$ (red dashed line) or 0.05 (blue dotted line).

In Fig. 4.4.2, we show a contour plot of $\hbar G/U$ in the $(\gamma, zJ/U)$-plane. There we see that when γ increases from zero, the contour lines become more distant from one another, i.e., the transition is changed to a crossover. We also see that zJ/U on each contour line exhibits a non-monotonic behavior as a function of γ; when γ increases, it initially decreases but starts to increase above a certain γ. This result indicates that the strong two-body loss term, i.e., $\gamma \gg 1$, favors the Mott insulating state over the "superfluid".

Numerical simulation of the dynamics with the experimental parameters

In the calculation discussed above, the tunneling amplitude is linearly increased. Here we simulate the realistic experimental situation: we ramp down the lattice depth linearly in time

$$V_0(t) = \begin{cases} v_{\rm up}(t - t_0) + V_{0,\rm ini}, & \text{when } t_0 \le t < t_1, \\ v_{\rm down}(t - t_1) + V_{0,\rm max}, & \text{when } t_1 \le t < t_2. \end{cases} \tag{4.4.4}$$

We start with the superfluid ground state at $V_{0,\rm ini} = 5\,E_{\rm R}$ and $t_0 = -100\,$ms while setting $\gamma = 0$. We slowly ramp up the optical lattice in 100 ms to $V_{0,\rm max} = 20\,E_{\rm R}$, implying that $t_1 = 0\,$ms and $v_{\rm up} = 0.15\,E_{\rm R}/$ms, in order to prepare a Mott insulating state. Right after preparing the Mott insulating state, we turn on γ to be a finite value

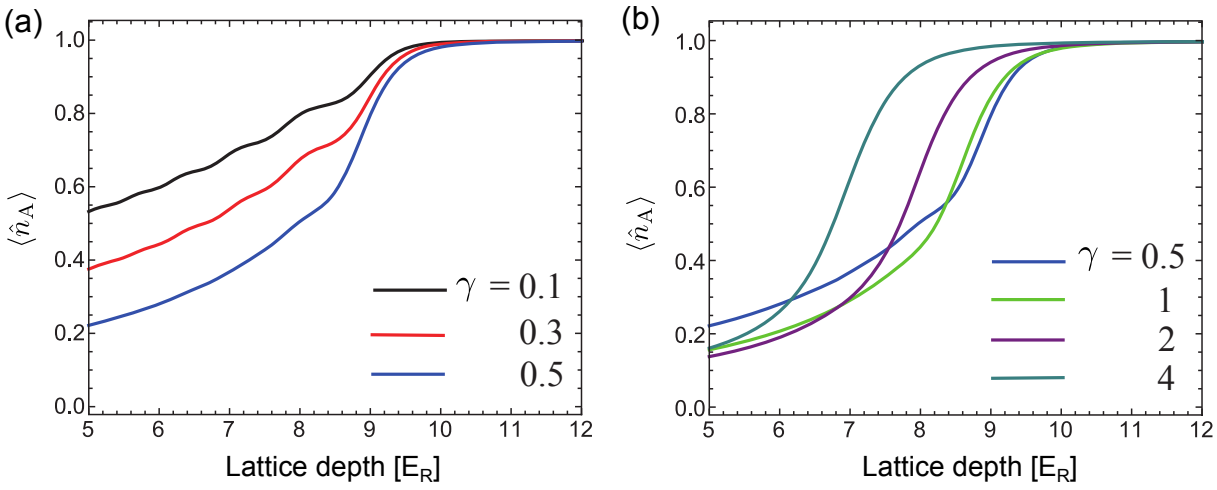

Figure 4.4.3: Atom density $\langle \hat{n}_A \rangle$ as a function of the instantaneous value of the lattice depth V_0/E_R. We take the time region $t_1 \leq t < t_2$.

and ramp down the optical lattice to $V_{0,\mathrm{fin}} = 5\,E_R$ in 7.5 ms, implying that $t_2 = 7.5$ ms and $v_{\mathrm{down}} = -2\,E_R/\mathrm{ms}$. Notice that in contrast to the dynamics subjected to the tunneling amplitude ramp-up analyzed above, we do not explicitly include small random noise terms in the initial condition. Instead, the finite-time ramp-up process creates small excitations in the prepared Mott insulating state at $t = t_1$, which practically take a role of small initial noise terms needed for dynamically melting the initial Mott state into the "superfluid" state.

In Fig. 4.4.3, we show the atom number per site $\langle \hat{n}_A \rangle$ during the ramp-down of the lattice depth, where $t_1 \leq t < t_2$, as a function of the instantaneous value of V_0/E_R. In Fig. 4.4.3 (a), we see that the onset of the atom loss shifts to the side of large V_0/E_R when γ increases up to $\gamma = 0.5$. In contrast, as shown in Fig. 4.4.3 (b), the onset significantly shifts to the side of small V_0/E_R when γ increases further from $\gamma = 0.5$. This means that the melting of the initial Mott insulating state is delayed due to the effect of the strong two-body loss term.

As shown in Fig. 4.4.4, a similar tendency is also seen in the dynamics of the condensate fraction $|\psi|^2/\langle \hat{n}_A \rangle$, which qualitatively corresponds to the strength of the coherence peak in the momentum distribution. When γ increases from $\gamma = 0.5$, the onset of the growth of $|\psi|^2/\langle \hat{n}_A \rangle$ shifts significantly to the side of small V_0/E_R. Note that the oscillation of the condensate fraction originates from non-adiabaticity of the ramp down of the lattice depth. Because the gap of the amplitude mode is small in the crossover region [147], a relatively fast ramp-down across the crossover excites the amplitude mode. In contrast, such an oscillation is not observed in the experiment likely because of the combined effect of quantum and thermal fluctuations, and the spatial inhomogeneity due to the trap potential. Specifically for the inhomogeneity, the frequency of the amplitude mode significantly depends on the chemical potential, which varies in space in the presence of a trap potential, and this leads to the dephasing of the oscillation.

Finally, we summarize the numerical calculation of the atom number per site and the condensation fraction in Fig. 4.4.5. Each curve of Fig. 4.4.3 and Fig. 4.4.4 represent a cross-section view of Fig. 4.4.5.

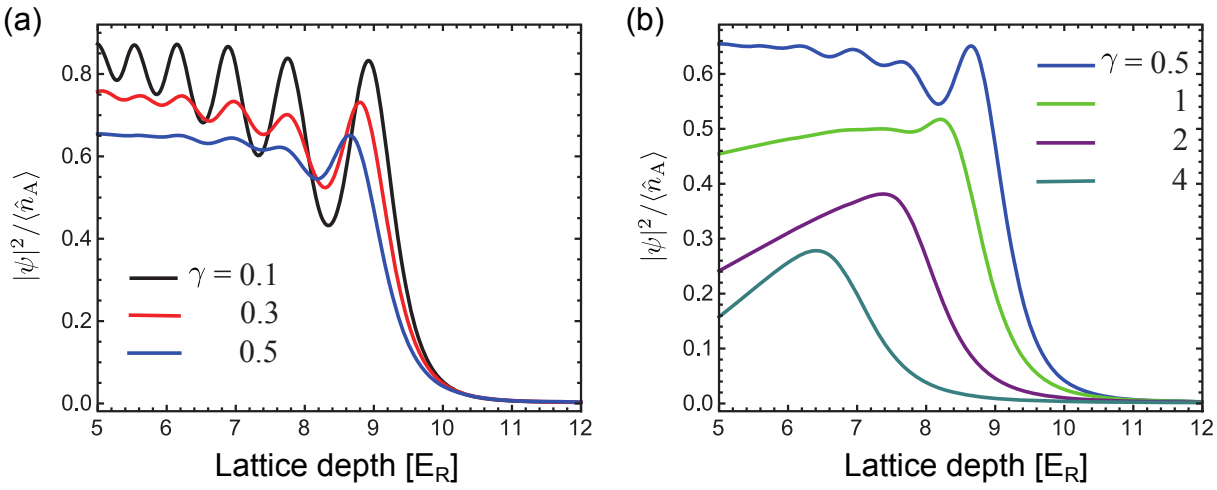

Figure 4.4.4: Condensate fraction $|\psi|^2/\langle\hat{n}_A\rangle$ as a function of the instantaneous value of the lattice depth V_0/E_R. We take the time region $t_1 \leq t < t_2$.

In the summary of the numerical simulation, we characterize the crossover by the growth rate of the superfluid order-parameter amplitude; when the growth rate is smaller, the system is deeper in the Mott insulator region. According to this characterization, we find that in the strong on-site dissipation region, where $\gamma \gg 1$, the Mott insulating state is more favored for larger γ (Fig. 4.4.2). This effect originates from the quantum Zeno suppression of the tunneling, which is observed in the two-body loss rate measurement (Section 4.3).

This interesting effect of the on-site dissipation on the crossover manifests as the delay in the melting of the singly-occupied Mott insulator in the ramp-down dynamics. In Figs. 4.4.5, we show the atom number per site $\langle\hat{n}_A\rangle$ and the condensate fraction $|\psi|^2/\langle\hat{n}_A\rangle$ as functions of the instantaneous lattice depth during the ramp-down dynamics. We clearly see that in the strong dissipation region the onset of the atom loss or the order parameter growth shifts to the side of small lattice depth as γ increases. This result suggests that one may experimentally observe the delay in the Mott-insulator melting by measuring the time evolution of the atom number and the momentum distribution during the ramp-down dynamics.

4.4.2 Experimental observation

We perform the experiment for measuring ramp-down dynamics across the crossover from the Mott insulator to the superfluid. The atom number and the momentum distribution during ramp-down dynamics are obtained from the fluorescence detection and the density distribution of the time-of-flight (TOF) absorption image, respectively. Our experiment starts with ramping up the lattice to $V_0 = 20\ E_R$ for preparation of the singly-occupied Mott insulator state. The atom number is tuned to be small enough that no doubly-occupied site exists. Subsequently we ramp down the lattice with applying the PA laser. The lattice ramp-down speed is $-2\,E_R$/ms. After ramping down the lattice to the final lattice depth, we perform the fluorescence detection for measuring the atom number, or we suddenly turn off all the trap and take the absorption image after 8 ms ballistic expansion

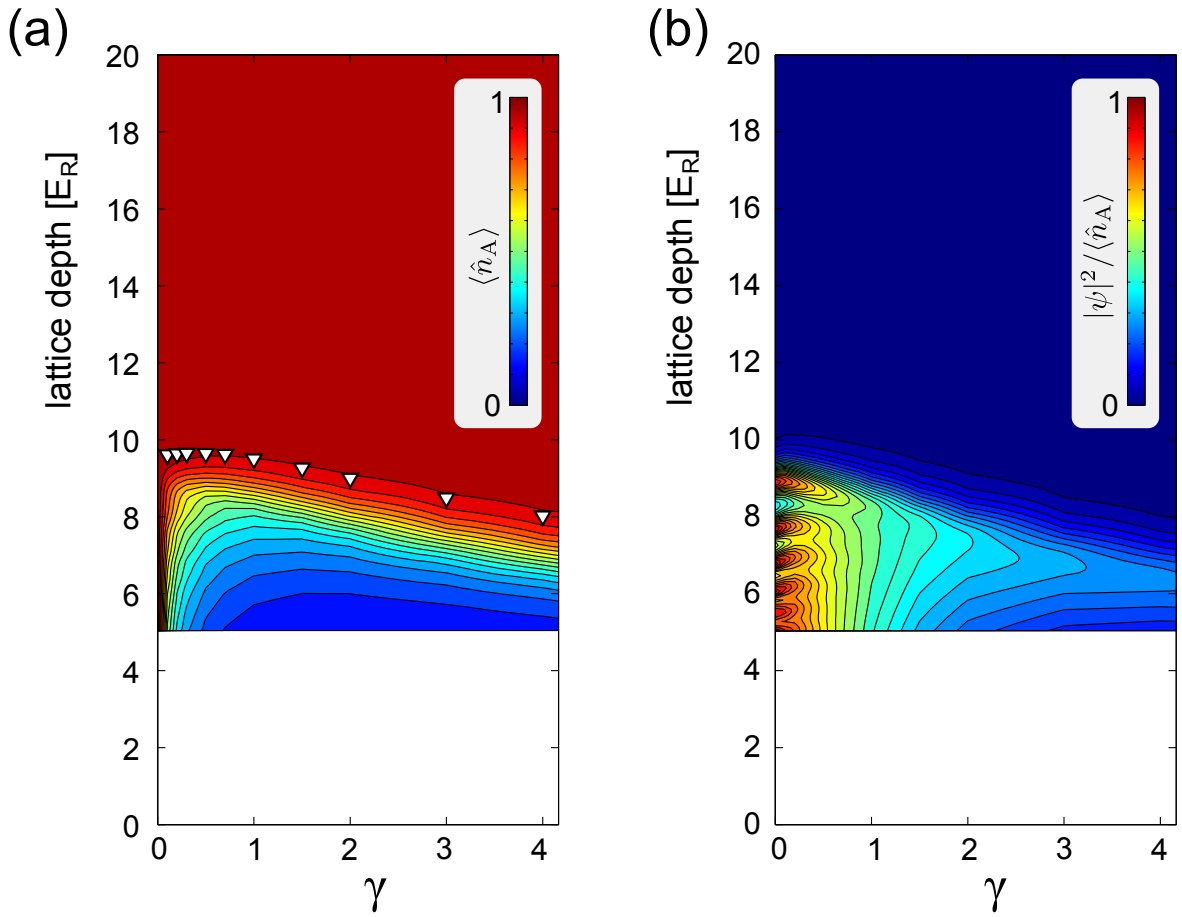

Figure 4.4.5: Numerical calculation of the atom number per site $\langle \hat{n}_{\mathrm{A}} \rangle$ (a) and the condensate fraction $|\psi|^2/\langle \hat{n}_{\mathrm{A}} \rangle$ (b) based on the dissipative Bose-Hubbard model with the Gutzwiller approximation. The time sequence of the lattice depth and the strength of the dissipation are set to be almost identical to those in the experiments.

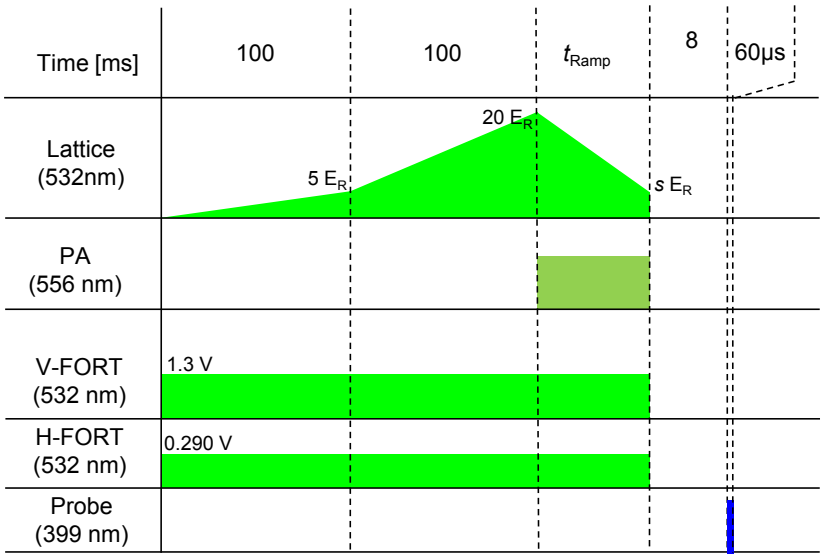

Figure 4.4.6: Experimental sequence for the observation of the effect of the dissipation on the quantum phase transition. The lattice ramp-down speed is $-2E_R$/ms and the ramp-down time is $t_{\mathrm{ramp}} = (20 - s)/2$ ms.

for obtaining the density distribution.

Atom number

We first focus on the atom loss measurement during ramp-down dynamics. Figure 4.4.7 shows the atom number measured with various dissipation strengths. The experimental result well reproduces the overall features of the calculation shown in Fig. 4.4.5 (a). Specifically, the significant atom loss starts around $V_0 = 10\ E_R$ in the presence of weak dissipation (②), while the atom number is conserved during ramping down the lattice without dissipation (①). This onset shifts to the deep lattice side as γ increases (③) for weak dissipation ($\gamma < 2$). However, when γ increases further from $\gamma \sim 2$, the onset shifts to the shallow lattice side (④). In order to identify the onset, we fit the double linear function to the data (Fig. 4.4.7 (b)). In the presence of on-site dissipation, the atom loss is correlated with the melting of the Mott insulator in ramp-down dynamics because the melting creates the double occupation which is blasted out by the PA laser. Our result suggests that the melting of the Mott insulator is delayed for strong on-site dissipation.

Quantitatively, the onset changes from $V_0 = 11.7(4)\ E_R$ to $V_0 = 9.2(4)\ E_R$ at the maximum as γ increases. This corresponds to the increase of zJ/U by a factor of 2.2. These behaviors capture the essence of the theoretical predictions mentioned in the above.

TOF abosorption images

Figure 4.4.8 shows a series of TOF absorption images obtained by changing the final lattice depth from Mott insulator regime to superfluid regime with various strength of the dissipation. Without dissipation, we clearly observe the transition from a Mott insulator state to a superfluid state as shown in Fig. 4.4.8 of $\gamma = 0$: in the deep lattice such as

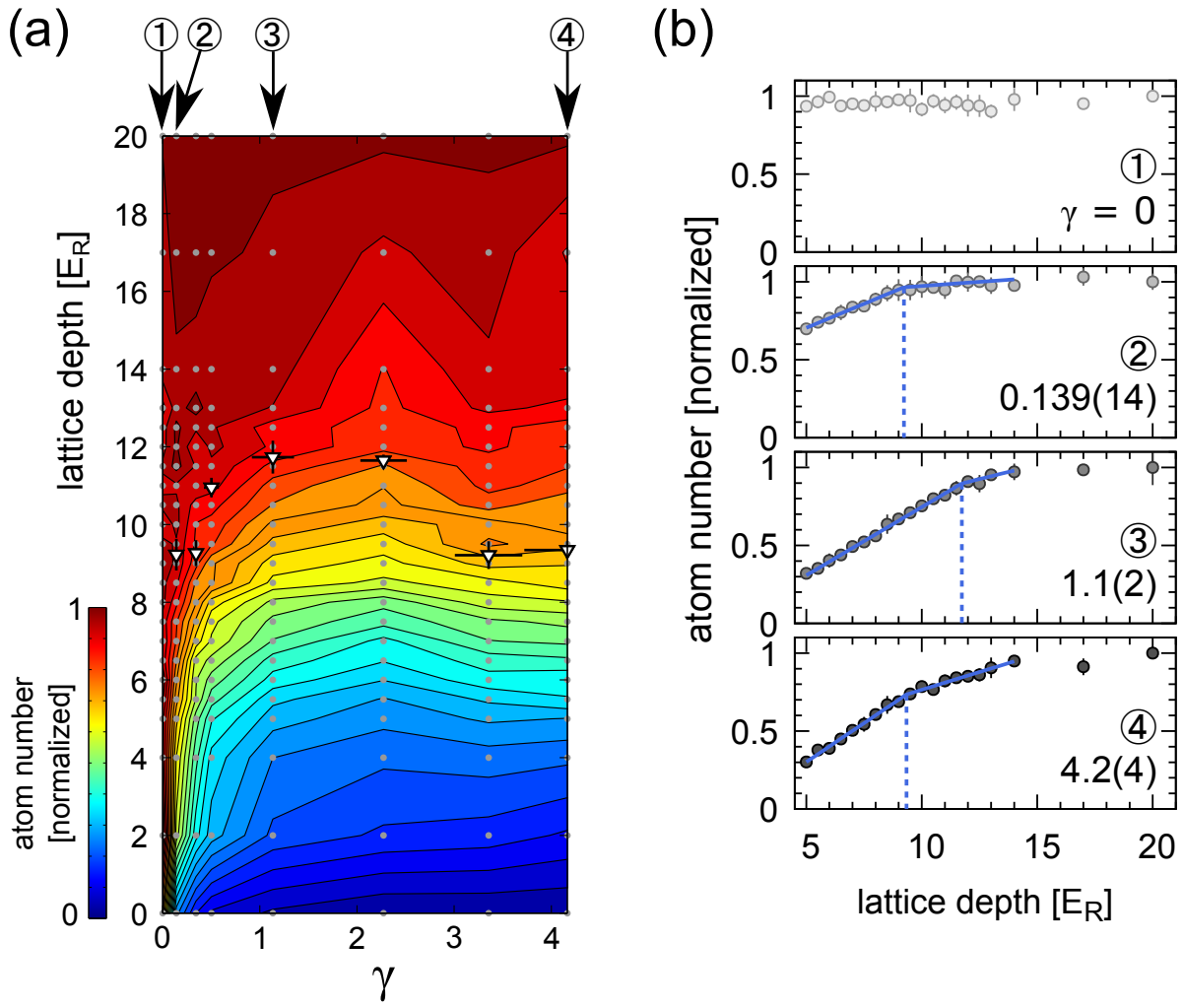

Figure 4.4.7: (a) Atom number diagram. The experimental data of the atom number are shown as the gray dots as a function of the final lattice depth for various strengths of dissipation, and are interpolated. The white triangles show the lattice depths at which the atom loss sets in, determined from the analysis in (b). The numbers ① to ④ correspond to the dissipation strengths for which the atom number changes are plotted in (b). (b) Temporal change of the atom number during a ramp-down sequence for four representative strengths of the dissipation. The atom number is normalized by the initial atom number at the lattice depth of $V_0 = 20\ E_R$. Blue lines are double linear fits to extract the onset of the atom loss, which are shown as dotted lines.

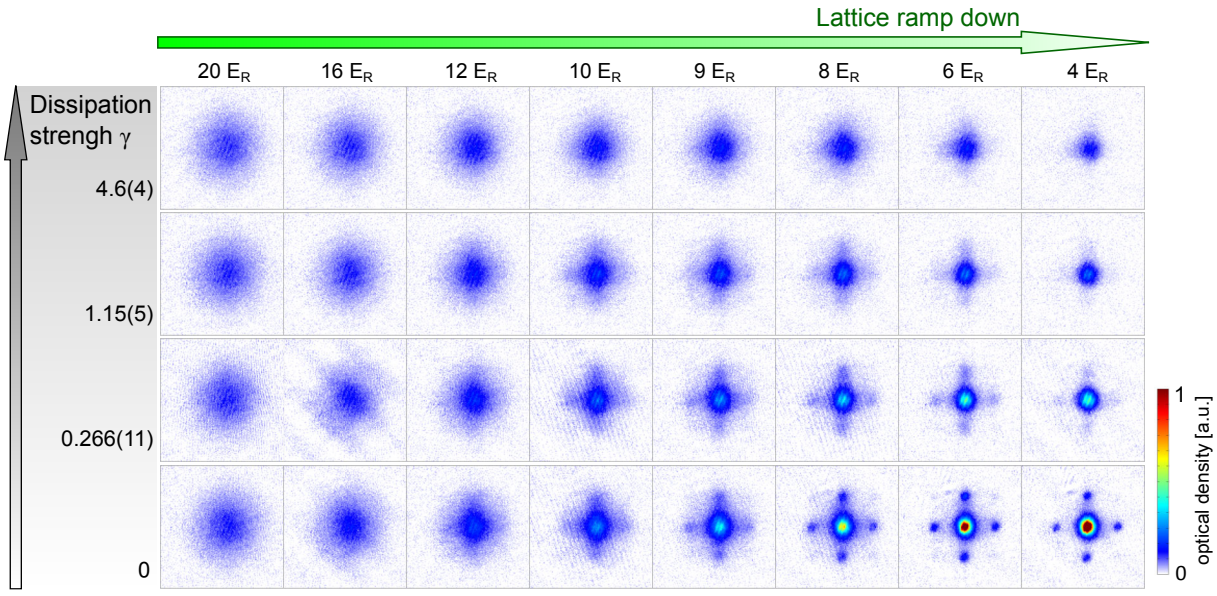

Figure 4.4.8: TOF absorption images. The images are taken with different final lattice depths and strengths of the dissipation, and averaged over 20 shots at each parameter.

$V_0 = 20\ E_R$, we obtain a broad distribution with no pattern, which indicates that the atoms have no phase coherence corresponding to the Mott insulator state. As ramping down the lattice across the critical depth of $V_0 = 11.3\ E_R$, which is calculated from the scattering length of $^1S_0$ state of ^{174}Yb [127], we obtain a clear interference pattern characterizing the presence of the phase coherence of the superfluid state. In the presence of dissipation, the observed transition is significantly modified. As the strength of the dissipation increases, the interference pattern becomes unclear in the shallow lattice regime. For strong dissipation such as $\gamma \sim 5$, any pattern cannot be observed. This result indicates that the growth of the phase coherence is suppressed by the strong dissipation.

Visibility of the interference pattern and width of the atom distribution

In order to evaluate the phase coherence quantitatively, we introduce the visibility of the interference peaks [101] as

$$v = \frac{N_{\max} - N_{\min}}{N_{\max} + N_{\min}}. \tag{4.4.5}$$

Here, $N_{\max}$ is the sum of the number of atoms in the regions of first-order interference peaks and $N_{\min}$ is the sum of the number of atoms in the regions at the same distance from the central peak along the diagonals. While the visibility increases with the ramp-down of the lattice, this increase becomes more moderate in the stronger dissipation, as shown in Fig. 4.4.9. Especially, clear dependence on the strength of the dissipation is observed below the depth of $V_0 = 11\ E_R$, which is around the calculated critical depth at $\gamma = 0$. As shown in Fig. 4.4.9, the effect of the dissipation on the width of the crossover region is observed as more moderate growing of the visibility below the depth of 11 E_R associated with the increase of γ.

In addition, as shown in Fig. 4.4.10, the dissipation moderates the narrowing of

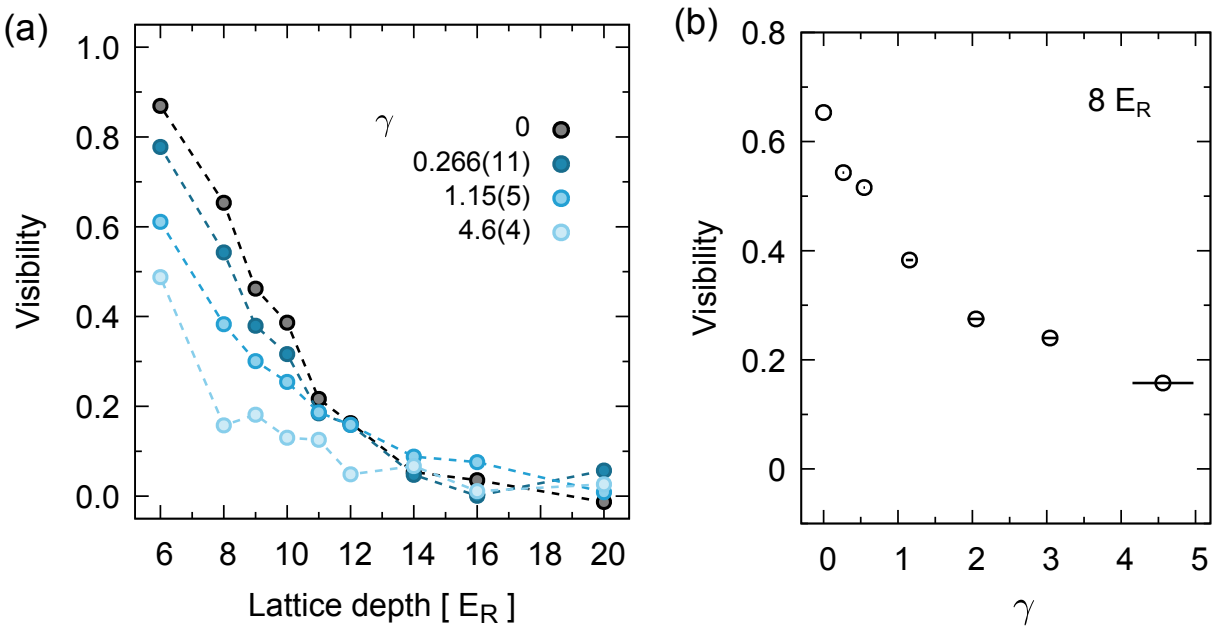

Figure 4.4.9: (a) Visibility of the interference peak of images. (b) Visibility as a function of the dissipation strength γ in the fixed lattice depth of 8 E_R.

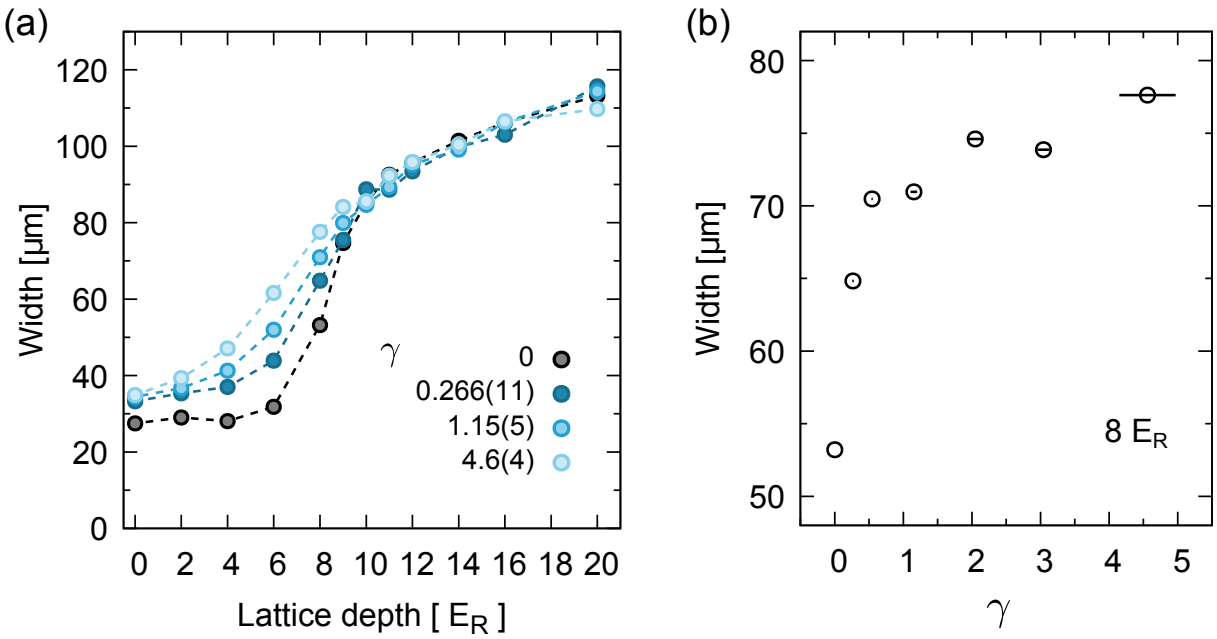

Figure 4.4.10: (a) Width of the density distribution, which is the full width at half maximum obtained by the Gaussian fitting. (b) Width as a function of the dissipation strength γ in the fixed lattice depth of 8 E_R.

the width (in μm) of the density distribution and the slope of the width (in μm) with respect to the lattice depth becomes less steep as γ increases. Narrowing the width of the distribution indicates the localization of the state in the momentum space.

All of these measurements support the delay in the melting of the singly-occupied Mott insulator in the ramp-down dynamics as an effect of the on-site dissipation as we see in the calculation of the condensate fraction shown in Fig. 4.4.5. Note that the observation of the excitation gap, which is the direct evidence of the formation of the Mott insulator, is difficult in this dissipative system because the excitation spectrum should have a broad linewidth determined by the inelastic collision rate Γ_{PA} of a few tens of kHz.

4.5 Quenching the dissipation

It is important to experimentally check whether this behavior is attributed to some heating effect by the PA laser. For this purpose, we measure the phase coherence after turning off the PA laser. If the absence of the interference pattern is attributed to the heating, the phase coherence is no longer restored after the PA laser is turned off. In contrast, if the state after the ramp-down of the lattice is still a Mott insulator, the phase coherence can be restored.

Similarly to the measurement of Fig. 4.4.8, we ramp down the lattice to a final lattice depth in $-2E_R$/ms with the maximum strength of dissipation $\gamma = 4.6(4)$. Then, we suddenly turn off the PA laser and investigate the subsequent time evolution of the atoms in the lattice by observing the phase coherence through a TOF absorption image at some hold time (Fig. 4.5.1 (a)).

The result for the case of the final lattice of $V_0 = 8\ E_R$ is shown in Fig. 4.5.1 (b) for the observed TOF images. After some hold time, an interference pattern grows. It serves as a direct signature of the restoration of the phase coherence, indicating that the absence of the interference pattern in Fig. 4.4.8 is not completely attributed to the heating.

We confirm that the total atom number is conserved in this dynamics as shown in Fig. 4.5.2. This means that the evaporative cooling which could possibly explain the observed behavior does not occur during the dynamics.

We consider the tunneling time as a relevant time scale because the superfluid state is realized through the process of delocalization of the particles by the tunneling. As shown in Figs. 4.5.3 (a) and (b), the time constant of the increase of the visibility and the decrease of the width is comparable to the tunneling time $(6J/\hbar)^{-1} = 0.21$ ms.

Figure 4.5.4 shows the visibility and the width of the density distribution, 0 ms and 4 ms after the ramp-down for various final lattice depths, similarly indicating the restoration of the coherence.

Importantly, the atoms after turning off the dissipation can be considered as an isolated (closed) system. Therefore, the observed dynamics in our experiment should not be considered as the usual thermal relaxation with the environment, but the relaxation in the isolated quantum system, which is a hot topic actively studied in recent experiments and theories [148, 149, 150, 151].

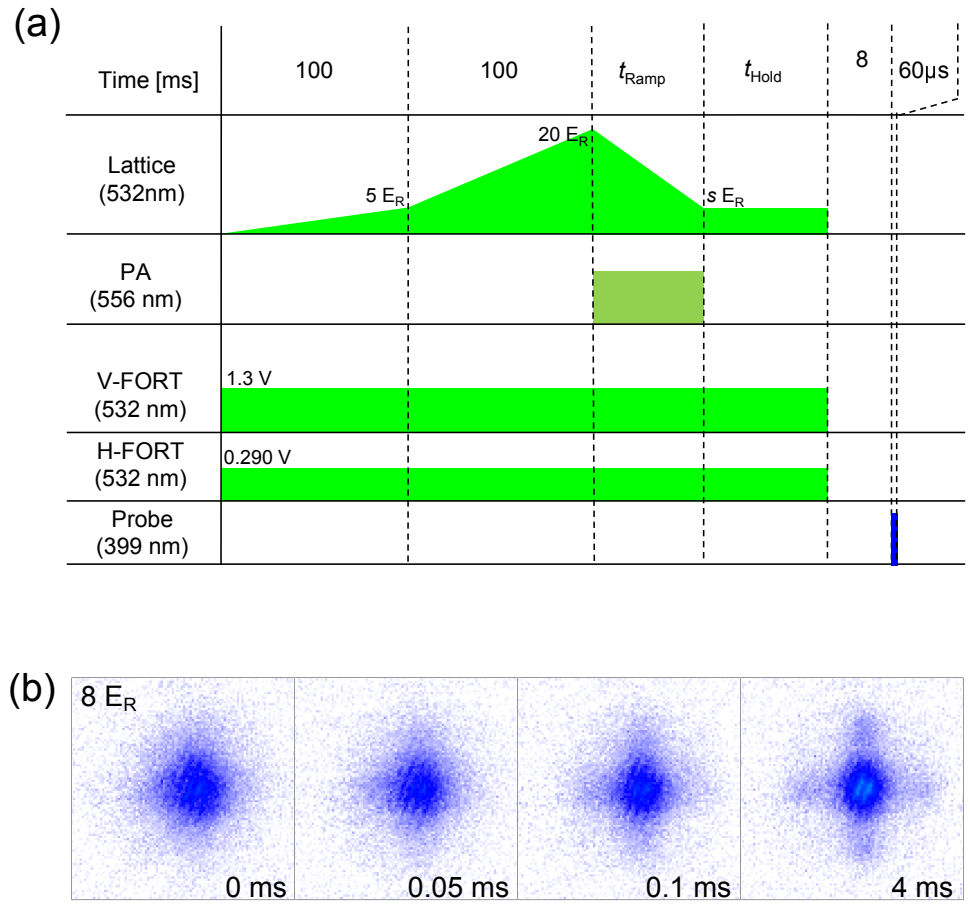

Figure 4.5.1: (a) Experimental sequence for the observation of the dynamics after turning off the dissipation. After ramping up the lattice to $V_0 = 20\ E_R$ for preparing the Mott insulator state, we ramp down the lattice to the final lattice depth $V_0 = s\ E_R$ with applying the PA laser. The ramp-down speed is $-2E_R/\mathrm{ms}$ and the ramp-down time is $t_{\mathrm{ramp}} = (20 - s)/2$ ms. After ramping down the lattice, we turn off the PA laser and hold the lattice for t_{hold}. (b) Time evolution of TOF image after turning off the dissipation. The final lattice depth is $V_0 = 8\ E_R$. The hold time after turning off the PA laser is shown at the bottom right of each image.

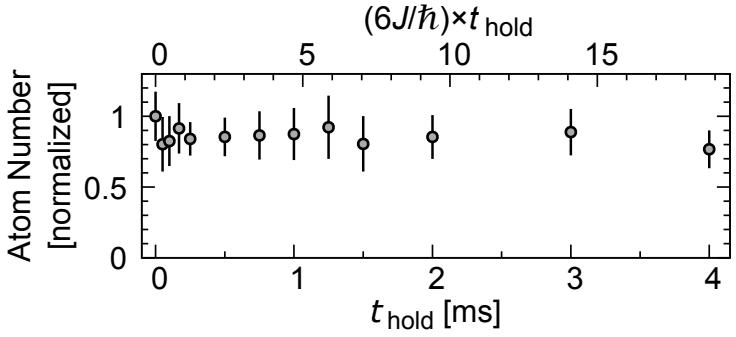

Figure 4.5.2: Atom number during after turning off the dissipation. The atom number is normalized by the initial atom number at $t_{\mathrm{hold}} = 0$ ms.

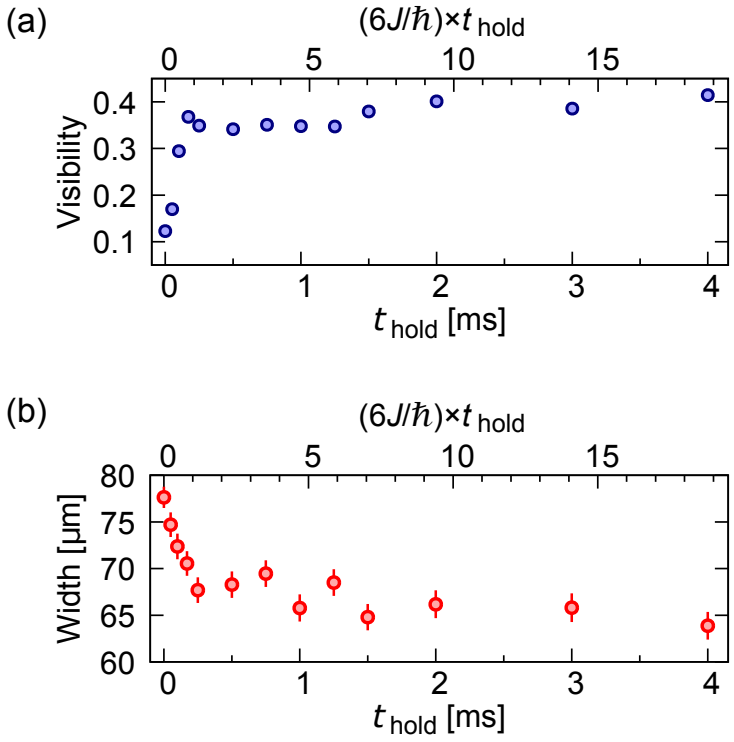

Figure 4.5.3: Time evolution of the visibility (a) and the width (b) after turning off the dissipation.

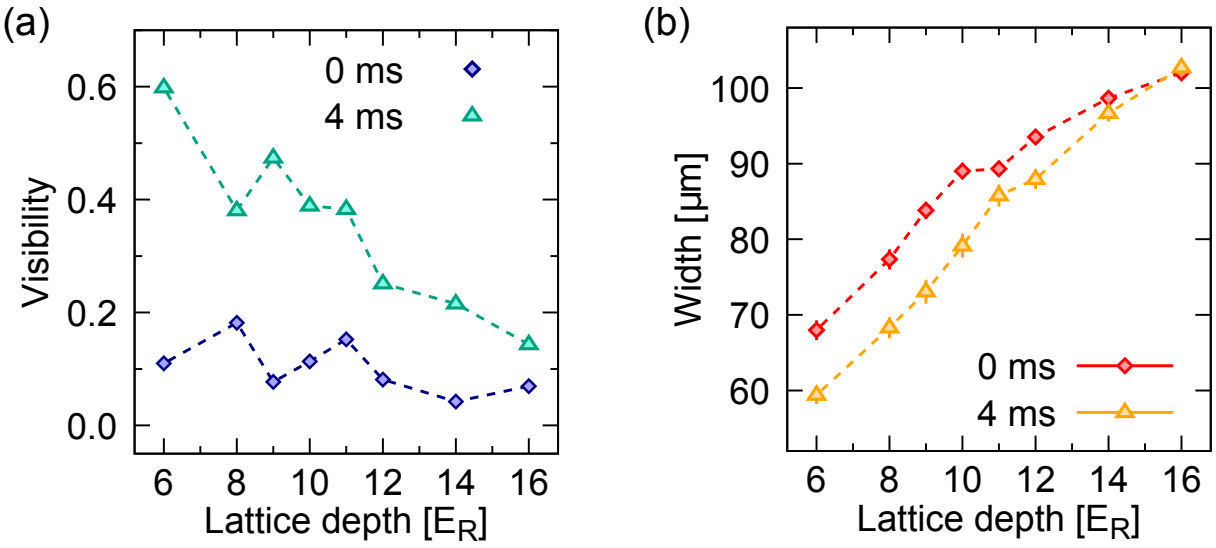

Figure 4.5.4: Lattice depth dependence of the visibility (a) and the width (b) with 0 ms and 4 ms hold time.

4.6 Conclusion and outlook

We have realized the engineered dissipative Bose-Hubbard system by introducing a controllable-strength two-body inelastic collision with use of a PA laser. By exploiting the highly controllable nature of the dissipation, we have investigated the effect of the dissipation on the quantum phase transition from the Mott insulator state to the superfluid state in the lattice ramp-down dynamics. We have observed that the melting of the Mott state is delayed and the growth of the phase coherence is suppressed for the strong on-site dissipation. The favored state depends on the type of the dissipation. For example, the stabilization of the superfulid state with use of a well-designed off-site dissipation is proposed [64]. Thanks to the dramatic change in the onset of the Mott-insulator melting, as shown in the fact of increase of zJ/U, we can access the interesting problem of quenching the dissipation across the crossover from the Mott insulator to the superfluid, where turning off the dissipation corresponds to a sudden parameter change of the Bose-Hubbard system [147]. In this method, the required time for turning off the dissipation could be very short while the sudden change of the depth of optical lattice needs a certain time in order to stabilize the power of the lattice laser as well as to prevent non-adiabatic inter-band transition. Moreover, while we have used ^{174}Yb, which is a bosonic isotope of an alkali-earth-like species, to demonstrate our method for controlling the dissipation, it is applicable generally to other atomic species that can be coupled to a state of lossy PA molecule. The crossover properties can also be caused by varying the on-site interaction. Controlling the on-site interaction with Feshbach resonance, for example using alkali atoms, enables us to investigate wider range of strength of dissipation including infinitely strong, since weakening the on-site interaction corresponds to strengthen the dissipation γ.

Chapter 5

Dissipative Bose-Hubbard system with intrinsic two-body loss

In this chapter, we report an experimental study of dynamics of the metastable $^3P_2$ state of ^{174}Yb in a 3D optical lattice. The intrinsic strong inelastic collision of the $^3P_2$ atoms realizes a dissipative Bose-Hubbard system with on-site two-body atom loss. First, we describe the measurement of the scattering length between two $^3P_2$ atoms a_{ee}. Because of the on-site interaction and the dissipation, the $^3P_2$ atoms are strongly correlated, which is revealed by the loss rate measurement described in Section 5.3. We observe the growth of the phase coherence and find its suppression owing to the dissipation, which is described in Section 5.4.

5.1 Bose-Hubbard system with intrinsic dissipation

The bosonic ^{174}Yb atoms in the $^3P_2$ state in the optical lattice can be regarded as the dissipative Bose-Hubbard system described by a master equation in Lindblad form [19]:

$$\hbar\frac{d\hat{\rho}}{dt} = -i[\hat{H},\hat{\rho}] + \mathcal{L}(\hat{\rho}), \tag{5.1.1}$$

where $\hat{H}$ is the Bose-Hubbard Hamiltonian

$$\hat{H} = \frac{U_{ee}}{2}\sum_j \hat{n}_j(\hat{n}_j - 1) - J\sum_{\langle j,k\rangle}(\hat{a}_j^\dagger \hat{a}_k + \text{h.c.}) + \sum_j(\epsilon_j - \mu)\hat{n}_j, \tag{5.1.2}$$

and $\mathcal{L}(\hat{\rho})$ represents the dissipation due to the inelastic collision between two atoms in the $^3P_2$ state

$$\mathcal{L}(\hat{\rho}) = \frac{\hbar\Gamma_{ee}}{4}\sum_j(-\hat{a}_j^\dagger\hat{a}_j^\dagger\hat{a}_j\hat{a}_j\hat{\rho} - \hat{\rho}\hat{a}_j^\dagger\hat{a}_j^\dagger\hat{a}_j\hat{a}_j + 2\hat{a}_j\hat{a}_j\hat{\rho}\hat{a}_j^\dagger\hat{a}_j^\dagger). \tag{5.1.3}$$

U_{ee}, J, and Γ_{ee} represent the on-site interaction, the tunneling amplitude, and the inelastic collision rate, respectively. Index e (g) denotes $^3P_2$ ($^1S_0$) state. $\hat{a}_j$ is the annihilation operator of the $^3P_2$ state atoms at a site j and $\hat{n}_j = \hat{a}_j^\dagger\hat{a}_j$. We note that there exists the one-body loss process due to the photon scattering and the spontaneous emission, the loss rate of which is $1 \sim 2$ order of magnitude smaller than the two-body loss rate (The detail is described in Section 5.3).

5.2 Measurement of the scattering length a_{ee}

For the full characterization of the system, it is necessary to measure the strength of the on-site interaction between the $^3P_2$ state atoms. This has never been done because of the difficulty associated with the rapid loss of atoms in the $^3P_2$ state due to the large inelastic collision. We determine the scattering length between the $^3P_2$ state by establishing a new spectroscopic technique with double-excitation process by utilizing the inelastic loss property.

We start with a preparation of the Mott insulating state of the $^1S_0$ atoms with singly- and doubly-occupied sites at the lattice depth of $V_0 = 18\ E_R$ for the $^1S_0$ state. Because the polarizability of the $^3P_2$ state for the 532 nm lattice beam is different from that of the $^1S_0$ state, the lattice depth depends on the atomic state, which is taken into account in the determination of the lattice depth and the calculation of the interaction.

The polarizability of the $^3P_2$ state for the 532 nm lattice beam depends on the magnetic sublevel m_J and the angle between the quantization axis and the polarization of the lattice beam $\theta_{x,y,z}$. In our experiment, the polarizability of the $^3P_2$ state is $(\alpha_{e,x}, \alpha_{e,y}, \alpha_{e,z})/\alpha_g = (1.43(5), 1.43(5), 1.132(8))$ (see Appendix D). Here, α_g is the polarizability of the $^1S_0$ state and $(\theta_x, \theta_y, \theta_z) = (0°, 0°, 90°)$. For example, in the spectroscopy, the lattice depth of $V_0 = 18\ E_R$ for the $^1S_0$ state corresponds to $(V_{0x}, V_{0y}, V_{0z}) = (25.7, 25.7, 20.4)\ E_R$ for the $^3P_2$ state.

We then excite a single $^1S_0$ state atom in the doubly-occupied sites into the $^3P_2$ state by adiabatic rapid passage (ARP) with a frequency-swept pulse with a 507 nm laser under a bias magnetic field of 200 mG along z axis, which is more robust than the π-pulse excitation against the fluctuation of the frequency and the intensity of the excitation laser. We perform the experiment with the atoms in the magnetic sublevel of $m_J = -2$. The atoms in the singly-occupied sites are not excited because of the well-separated resonance frequencies between the singly- and doubly-occupied sites due to the interaction (see Fig. 5.2.1 (c)). Subsequently, we apply the second excitation pulse with a variable frequency. If the second pulse successfully excites a remaining $^1S_0$ state atom in the doubly-occupied sites, two $^3P_2$ state atoms occupy the same site, resulting in the strong atom loss due to the inelastic collision with the rate Γ_{ee} (Fig. 5.2.1 (a)). In the optical lattice, Γ_{ee} is determined by the inelastic collision coefficient β_{ee} and the confinement of the lattice potential through the relation $\Gamma_{ee} = \beta_{ee} \int |w(\boldsymbol{r})|^4 d\boldsymbol{r}$, where $w(\boldsymbol{r})$ is the Wannier function of the lowest band. β_{ee} is expected to a half of the inelastic collision coefficient with a thermal gas $\beta_{ee}^{\mathrm{thermal}} = 5.1(6) \times 10^{-11}\mathrm{cm}^3/\mathrm{s}$ [91, 152].

For the detection, atoms in the excited $^3P_2$ state are repumped back to the $^1S_0$ state using repump laser of 649 nm and 770 nm. Finally, the number of the repumped $^1S_0$ atoms are measured by the fluorescence imaging using the $^1S_0 - {}^1P_1$ transition.

Figure 5.2.1 (b) shows the spectrum of the above-mentioned double-excitation spectroscopy. We observe a large dip around +10 kHz detuning from the $^1S_0 - {}^3P_2$ transition of the singly-occupied atoms, which does not have the counterpart in the spectrum of the low-intensity single pulse spectroscopy (Fig. 5.2.1 (c)). For precise determination of the on-site interaction, we take four data. Because the first ARP excitation is sensitive to the laser frequency, we evaluate the excitation efficiency and its fluctuation, which are represented as the offset (dashed line) and the errorbars of the data points, respectively. For each result of the spectroscopy, we fit the data to multiple Lorentzian functions with

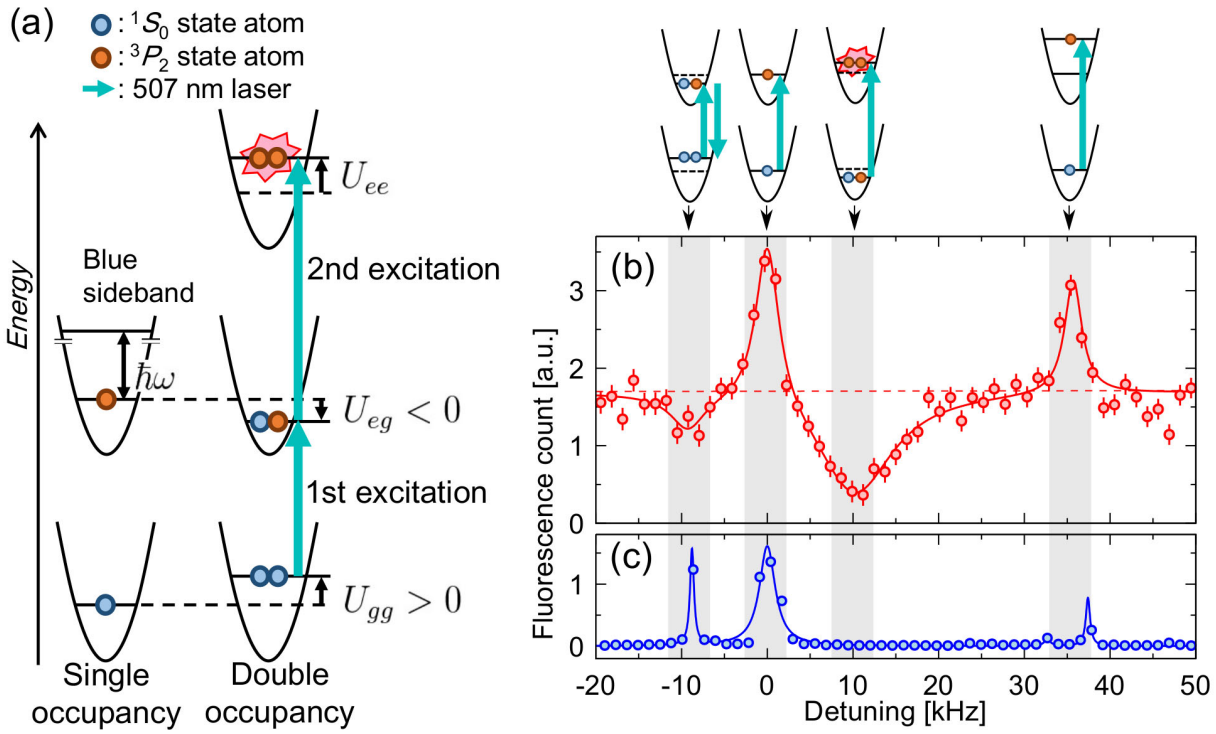

Figure 5.2.1: (a) Schematic of the double-excitation spectroscopy. The on-site interaction strength manifests itself in the shift of the excitation frequency at the doubly-occupied sites, which differs from the excitation frequency of the atoms at the singly-occupied site. (b) The spectrum of the double-excitation spectroscopy. We subtract the fluorescence count measured after the first excitation, which corresponds to the atoms excited by the first pulse. The horizontal axis represents the detuning of the second-excitation pulse frequency from the transition of the atoms in the singly-occupied sites. The resonance observed in the negative detuning corresponds the de-excitation from the $^1S_0 + {}^3P_2$ state to the $^1S_0 + {}^1S_0$ state and peak around +35 kHz represents the excitation for the blue-sideband. (c) The spectrum of the single-excitation spectroscopy for comparison.

the error, from which we obtain the center positions of the peaks and the errors with 4-5%. Finally, by calculating the weighted average of the four results, we determine the value of on-site interaction with the error of $\sim 1\%$. From these data, we determine the interaction shifts as follows:

$$\frac{U_{ee} - U_{eg}}{h} = +10.7(3)\ \text{kHz}, \tag{5.2.1}$$

$$\frac{U_{eg} - U_{gg}}{h} = -9.70(5)\ \text{kHz}. \tag{5.2.2}$$

From these results and the known scattering length $a_{gg} = +104.9(1.5)a_0$ [127], we obtain the scattering lengths

$$a_{eg} = -201.5(1.5)a_0 \tag{5.2.3}$$

and

$$a_{ee} = +110(8)a_0, \tag{5.2.4}$$

where a_0 is the Bohr radius. Here we calculate the scattering lengths using the relations

$$U_{ee} = \frac{4\pi\hbar^2 a_{ee}}{m} \int |w_e(\boldsymbol{r})|^4 d\boldsymbol{r}, \tag{5.2.5}$$

$$U_{eg} = \frac{4\pi\hbar^2 a_{eg}}{m} \int |w_e(\boldsymbol{r})|^2 |w_g(\boldsymbol{r})|^2 d\boldsymbol{r} \tag{5.2.6}$$

and

$$U_{gg} = \frac{4\pi\hbar^2 a_{gg}}{m} \int |w_g(\boldsymbol{r})|^4 d\boldsymbol{r}, \tag{5.2.7}$$

where $w_g(\boldsymbol{r})$ and $w_e(\boldsymbol{r})$ represent the Wannier function of the ${}^1S_0$ state and the ${}^3P_2$ state, respectively.

The obtained scattering length a_{ee} shows that the on-site interaction between the ${}^3P_2$ atoms is repulsive and comparable to the dissipation strength: the dimensionless dissipation strength is $\hbar\Gamma_{ee}/U_{ee} = 0.94(13)$, which does not depend on the lattice depth.

5.3 Strong correlation between the ${}^3P_2$ atoms

5.3.1 Measurement of the two-body loss rate

As the basic property of the dissipative quantum many-body system, we first study the stability of the unit-filling Mott insulating state in the presence of the two-body dissipation. Here, we measure the loss rate, which varies as a function of the lattice depth because J, U_{ee}, and Γ_{ee} depend on the lattice depth.

We first prepare the unit-filling Mott insulating state of the ${}^3P_2$ state in almost the same manner as in the double-excitation spectroscopy, except that the lower atom number is loaded so that the doubly-occupied sites are not created, which is confirmed by the occupancy-sensitive spectroscopy [43]. After ramping up the lattice, we excite the atoms to the ${}^3P_2$ state by the ARP. The remaining ${}^1S_0$ atoms are blasted by applying 399-nm resonant light. The atom number in the ${}^3P_2$ state $N(t)$ decreases as

$$\frac{dN(t)}{dt} = -\frac{n_0\kappa}{N(0)} N(t)^2 - \xi N(t), \tag{5.3.1}$$

where κ is two-body loss rate and ξ is one-body loss rate. n_0 is initial filling factor estimated by the ARP excitation efficiency, which is typically 90 %. The one-body loss is mainly induced by the photon scattering with the ${}^3P_2 - {}^3S_1$ transition at 770 nm caused by the 532-nm lattice beam, the rate γ_{sc} of which depends on the intensity of the lattice beam I as follows:

$$\gamma_{\mathrm{sc}} = \frac{3\pi c^2 \Gamma_{\mathrm{nat}}^2}{2\hbar\omega_0^3} \left(\frac{\omega}{\omega_0}\right)^3 \left(\frac{1}{\omega - \omega_0} - \frac{1}{\omega + \omega_0}\right)^2 I, \tag{5.3.2}$$

where Γ_{nat} is the natural linewidth, ω is the oscillation frequency of the lattice beam and ω_0 is the oscillation frequency of the transition line. The spontaneous emission rate is $\gamma_{\mathrm{sp}} = 67(7)$ mHz [132]. The one-body loss rate is given by $\xi = \gamma_{\mathrm{sc}} + \gamma_{\mathrm{sp}}$, which is calculated up to $\sim$0.3 Hz.

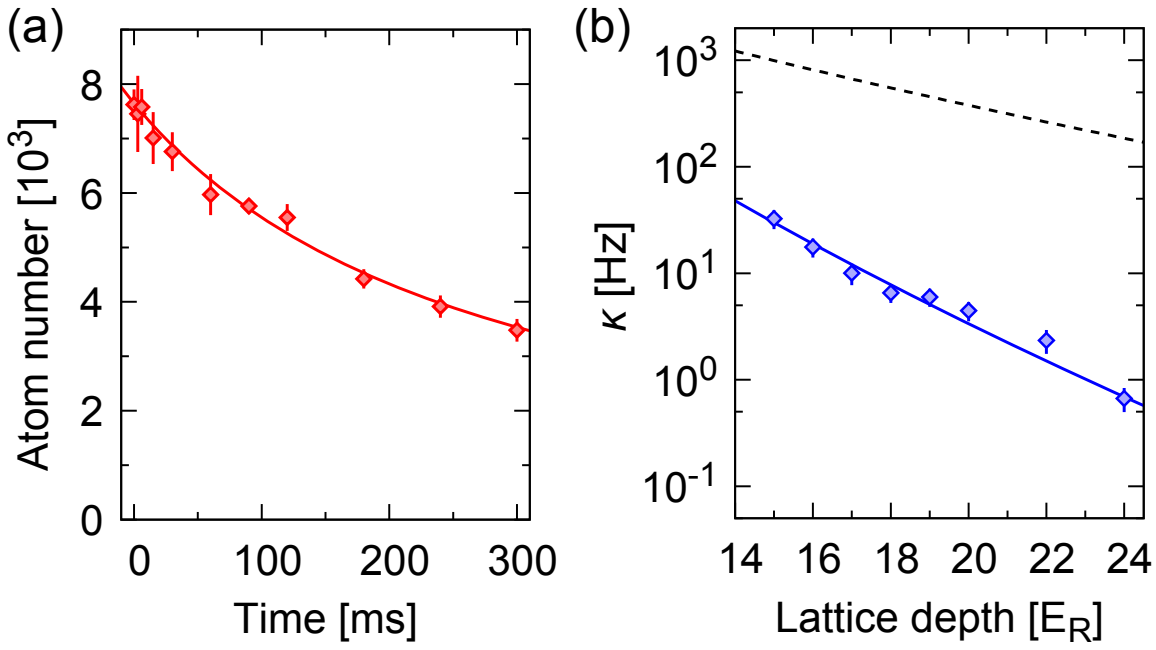

Figure 5.3.1: (a) Time dependence of the remaining $^3P_2$ atoms at $V = 19E_R$. The solid line shows a fit of Eq. (5.3.1) to the experimental data. (b) Two-body loss rate as a function of the lattice depth. The solid line shows a fit of Eq. (5.3.4) to the experimental data and the dashed line is the tunneling rate $6J/\hbar$ for comparison. The lattice depths are adjusted for the $^3P_2$ state.

The analytical solution to the Eq. 5.3.1 is

$$N(t) = N(0)\left[\left(1+\frac{n_0\kappa}{\xi}\right)e^{\xi t} - \frac{n_0\kappa}{\xi}\right]^{-1} \tag{5.3.3}$$

which is used for the fitting to the experimental data.

Figure 5.3.1 (a) shows the typical decay of the atom number of the $^3P_2$ state. By fitting Eq. (5.3.2) to the data with the calculated one-body loss rate ξ, we extract the two-body loss rate κ (see Fig. 5.3.1 (b)). The loss rate κ is suppressed compared with the tunneling rate $6J/\hbar$ (see Fig. 5.3.1 (b)), which naïvely characterizes the time scale of the creation of the double occupancy. In the sufficiently deep lattice, κ can be suppressed to the order of Hz.

This suppression is attributed to the formation of strong correlation. When the tunneling is much smaller than the other energy scales ($J \ll \hbar\Gamma_{ee}, U_{ee}$), κ is given by [74, 143]

$$\kappa = \frac{16z(J/\hbar)^2}{\Gamma_{ee}}\left[1+\left(\frac{2U_{ee}}{\hbar\Gamma_{ee}}\right)^2\right]^{-1}. \tag{5.3.4}$$

Here, $z = 6$ is the coordination number. We fit Eq. (5.3.4) to the data with the fitting parameter of β_{ee}. The best-fit value is $\beta_{ee} = 2.5(6) \times 10^{-11}$ cm^3/s, which is well agree with half of $\beta_{ee}^{\mathrm{thermal}} = 5.1(6) \times 10^{-11}$cm^3/s [91, 152].

We note that the strength of the inelastic collision does not achieve the quantum Zeno region as the previous experiments [74, 76] and our experiment with the PA (see Chapter

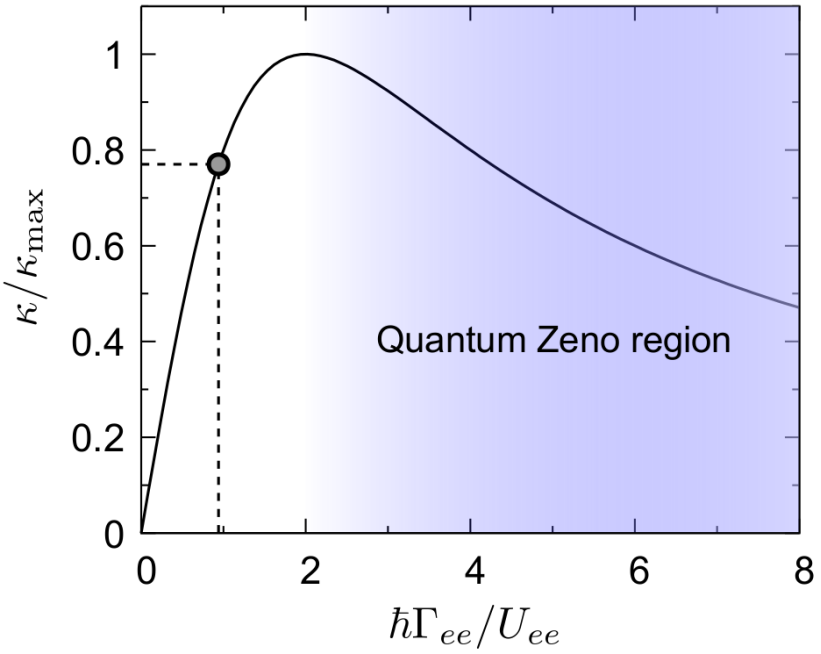

Figure 5.3.2: Loss rate κ (Eq. 5.3.4) normalized by the maximum loss rate $\kappa_{\max}$ as a function of the dissipation strength $\hbar\Gamma_{ee}/U_{ee}$. The point plotted on the curve indicates our experimental parameter of $\hbar\Gamma_{ee}/U_{ee} = 0.94(13)$ in this experiment.

4), in which κ decrease as the strength of the dissipation increases. Figure 5.3.2 shows the loss rate κ (Eq. 5.3.4) normalized by the maximum loss rate $\kappa_{\max}$ as a function of the dissipation strength. In the region of $\hbar\Gamma_{ee}/U_{ee} \geq 2$, which we call the quantum Zeno region, κ decreases as $\hbar\Gamma_{ee}/U_{ee}$ increases, which is the manifestation of the quantum Zeno effect. On the other hand, this suppression does not occur as $\hbar\Gamma_{ee}/U_{ee}$ increases in the region around our experimental parameter of $\hbar\Gamma_{ee}/U_{ee} = 0.94(13)$.

5.3.2 Pair correlation function $g^{(2)}(0)$

In order to evaluate the correlation quantitatively, we introduce the pair correlation function between two particles placed at site i and j

$$g^{(2)}(i,j) \equiv \frac{\langle \hat{a}_i^\dagger \hat{a}_j^\dagger \hat{a}_j \hat{a}_i \rangle}{\langle \hat{a}_i^\dagger \hat{a}_i \rangle \langle \hat{a}_j^\dagger \hat{a}_j \rangle}. \tag{5.3.5}$$

In this analysis, we use the pair correlation function of the two particle at the same site $g^{(2)}(0) \equiv g^{(2)}(i,i)$ to characterize the reduction of the double occupation arising from the interaction between the atoms. $g^{(2)}(0)$ can be written as follows:

$$g^{(2)}(0) \equiv \frac{\langle \hat{n}_i(\hat{n}_i - 1) \rangle}{\langle \hat{n}_i \rangle^2}. \tag{5.3.6}$$

This value can be estimated from the experimental result according to the relation [74, 143]

$$g^{(2)}(0) = \frac{\kappa}{\Gamma_{ee}}. \tag{5.3.7}$$

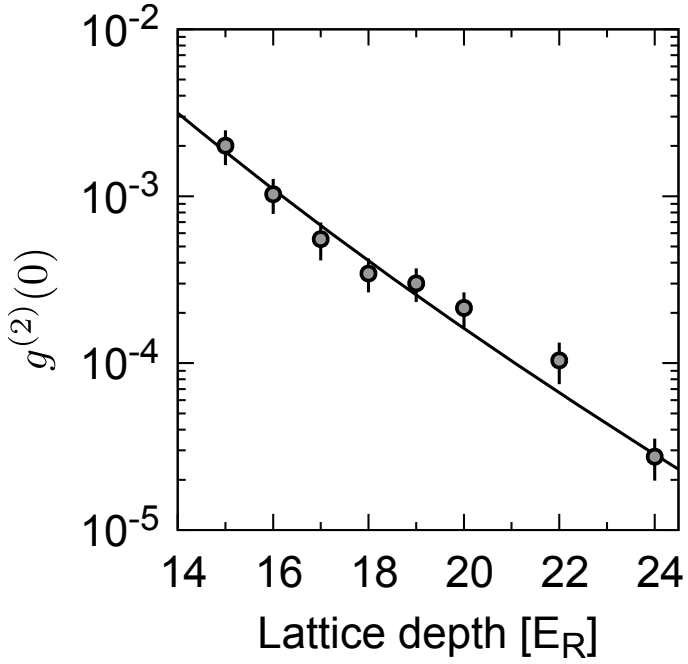

Figure 5.3.3: Pair correlation function $g^{(2)}(0)$ calculated from the data in the loss rate measurement. The solid line represents the theoretical calculation with β_{ee} obtained from the data in Fig. 5.3.1.

Figure 5.3.3 shows that $g^{(2)}(0)$ is much smaller than 1, which means that the creation of the double occupation is strongly suppressed. From Eq. (5.3.4) we can derive the following representation

$$g^{(2)}(0) = \frac{4zJ^2}{\left(\frac{\hbar\Gamma_{ee}}{2}\right)^2 + U_{ee}^2}, \tag{5.3.8}$$

which shows that the reduction of the $g^{(2)}(0)$ is attributed to both of the on-site elastic interaction U_{ee} and the inelastic loss $\hbar\Gamma_{ee}$. In our experimental parameter of $\hbar\Gamma_{ee}/U_{ee} = 0.94(13)$, the inelastic interaction contributes to the formation of the correlation in addition to the elastic interaction.

5.3.3 Dependence of the tunneling on the neighboring site occupation

In order to confirm that the suppression of the doubly-occupied sites is not due to the reduction of the tunneling amplitude itself but due to the correlation effect as a result of the occupation of the atoms in the nearest neighboring site, we observe the tunneling dynamics from the initial state in which there is no atom in the nearest neighboring sites along one direction.

After preparing the Mott insulating state with the $^1S_0$ atoms, we form the optical superlattice by adding the long lattice with 1064 nm laser along the x axis with the relative phase between two lattice beam adjusted to make potential difference between A and B layers. The polarizability of the $^1S_0$ state for 1070 nm is $\alpha_g^{1070} = 6.3\text{Hz}/(\text{W}/\text{cm}^2)$

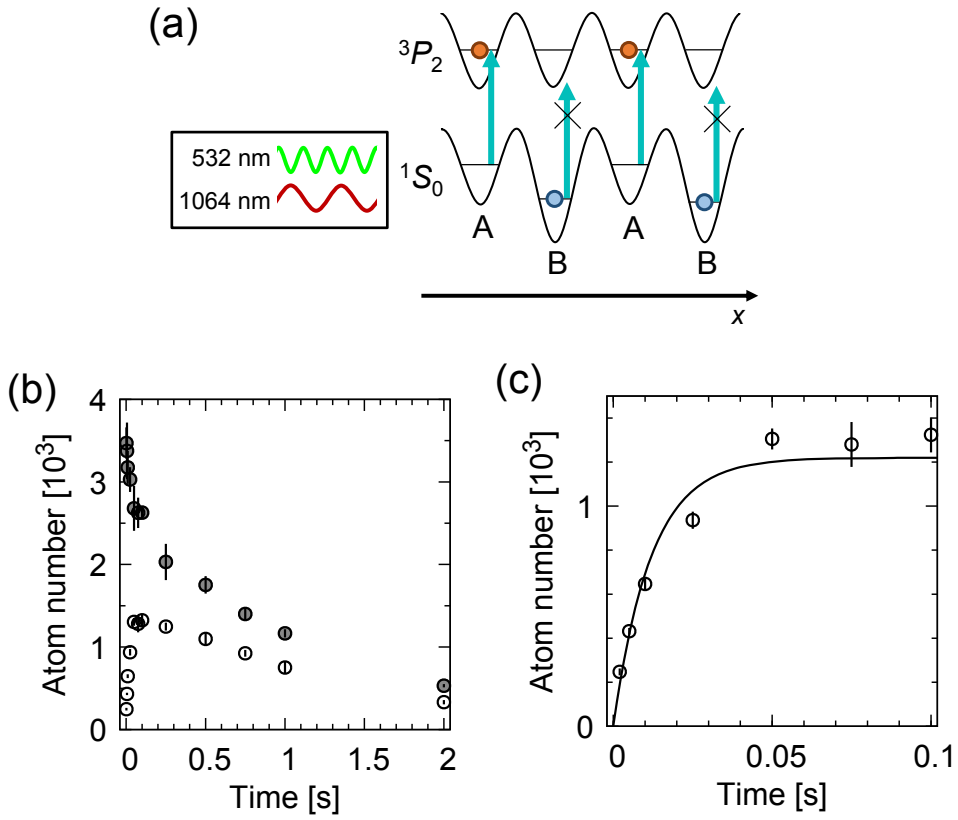

Figure 5.3.4: (a) Schematic of the selective excitation using a superlattice. The potential difference between the A and B layers created by the long lattice allows us to excite the atoms only in the A layer. (b) Time dependence of the atom number in the A layer (white circle) and B layer (gray circle) at $V_0 = (19.0, 19.0, 19.9)E_R$ for the $^3P_2$ state. We note that the difference of the transfer efficiency between the A and B layers causes the remaining imbalance for longer times. (c) The initial 0.1 sec data of the atom number in the B layer and the fitting of the exponential function. Note that we also observe the slow decrease of the atom number due to the two-body loss at later time that the population imbalance is already reduced.

while that of $^3P_2$ is $\alpha_e^{1070} = 0.0(4)\text{Hz}/(\text{W}/\text{cm}^2)$ with the angle between the quantization axis and the polarization of the lattice beam of 0° in our condition [153]. Since 1064 nm is close to the 1070 nm without any resonance line around these frequencies, the 1064 nm lattice forms the deep optical lattice mainly for the $^1S_0$ state only, which separates the excitation frequency (Fig. 5.3.4 (a)). We can selectively excite the atoms to the $^3P_2$ state only in the A layer with ARP and blast the remaining $^1S_0$ atoms. Then, we remove the additional lattice and monitor the atom number. The detection is also selectively performed with the coherent transfer to the $^1S_0$ state using the ARP.

We observe fast decrease of the atom number in the A layer and increase of the atom number in the B layer (Fig. 5.3.4 (b)), which indicate the tunneling of the atoms along the x axis. In general, it is difficult to calculate the behavior of the relaxation dynamics from the imbalanced initial state. In our experiments, we allow the tunneling along the y and z axes, thus the dynamics is rather complex. In this analysis, we simply describe the

tunneling behavior as follows:

$$\begin{aligned} \frac{dN_{\mathrm{A}}(t)}{dt} &= -RN_{\mathrm{A}}(t) + RN_{\mathrm{B}}(t), \\ \frac{dN_{\mathrm{A}}(t)}{dt} &= RN_{\mathrm{A}}(t) - RN_{\mathrm{B}}(t). \end{aligned} \tag{5.3.9}$$

Here, $N_{A\ (B)}$ is the atom number in the A (B) layer, and R represents the tunneling rate between the A and B layers. With the initial condition that all atoms are placed in the A layer, Eq. (5.3.9) yields

$$N_{\mathrm{A}}(t) = \frac{N_0}{2}[1 + \exp(-2Rt)] \tag{5.3.10}$$

and

$$N_{\mathrm{B}}(t) = \frac{N_0}{2}[1 - \exp(-2Rt)], \tag{5.3.11}$$

where N_0 is the initial atom number. We fit this function to the initial 0.1 s data of the atom number in the B layer, as shown in the inset of Fig. 5.3.4 (b). From the fitting, we obtain the tunneling rate of $R = 42(6)$ Hz, which is much larger than the observed κ in the case of the unit-filling Mott insulator (see Fig. 5.3.1 (b)) and is consistent with the relaxation time scale $4J/h = 50$ Hz discussed in Ref [154].

5.4 Effect of the intrinsic dissipation on the Mott insulator - superfluid transition

5.4.1 Time-of-Flight images

We also investigate the effect of the dissipation on the quantum phase transition from the Mott insulator to the superfluid state. We first prepare the unit-filling Mott insulator of the $^3P_2$ state in the same manner as the preparation of the initial state of the loss rate measurement. The lattice depth is $V_0 = 20\ E_R$ for the $^3P_2$ state. Then we ramp down the lattice, in which the lattice ramp-down speed is $-2\ E_R$/ms. The atom number and the momentum distribution during the ramp-down dynamics are obtained from the density distribution of the time-of-flight (TOF) absorption image. After ramping down the lattice to the final lattice depth, we suddenly turn off all the trap and take the image after 6-ms expansion of the atom cloud (Fig. 5.4.2 (a)). The atoms in the $^3P_2$ state are repumped back to the $^1S_0$ state 1 ms before taking the absorption image. For comparison, we observe the atoms in the dissipationless $^1S_0$ state. We compare the two results as a function of the lattice depths because the scattering lengths a_{ee} and a_{gg} are almost the same within the error: $a_{ee}/a_{gg} = 1.05(7)$. The lattice depth is adjusted for each state.

Without dissipation (the $^1S_0$ state), around $V_0 \sim 10\ E_R$ we observe the transition from a MI with a broad distribution to the SF with a clear interference pattern characterizing the presence of the phase coherence, which is consistent with the theoretical value of the critical lattice depth of $V_0 = 11.29(16)\ E_R$. On the other hand, the atom distribution of the dissipative $^3P_2$ state is modified. Although we still observe the anisotropic interference pattern in the shallow lattice region, the interference pattern is unclear.

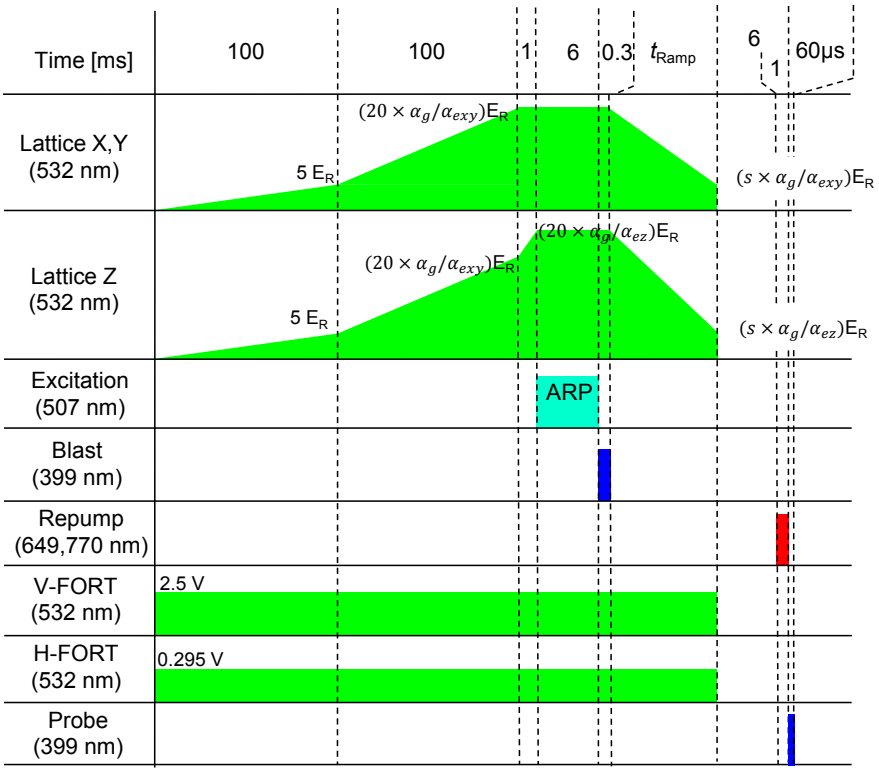

Figure 5.4.1: Experimental sequence for the observation of the effect of the intrinsic dissipation on the quantum phase transition. The lattice ramp-down speed is $-2\ E_R$/ms and the ramp-down time is $t_{\mathrm{ramp}} = (20 - s)/2$ ms. First, we ramp up the lattice whose depths are isotropic for the $^1S_0$ state. Because of the difference of the polarizability between the $^1S_0$ state and the $^3P_2$ state, we adjust the lattice depth immediately before the excitation in order to create isotropic lattice for the $^3P_2$ state. The lattice depths shown in the figure represent the value for the $^1S_0$ state. α_g, α_{exy} and α_{ez} are the polarizability of the $^1S_0$ state, that of the $^3P_2$ state for x, y-lattice, and that of the $^3P_2$ state for z-lattice, respectively.

5.4.2 Quantitative analysis

For the quantitative analysis, we evaluate the atom number, the visibility of the interference peaks, and the width of the atom distribution obtained by the TOF images (Fig. 5.4.3 (a-c)). For the $^3P_2$ system, the number of atoms starts to decrease around $V_0 = 10\ E_R$. This significant atom loss reflects the start point of the melting of the Mott insulator, which creates the double occupation. The definition of the visibility is given in Eq. 4.4.5. In both cases, the visibility increases with the ramp-down of the lattice. This increase in the $^3P_2$ state is more moderate compared to that in the $^1S_0$ state (Fig. 5.4.2 (b)). In addition, the narrowing of the width of the density distribution is also more moderate in the case of the $^3P_2$ state (Fig. 5.4.2 (c)). These results suggest that the growth of the phase coherence is suppressed by the intrinsic on-site two-body dissipation. Similar behavior is observed in the dissipative Bose-Hubbard system with the artificial dissipation (Chapter 4), where the two-body loss is artificially introduced using the photo-association

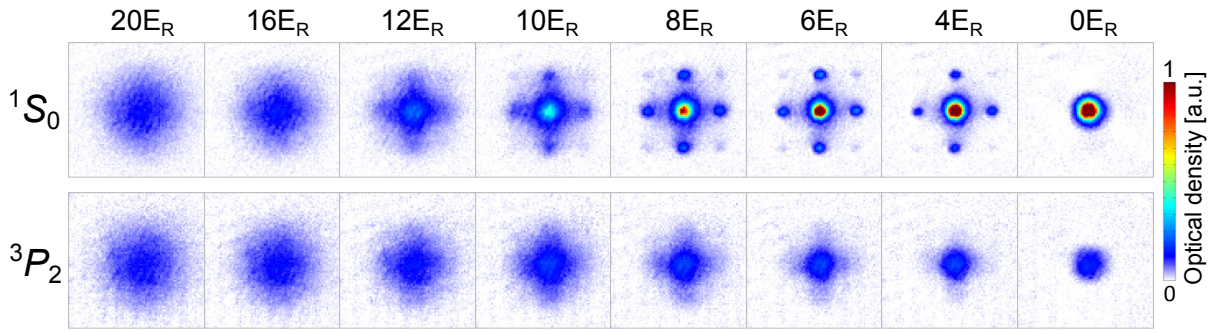

Figure 5.4.2: Absorption images of the atoms. The images are taken with different final lattice depths. The images are averaged over 5 and 20 shots for the $^1S_0$ state and the $^3P_2$ state, respectively.

technique.

We note that, in the case of the $^3P_2$ state, the formation of the interference pattern is still observed, which suggests the the growth of the phase coherence in the metastable state. Because of the strong inelastic collision, it is difficult to create the BEC in the metastable state and load it into the optical lattice. On the other hand, in our method with the slow ramp-down of the lattice, we can load the metastable atoms into the shallow optical lattice with suppressing the inelastic collision between atoms.

Effect of the momentum kick in the repumping process

We estimate the effect of the momentum kick in the repumping process by the deconvolution analysis of the atom distribution. Because the repumping laser is irradiated along the imaging axis, the effect of the recoil due to the photon absorption of the repumping laser is not observed. On the other hand, the expansion of the distribution of the atoms due to the recoil of the photon emission is observed because the direction of the photon emission is random and isotropic. After repumping process, the repumped $^1S_0$ state atoms expand in the accordance with the sum of the original momentum and the recoil momentum obtained by the photon emission.

We estimate the width of the expansion of the atom cloud with calculating the average number of the emitted photons N_{ph} through the repumping process (Table 5.4.1) with the assumption that the repumping process is instantaneously finished. In the numerical calculation, we obtain the momentum distribution due to the recoil in the repumping process, which is well approximated by the gaussian function with a half width at half maximum of 1.2 $\hbar k_L$. Here, $k_L = 2\pi/\lambda_L$ is the wave number of the lattice beam and $\hbar k_L$ represents the recoil momentum of the lattice beam.

After turning off all the trap, the $^3P_2$ atoms expands in 5 ms. Then the atoms get the recoil momenta through the repumping process and expand in 1 ms. In the numerical calculation, all atoms are repumped into the $^1S_0$ state within 10 μs, while the actual repumping time is much larger than the estimated value. We reconstruct the original atom distribution by deconvoluting the recoil momentum distribution from the atom distribution obtained from the TOF image, and estimate original visibility and width, which are shown in the yellow triangles in the Fig. 5.4.3 (b) and (c). This shows that

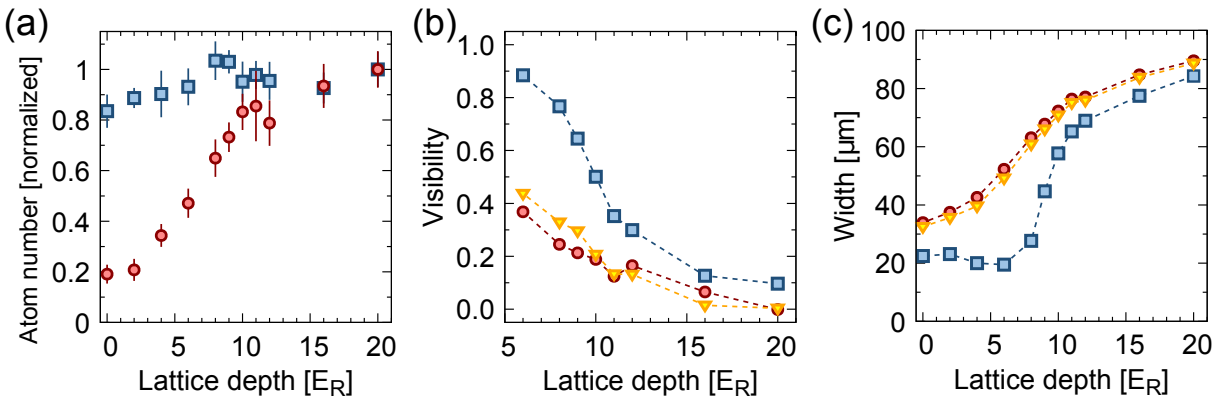

Figure 5.4.3: (a) Temporal change of the atom number during the ramp-down sequence, which is normalized by the initial atom number at the lattice depth of $V_0 = 20\ E_R$. (b) Visibility of the interference peak of the images and (c) width of the density distribution. The width is the full width half maximum obtained by the Gaussian fitting. In these plots, the blue square and the red circle correspond to the data for the $^1S_0$ state and the $^3P_2$ state, respectively. The yellow triangle indicates the data for the $^3P_2$ state after eliminating the effect of the momentum kick.

the effect on the TOF image is limited and does not change the whole behavior of these values qualitatively.

5.5 Summary and Outlook

In conclusion, we have realized the dissipative Bose-Hubbard system with the metastable $^3P_2$ state of ^{174}Yb by first creating a Mott insulating state in the ground state and the subsequent coherent transfer of the atoms into the $^3P_2$ state, evading the large inelastic loss process in the state preparation. We fully characterize the system by measuring the scattering length between two $^3P_2$ atoms by developing the double-excitation method. In the 3D optical lattice, we investigate the atom loss behavior with the unit-filling Mott insulator as the initial state and find that the atom loss is suppressed by the strong correlation between atoms. Also, as we decrease the potential depth of the lattice, we observe the growth of the phase coherence and find that the formation of a sizable phase coherence is suppressed by the dissipation.

It is expected that similar behaviors will be observed with the $^3P_0$ state of Yb [94, 93] and other two-electron atomic species [89, 88, 92]. The strong suppression of the inelastic collision between atoms in the metastable state allows us to investigate the two-component many-body physics [30] and the manipulation of the $^3P_2$ atoms exploiting the magnetic dipole moment [47], avoiding the atom loss in the practical time scale of the experiment.

Another interesting prospect with this system is the control of the on-site interaction. It is expected that the anisotropic interactions between the $^3P_2$ atoms leads to anisotropy-induced Feshbach resonances [155]. In the case of the Yb, the anisotropy-induced Feshbach resonances between the $^1S_0 - {}^3P_2$ was observed [61], which makes us expect the existence of the resonances between the $^3P_2$ atoms. Our new spectroscopic method for measuring

Table 5.4.1: Information of the repump transitions [132]. λ is the wavelength of the transition, $\Gamma^{(s)}$ is the decay rate and N_{ph} is the average number of the photon emission though the repumping process. The numerical simulation is performed based on these parameters.

	$^3S_1 \to {}^3P_0$	$^3S_1 \to {}^3P_1$	$^3S_1 \to {}^3P_2$
λ [nm]	649	680	770
$\Gamma^{(s)}$ [Hz]	9.6 $\times 10^6$	2.7 $\times 10^7$	3.7 $\times 10^7$
Branching ratio	0.13	0.37	0.50
N_{ph}	1.4	1.0	0.36

the on-site interaction enables us to search Feshbach resonances between the $^3P_2$ atoms, while there has been no experimental study of Feshbach resonance because of the absence of the measuring scheme for the dissipative metastable states so far. If we can control the on-site interaction with the Feshbach resonance and change the ratio $\hbar\Gamma_{ee}/U_{ee}$, we can systematically investigate the dissipative Bose-Hubbard in a wide range of the parameters. Unlike the previous researches with molecules [74, 76] or photo-association (Chapter 4), the Feshbach resonance allows one to create attractive on-site interaction, which possibly provide a novel many-body state with the competence between the attractive on-site interaction and the dissipation-induced "repulsive" interaction, for example.

Chapter 6

Conclusion & Outlook

In this thesis, quantum many-body dynamics of a Bose-Hubbard system with artificial and intrinsic dissipation was studied. We briefly review the achievement of the work in this thesis.

- *Observation of the Mott insulator to superfluid crossover of a driven-dissipative Bose-Hubbard system (Chapter 4).*

  We succeeded in the realization of an engineered dissipative Bose-Hubbard system by introducing a controllable-strength two-body inelastic collision with the use of a PA laser. By exploiting the highly controllable nature of the dissipation, we investigated the effect of the dissipation on the quantum phase transition from the Mott insulator state to the superfluid state in the lattice ramp-down dynamics. We observed that the melting of the Mott state is delayed and the growth of phase coherence is suppressed for the strong on-site dissipation. Thanks to the dramatic change in the onset of the Mott-insulator melting, as shown by the increase in zJ/U, we accessed the interesting problem of quenching the dissipation across the crossover from the Mott insulator to the superfluid, where turning off the dissipation corresponds to a sudden parameter change in the Bose-Hubbard system [147]. The experimental results were compared with theoretical analysis and numerical calculation, which qualitatively capture the novel behavior presented in the experiments.

- *Dissipative Bose-Hubbard system with intrinsic two-body atom loss (Chapter 5).*

  We realized a dissipative Bose-Hubbard system with the metastable $^3P_2$ state of ^{174}Yb by first creating a Mott insulating state in the ground state and the subsequent coherent transfer of atoms into the $^3P_2$ state, avoiding large inelastic loss in the state preparation. We fully characterized the system by measuring the scattering length between two $^3P_2$ atoms by developing the double-excitation method. In a 3D optical lattice, we investigated the atom loss behavior with the unit-filling Mott insulator as the initial state and found that the atom loss is suppressed by the strong correlation between atoms. Also, as we decreased the potential depth of the lattice, we observed the growth of the phase coherence and found that the formation of a sizable phase coherence is suppressed by the dissipation.

Outlook

Below, we present possible directions for future experiments with the dissipative Bose-Hubbard system.

Localized dissipation In our experiments, the dissipation is applied homogeneously to the whole system. On the other hand, the effect of localized dissipation on the quantum many-body state has been theoretically investigated. For example, the dynamics of the extended Bose-Hubbard system induced by localized dissipation is analyzed in Ref. [72]. In Ref. [156], different dissipative dynamics in the strongly and weakly correlated superfluid regimes is found. The local addressing technique of a quantum gas microscope enables one to apply the localized dissipation and explore these physics.

Non-Hermitian Bose-Hubbard system One intriguing direction is the investigation of non-Hermitian quantum many-body systems. In our setup, a non-Hermitian Bose-Hubbard system could be realized by post-selecting the dynamics with a quantum gas microscope. In Ref. [28], simulation of the non-Hermitian dynamics and the experimental implementation are proposed with ultracold atoms and a quantum gas microscope and the feasibility of the proposal with inelastic two-body loss is discussed. The realization of the non-Hermitian system leads to the investigation of $\mathcal{PT}$ symmetric systems.

Dissipative Fermi-Hubbard system In Ref. [86], dynamics in a one-dimensional dissipative Fermi-Hubbard system with two- and six-component ^{173}Yb is investigated, and in the experiment, a highly entangled Dicke state is observed. In this setup, the photo-association scheme presented in our thesis could be employed to tune the dissipation strength and study loss dynamics across the phase diagram from the Mott insulator to the quantum Zeno regime, while the inelastic two-body collision between the $^3P_0$ state atoms is used in this experiment.

Anisotropy-induced Feshbach resonance Related to the experiment with the $^3P_2$ state, one interesting prospect is the control of on-site interaction. It is expected that the anisotropic interactions between the $^3P_2$ atoms leads to anisotropy-induced Feshbach resonances, as in the case of Er [157] and Dy [155, 158]. In the case of Yb, the anisotropy-induced Feshbach resonances between $^1S_0-^3P_2$ were observed [61], which lead us to expect the existence of resonances between the $^3P_2$ atoms. Our new spectroscopic method for measuring the on-site interaction enables us to search for Feshbach resonances between the $^3P_2$ atoms, while there has been no experimental study of Feshbach resonance because of the absence of a measuring scheme for dissipative metastable states. If we can control the on-site interaction with the Feshbach resonance and change the ratio $\hbar\Gamma_{ee}/U_{ee}$, we can systematically investigate the dissipative Bose-Hubbard system over a wide range of parameters. Unlike previous studies with molecules [74, 76] or photo-association (Chapter 4), the Feshbach resonance allows one to create attractive on-site interaction and may provide a novel many-body state with competence between the attractive on-site interaction and the dissipation-induced "repulsive" interaction, for example. Also, quantum chaos could be observed in the systematic search for Feshbach resonances, as is observed in the case of Er [159].

Development of more sophisticated tools for numerical calculation In addition to the experimental investigation, we mention the possibility of numerical simulation in the future. In our investigation, numerical analysis under the Gutswiller approximation is presented, which qualitatively agrees with the experimental results. For further investigation, it would be desirable to verify the experimental results with more sophisticated tools such as truncated Winger approximations [160], and the quantum trajectories method [5]. Our experimental results would be useful as a benchmark for developing tools for numerical calculation.

Journal Articles

Below is the list of journal articles to which I contributed during this course.

- *Topological Thouless pumping of ultracold fermions.*
  S. Nakajima, T. Tomita, S. Taie, T. Ichinose, H. Ozawa, L. Wang, M. Troyer, and Y. Takahashi
  Nature Physics **12**, 296 (2016)

- *Observation of the Mott insulator to superfluid crossover of a driven-dissipative Bose-Hubbard system.*
  T. Tomita, S. Nakajima, I. Danshita, Y. Takasu, and Y. Takahashi
  Science Advances **3**, e1701513 (2017)

- *Dissipative Bose-Hubbard system with intrinsic two-body loss.*
  T. Tomita, S. Nakajima, Y. Takasu, and Y. Takahashi
  arXiv:1809.09989 (2018)

Appendix A

Derivation of the dissipative Bose-Hubbard model

In this appendix, we present a detailed derivation of the dissipative Bose-Hubbard model with a two-body loss term from the coupled atom-molecule mixture model with a one-body molecular loss term. The derivation is based on a kind of perturbative approach developed in Ref. [143].

A.1 Model

We start with the Markovian master equation for the coupled atom-molecule mixture model with a one-body molecular loss term,

$$\hbar \frac{d}{dt}\hat{\rho} = -i\left[\hat{H}, \hat{\rho}\right] + L_{\mathrm{M}}(\hat{\rho}). \tag{A.1.1}$$

The Hamiltonian is given by

$$\hat{H} = \hat{H}_0 + \hat{H}_{\mathrm{am}} + \hat{H}_{\mathrm{hop}}, \tag{A.1.2}$$

where

$$\hat{H}_0 = \sum_j \left(D\hat{n}_{\mathrm{M},j} + \frac{U}{2}\hat{n}_{\mathrm{A},j}(\hat{n}_{\mathrm{A},j} - 1) + W\hat{n}_{\mathrm{A},j}\hat{n}_{\mathrm{M},j} \right), \tag{A.1.3}$$

$$\hat{H}_{\mathrm{am}} = \sum_j g\left(\hat{m}_j^\dagger \hat{a}_j \hat{a}_j + \mathrm{h.c.} \right), \tag{A.1.4}$$

$$\hat{H}_{\mathrm{hop}} = -\sum_{\langle j,k \rangle} J\left(\hat{a}_j^\dagger \hat{a}_k + \mathrm{h.c.} \right). \tag{A.1.5}$$

The quantum phases of this atom-molecular Hamiltonian have been theoretically studied in Ref. [141]. We anticipate that the molecule consists of a $^1S_0$ atom and a $^3P_1$ atom as in the experiment such that its linewidth is on the order of 1 MHz due to the short lifetime of the latter state of atom. Hence, we have to include the one-body loss term of molecules in the master equation,

$$L_{\mathrm{M}}(\hat{\rho}) = \frac{\hbar\Gamma_{\mathrm{M}}}{2} \sum_j \left(-\hat{n}_{\mathrm{M},j}\hat{\rho} - \hat{\rho}\hat{n}_{\mathrm{M},j} + 2\hat{m}_j \hat{\rho} \hat{m}_j^\dagger \right). \tag{A.1.6}$$

Equation (A.1.1) describes the dynamics of ultracold bosonic atoms in an optical lattice coupled with a molecular state via PA laser. $\hat{a}_j$ and $\hat{m}_j$ annihilate an atom and a molecule on site j while $\hat{n}_{\mathrm{A},j} = \hat{a}_j^\dagger \hat{a}_j$ and $\hat{n}_{\mathrm{M},j} = \hat{m}_j^\dagger \hat{m}_j$ are the density operators of atoms and molecules. Γ_{M}, D, U, W, g, and J denote the one-body loss of molecules, the detuning of the PA coupling from the molecular state, the on-site interaction between two atoms, the on-site interaction between an atom and a molecule, the atom-molecule coupling, and the tunneling amplitude of atoms. $\langle j,k\rangle$ represents nearest-neighboring pairs of lattice sites. Since $\hbar\Gamma_{\mathrm{M}} \gg \max(|D|,|g|,|J|)$, a molecule created on a lattice site via the PA laser decays much earlier than the creation of another molecule on the same site. In this sense, we can safely assume the hardcore constraint on the molecules, which forbids more than one molecules to occupy a single site. We aim to show that when $\hbar\Gamma_{\mathrm{M}} \gg \max(|D|,|U|,|W|,|g|,|J|)$, the molecular degrees of freedom can be properly projected out by means of a perturbation theory [143] such that the system is well approximated by the following effective master equation,

$$\hbar\frac{d}{dt}\hat{\rho}_{\mathrm{eff}} = -i\left[\hat{H}_{\mathrm{eff}}, \hat{\rho}_{\mathrm{eff}}\right] + L_2(\hat{\rho}_{\mathrm{eff}}), \tag{A.1.7}$$

where

$$\hat{H}_{\mathrm{eff}} = \sum_j \frac{U}{2}\hat{n}_{\mathrm{A},j}(\hat{n}_{\mathrm{A},j}-1) - \sum_{\langle j,k\rangle} J\left(\hat{a}_j^\dagger \hat{a}_k + \mathrm{h.c.}\right), \tag{A.1.8}$$

$$L_2(\hat{\rho}_{\mathrm{eff}}) = \frac{\hbar\Gamma_{\mathrm{PA}}}{4}\sum_j \left(-\hat{a}_j^\dagger\hat{a}_j^\dagger\hat{a}_j\hat{a}_j\hat{\rho}_{\mathrm{eff}} - \hat{\rho}_{\mathrm{eff}}\hat{a}_j^\dagger\hat{a}_j^\dagger\hat{a}_j\hat{a}_j + 2\hat{a}_j\hat{a}_j\hat{\rho}_{\mathrm{eff}}\hat{a}_j^\dagger\hat{a}_j^\dagger\right), \tag{A.1.9}$$

and

$$\Gamma_{\mathrm{PA}} = \frac{8g^2}{\hbar^2\Gamma_{\mathrm{M}}}. \tag{A.1.10}$$

In order to express the density matrix of the system more explicitly, we define the local Fock state on site j,

$$|n_a, n_m\rangle_j = \frac{1}{\sqrt{n_a!\, n_m!}}(\hat{a}_j^\dagger)^{n_a}(\hat{m}_j^\dagger)^{n_m}|vac\rangle_j \tag{A.1.11}$$

We set the maximum number of atoms per site to be $d-1$. Hence, the dimension of the local Hilbert space is $2d$. While the maximum number of bosonic atoms per site is in principle the total number of atoms, at a finite filling factor the occupation probability of large-n_a states decays exponentially. This means that setting the cutoff of the local Hilbert space at $n_a = d-1$ does not affect results of numerical calculations in practice as long as $U > 0$ and d is sufficiently large [161].

For convenience, we introduce a simpler notation for the local state,

$$|l\rangle_j = \begin{cases} |n_a = l-1, n_m = 0\rangle_j, & \text{when } 1 \le l \le d, \\ |n_a = l-1-d, n_m = 1\rangle_j, & \text{when } d+1 \le l \le 2d. \end{cases} \tag{A.1.12}$$

Using the local states defined above, we express a general form of the density matrix as

$$\hat{\rho} = \sum_{l_1,l_2,\ldots}\sum_{m_1,m_2,\ldots}\rho_{l_1,l_2,\ldots}^{m_1,m_2,\ldots}\prod_j |l_j\rangle\langle m_j|_j. \tag{A.1.13}$$

Regarding the density matrix $\hat{\rho}$, which is a $(2d)^M \times (2d)^M$ matrix, as a $(2d)^{2M}$-dimensional vector $\boldsymbol{\rho}$, we can rewrite the master equation in the following form,

$$\hbar \frac{d}{dt}\boldsymbol{\rho} = \left(\hat{\mathcal{M}}_0 + \hat{\mathcal{V}}_{\rm am} + \hat{\mathcal{V}}_{\rm hop}\right)\boldsymbol{\rho}, \tag{A.1.14}$$

where the superoperators $\hat{\mathcal{M}}_0$, $\hat{\mathcal{V}}_{\rm am}$, and $\hat{\mathcal{V}}_{\rm hop}$ are $(2d)^{2M}\times(2d)^{2M}$ matrices originated from $\hat{H}_0$ and $L_{\rm M}(\hat{\rho})$, $\hat{H}_{\rm am}$, and $\hat{H}_{\rm hop}$, respectively. Associated with the change of the notation from $\hat{\rho}$ to $\boldsymbol{\rho}$, we also express the local matrix as the following vector,

$$|l_j, m_j)_j = |l_j\rangle\langle m_j|_j. \tag{A.1.15}$$

This vector satisfies the orthonormality condition,

$$(l'_j, m'_j|l_j, m_j) = \delta_{l'_j,l_j}\delta_{m'_j,m_j}. \tag{A.1.16}$$

A.2 Local projection

In order to derive the effective master equation (A.1.7), we need to express some of the superoperators explicitly and introduce the projection superoperator. The non-perturbative superoperator $\hat{\mathcal{M}}_0$ can be expressed as a sum of commuting local superoperators $\hat{\mathcal{M}}^{\rm loc}_{0,j}$,

$$\hat{\mathcal{M}}_0 = \sum_j \hat{\mathcal{M}}^{\rm loc}_{0,j}, \tag{A.2.1}$$

where

$$\hat{\mathcal{M}}^{\rm loc}_0 = \sum_{l=1}^{2d}\sum_{m=1}^{2d} |l,m)(l,m|\, i\left(\left(E^{(0)}_l\right)^* - E^{(0)}_m\right) + \sum_{l=1}^{d}\sum_{m=1}^{d} |l,m)(d+l,d+m|\hbar\Gamma_{\rm M}, \tag{A.2.2}$$

and

$$E^{(0)}_l = \begin{cases} \frac{U}{2}(l-1)(l-2), & \text{when } 1 \le l \le d, \\ D + \frac{U}{2}(l-d-1)(l-d-2) + W(l-d-1) - i\frac{\hbar\Gamma_{\rm M}}{2}, & \text{when } d+1 \le l \le 2d. \end{cases} \tag{A.2.3}$$

The perturbative superoperator $\hat{\mathcal{V}}_{\rm am}$ originated from the atom-molecule coupling $\hat{H}_{\rm am}$ can be also expressed as a sum of commuting local superoperators,

$$\hat{\mathcal{V}}_{\rm am} = \sum_j \hat{\mathcal{V}}^{\rm loc}_{{\rm am},j} \tag{A.2.4}$$

where

$$\begin{aligned} \hat{\mathcal{V}}^{\rm loc}_{\rm am} \;=\; & \sum_{l=1}^{2d}\sum_{m=1}^{d} \left(|l,m)(l,d+m-2| + |l,d+m-2)(l,m|\right)\tilde{g}_m \\ & - \sum_{l=1}^{d}\sum_{m=1}^{2d} \left(|l,m)(d+l-2,m| + |d+l-2,m)(l,m|\right)\tilde{g}_l \end{aligned} \tag{A.2.5}$$

and

$$\tilde{g}_l = g\sqrt{(l-1)(l-2)}. \tag{A.2.6}$$

We omitted the site index j of $\hat{\mathcal{M}}^{\rm loc}_{0,j}$ and $\hat{\mathcal{V}}^{\rm loc}_{{\rm am},j}$ in Eqs. (A.2.2) and (A.2.5) because they do not depend on j.

We do not write an explicit expression of the superoperator $\hat{\mathcal{V}}_{\rm hop}$ because it is unnecessary for our purpose. Nevertheless, it is worth noting that $\hat{\mathcal{V}}_{\rm hop}$ changes neither the number of atoms nor the number of molecules. This means that this superoperator does not have matrix elements connecting the effective Hilbert space with the truncated one.

In order to construct the projection superoperator, we need to solve the following eigenvalue problem,

$$\hat{\mathcal{M}}^{\rm loc}_0|v_\alpha) = \lambda_\alpha|v_\alpha), \tag{A.2.7}$$
$$(w_\alpha|\hat{\mathcal{M}}^{\rm loc}_0 = (w_\alpha|\lambda_\alpha. \tag{A.2.8}$$

Notice that the left eigenvector $(w_\alpha|$ in general is not equal to the conjugate of the right eigenvector $|v_\alpha)$ because $\hat{\mathcal{M}}^{\rm loc}_0$ is not Hermitian. The eigenvectors satisfy the following orthonormality condition,

$$(w_{\alpha'}|v_\alpha) = \delta_{\alpha,\alpha'}. \tag{A.2.9}$$

When we derive the effective model, we utilize the fact that d^2 eigenvalues have the property $|\lambda_\alpha| = O(\max(|D|,|U|,|W|))$ and the other eigenvalues have $|\lambda_\alpha| = O(\hbar\Gamma_{\rm M})$. The local subspaces that include states with the former and latter properties are denoted by $\mathcal{D}^{\rm loc}_{\rm eff}$ and $\mathcal{D}^{\rm loc}_{\rm trc}$, respectively.

We define the local projection superoperators as

$$\hat{\mathcal{P}}^{\rm loc}_\alpha = |v_\alpha)(w_\alpha|. \tag{A.2.10}$$

This superoperator projects a state or a superoperator on state α. From these projectors, we construct the projection superoperator on the effective Hilbert space,

$$\begin{aligned}\hat{\mathcal{P}}^{\rm loc}_{\rm eff} &= \sum_{\alpha\in\mathcal{D}^{\rm loc}_{\rm eff}} \hat{\mathcal{P}}^{\rm loc}_\alpha \\ &= \sum_{l=1}^{d}\sum_{m=1}^{d} \left(|l,m)(l,m| + |l,m)(d+l,d+m|\right). \end{aligned}\tag{A.2.11}$$

Notice that from the first line to the second line of Eq. (A.2.11), we neglected the terms on the order of $\max(|D|,|U|,|W|)/(\hbar\Gamma_{\rm M})$ on the basis of the assumption that $\hbar\Gamma_{\rm M} \gg \max(|D|,|U|,|W|)$.

A.3 Second-order perturbation

From the local projection operator of Eq. (A.2.11), we construct the projection operators for the entire system as

$$\hat{\mathcal{P}}_{\rm eff} = \prod_{j=1}^{M} \hat{\mathcal{P}}^{\rm loc}_{{\rm eff},j}, \tag{A.3.1}$$

$$\hat{\mathcal{P}}_{\rm trc} = \hat{\mathcal{I}} - \hat{\mathcal{P}}_{\rm eff}, \tag{A.3.2}$$

where $\hat{\mathcal{I}}$ is the global identity matrix. Multiplying $\hat{\mathcal{P}}_{\rm eff}$ on Eq. (A.1.14) from the left and using the facts that $\hat{\mathcal{P}}_{\rm eff}\hat{\mathcal{V}}_{\rm am}\hat{\mathcal{P}}_{\rm eff}=0$ and $\hat{\mathcal{P}}_{\rm eff}\hat{\mathcal{V}}_{\rm hop}\hat{\mathcal{P}}_{\rm trc}=0$, we obtain

$$\hbar\frac{d}{dt}\boldsymbol{\rho}_{\rm eff}=\hat{\mathcal{P}}_{\rm eff}\left(\hat{\mathcal{M}}_0+\hat{\mathcal{V}}_{\rm hop}\right)\hat{\mathcal{P}}_{\rm eff}\boldsymbol{\rho}_{\rm eff}+\hat{\mathcal{P}}_{\rm eff}\hat{\mathcal{V}}_{\rm am}\hat{\mathcal{P}}_{\rm trc}\boldsymbol{\rho}_{\rm trc}, \tag{A.3.3}$$

where

$$\boldsymbol{\rho}_{\rm eff} = \hat{\mathcal{P}}_{\rm eff}\boldsymbol{\rho}, \tag{A.3.4}$$
$$\boldsymbol{\rho}_{\rm trc} = \hat{\mathcal{P}}_{\rm trc}\boldsymbol{\rho}. \tag{A.3.5}$$

In Eq. (A.3.3), it is obvious that the first and second terms in the right hand side already agree with the term $-i\left[\hat{H}_{\rm eff},\hat{\rho}_{\rm eff}\right]$ in Eq. (A.1.7).

We will next derive $\hat{L}_2(\hat{\rho}_{\rm eff})$ in Eq. (A.1.7) from the last term in the right hand side of Eq. (A.3.3). The components in $\hat{\mathcal{P}}_{\rm trc}$ that can give finite contributions to $\hat{\mathcal{P}}_{\rm eff}\hat{\mathcal{V}}_{\rm am}\hat{\mathcal{P}}_{\rm trc}$ are the ones written as

$$\hat{\mathcal{P}}_\beta=\sum_k\hat{\mathcal{P}}_\beta^{(k)}, \tag{A.3.6}$$

where

$$\hat{\mathcal{P}}_\beta^{(k)}=\hat{\mathcal{P}}_{\beta,k}^{\rm loc}\prod_{j\neq k}\hat{\mathcal{P}}_{{\rm eff},j}^{\rm loc}, \tag{A.3.7}$$

and $\beta\in\mathcal{D}_{\rm trc}^{\rm loc}$. Hence, Eq. (A.3.3) can be rewritten as

$$\hbar\frac{d}{dt}\boldsymbol{\rho}_{\rm eff}=\hat{\mathcal{P}}_{\rm eff}\left(\hat{\mathcal{M}}_0+\hat{\mathcal{V}}_{\rm hop}\right)\hat{\mathcal{P}}_{\rm eff}\boldsymbol{\rho}_{\rm eff}+\hat{\mathcal{P}}_{\rm eff}\hat{\mathcal{V}}_{\rm am}\sum_\beta\hat{\mathcal{P}}_\beta\boldsymbol{\rho}_\beta. \tag{A.3.8}$$

In order for Eq. (A.3.8) to be closed within the effective Hilbert space, we need to express $\boldsymbol{\rho}_\beta$ in terms of $\boldsymbol{\rho}_{\rm eff}$. For this purpose, we look into the equation for $\boldsymbol{\rho}_\beta$ given by

$$\hbar\frac{d}{dt}\boldsymbol{\rho}_\beta=\left(\hat{\mathcal{R}}+\lambda_\beta\right)\boldsymbol{\rho}_\beta+\hat{P}_\beta\hat{\mathcal{V}}_{\rm am}\hat{P}_{\rm eff}\boldsymbol{\rho}_{\rm eff}+\hat{P}_\beta\hat{\mathcal{V}}\hat{P}_{\rm trc}\boldsymbol{\rho}_{\rm trc}, \tag{A.3.9}$$

where

$$\hat{\mathcal{R}} = \sum_k\hat{\mathcal{P}'}_{\rm eff}^{(k)}\hat{\mathcal{M}'}_0^{(k)}, \tag{A.3.10}$$
$$\hat{\mathcal{M}'}_0^{(k)} = \sum_{j\neq k}\hat{\mathcal{M}}_{0,j}^{\rm loc}, \tag{A.3.11}$$
$$\hat{\mathcal{P}'}_{\rm eff}^{(k)} = \hat{\mathcal{I}}_k^{\rm loc}\prod_{j\neq k}\hat{\mathcal{P}}_{{\rm eff},j}^{\rm loc}. \tag{A.3.12}$$

We neglect the last term in the right hand side of Eq. (A.3.9) because it gives higher-order contributions with respect to $\hat{\mathcal{V}}$. Making a variable transformation,

$$\boldsymbol{\rho}_\beta(t) = e^{\hat{\mathcal{R}}t/\hbar}\tilde{\boldsymbol{\rho}}_\beta(t), \tag{A.3.13}$$
$$\boldsymbol{\rho}_{\rm eff}(t) = e^{\hat{\mathcal{R}}t/\hbar}\tilde{\boldsymbol{\rho}}_{\rm eff}(t), \tag{A.3.14}$$

Eq. (A.3.9) is simplified a little,

$$\hbar\frac{d}{dt}\tilde{\boldsymbol{\rho}}_\beta = \lambda_\beta\tilde{\boldsymbol{\rho}}_\beta + \hat{P}_\beta\hat{\mathcal{V}}_{\rm am}\hat{P}_{\rm eff}\tilde{\boldsymbol{\rho}}_{\rm eff}. \tag{A.3.15}$$

Formally solving Eq. (A.3.15), we obtain

$$\tilde{\boldsymbol{\rho}}_\beta(t) = \frac{1}{\hbar}e^{\lambda_\beta t/\hbar}\int_0^t d\tau e^{-\lambda_\beta\tau/\hbar}\hat{P}_\beta\hat{\mathcal{V}}_{\rm am}\hat{P}_{\rm eff}\tilde{\boldsymbol{\rho}}_{\rm eff}(\tau). \tag{A.3.16}$$

Performing a partial integral, this solution becomes

$$\tilde{\boldsymbol{\rho}}_\beta(t) = -\frac{1}{\lambda_\beta}\hat{\mathcal{P}}_\beta\hat{\mathcal{V}}\hat{\mathcal{P}}_{\rm eff}\left(\tilde{\boldsymbol{\rho}}_{\rm eff}(t) - e^{\lambda_\beta t/\hbar}\tilde{\boldsymbol{\rho}}_{\rm eff}(0)\right) + \frac{e^{\lambda_\beta t/\hbar}}{\lambda_\beta}\int_0^t d\tau e^{-\lambda_\beta\tau/\hbar}\hat{\mathcal{P}}_\beta\hat{\mathcal{V}}\hat{\mathcal{P}}_{\rm eff}\frac{d}{d\tau}\tilde{\boldsymbol{\rho}}_{\rm eff}(\tau). \tag{A.3.17}$$

The remaining integral can be neglected because it is of higher order in $\max(|D|,|U|,|W|,|g|,|J|)/(\hbar\Gamma_{\rm M})$. The second term in Eq. (A.3.17), which includes $e^{\lambda_\beta t/\hbar}\tilde{\boldsymbol{\rho}}_{\rm eff}(0)$, decays very quickly on the order of $1/\Gamma_{\rm M}$ so that it can be also neglected as long as we are interested in much longer time scale than $1/\Gamma_{\rm M}$. Moreover, $\lambda_\beta = -\hbar\Gamma_{\rm M}/2$ in its leading order. Hence, $\boldsymbol{\rho}_\beta$ is well approximated as

$$\boldsymbol{\rho}_\beta(t) = \frac{2}{\hbar\Gamma_{\rm M}}\hat{\mathcal{P}}_\beta\hat{\mathcal{V}}\hat{\mathcal{P}}_{\rm eff}\boldsymbol{\rho}_{\rm eff}(t). \tag{A.3.18}$$

Substituting Eq. (A.3.18) into Eq. (A.3.8), we obtain

$$\hbar\frac{d}{dt}\boldsymbol{\rho}_{\rm eff} = \hat{\mathcal{P}}_{\rm eff}(\hat{\mathcal{M}}_0 + \hat{\mathcal{V}}_{\rm hop})\hat{\mathcal{P}}_{\rm eff}\boldsymbol{\rho}_{\rm eff} + \frac{2}{\hbar\Gamma_{\rm M}}\sum_{\beta\in\mathcal{D}_{\rm trc}^{\rm loc}}\hat{\mathcal{P}}_{\rm eff}\hat{\mathcal{V}}_{\rm am}\hat{\mathcal{P}}_\beta\hat{\mathcal{V}}_{\rm am}\hat{\mathcal{P}}_{\rm eff}\boldsymbol{\rho}_{\rm eff}, \tag{A.3.19}$$

where

$$\sum_\beta\hat{\mathcal{P}}_{\rm eff}\hat{\mathcal{V}}_{\rm am}\hat{\mathcal{P}}_\beta\hat{\mathcal{V}}_{\rm am}\hat{\mathcal{P}}_{\rm eff} = \sum_k\sum_\beta\hat{\mathcal{P}}^{\rm loc}_{{\rm eff},k}\hat{\mathcal{V}}^{\rm loc}_{{\rm am},k}\hat{\mathcal{P}}^{\rm loc}_{\beta,k}\hat{\mathcal{V}}^{\rm loc}_{{\rm am},k}\hat{\mathcal{P}}^{\rm loc}_{{\rm eff},k} \tag{A.3.20}$$

and

$$\begin{aligned}
&\hat{\mathcal{P}}^{\rm loc}_{\rm eff}\hat{\mathcal{V}}^{\rm loc}_{\rm am}\hat{\mathcal{P}}^{\rm loc}_\beta\hat{\mathcal{V}}^{\rm loc}_{\rm am}\hat{\mathcal{P}}^{\rm loc}_{\rm eff}\\
&= \sum_{l=1}^{d}\sum_{m=1}^{d}\Big(|l,m)(l,m|(\tilde{g}_m^2+\tilde{g}_l^2) - |l,m)(l+2,m+2|2\tilde{g}_{l+2}\tilde{g}_{m+2}\\
&\quad +|l,m)(d+l,d+m|(\tilde{g}_m^2+\tilde{g}_l^2) - |l,m)(d+l+2,d+m+2|2\tilde{g}_{l+2}\tilde{g}_{m+2}\Big).
\end{aligned} \tag{A.3.21}$$

Rewriting Eq. (A.1.7) with use of superoperators and the vector form of the density matrix, and setting $\Gamma_{\rm PA} = 8g^2/(\hbar^2\Gamma_{\rm M})$, we recognize that the derived effective master equation, which is Eq. (A.3.19), is equivalent to that for the dissipative Bose-Hubbard model with the two-body loss term. Thus, we have successfully derived the dissipative Bose-Hubbard model from the coupled atom-molecule mixture model with the one-body molecular loss term.

Appendix B

Theoretical analysis of loss dynamics from the Mott insulating state with double filling

In this appendix, we analyze the dynamics of the Mott insulator with two bosonic atoms per site in an optical lattice subjected to a sudden increase of the atom-molecule coupling g from zero.

As an initial condition, we assume that the system is deep in a Mott insulating state of atoms with double filling and that the atom-molecule coupling g is zero. In such a situation we can safely neglect the hopping term of atoms as long as we are interested in the atom-loss dynamics and its timescale $1/\Gamma_{\mathrm{PA}}$ is much shorter than that of the hopping, which is on the order of $\hbar U/J^2$ in the Mott insulator. Thus, the system can be described by the following single-site master equation,

$$\hbar\frac{d}{dt}\hat{\rho}^{\mathrm{loc}} = -i\left[\hat{H}^{\mathrm{loc}}, \hat{\rho}^{\mathrm{loc}}\right] + L_{\mathrm{M}}^{\mathrm{loc}}(\hat{\rho}^{\mathrm{loc}}). \tag{B.0.1}$$

The Hamiltonian is given by

$$\hat{H}^{\mathrm{loc}} = \hat{H}_0^{\mathrm{loc}} + \hat{H}_{\mathrm{am}}^{\mathrm{loc}}, \tag{B.0.2}$$

where

$$\hat{H}_0^{\mathrm{loc}} = \left(D\hat{n}_{\mathrm{M}} + \frac{U}{2}\hat{n}_{\mathrm{A}}(\hat{n}_{\mathrm{A}}-1) + W\hat{n}_{\mathrm{A}}\hat{n}_{\mathrm{M}}\right), \tag{B.0.3}$$

$$\hat{H}_{\mathrm{am}}^{\mathrm{loc}} = g\left(\hat{m}^{\dagger}\hat{a}\hat{a} + \mathrm{h.c.}\right). \tag{B.0.4}$$

The one-body molecular loss term is given by

$$L_{\mathrm{M}}^{\mathrm{loc}}(\hat{\rho}^{\mathrm{loc}}) = \frac{\hbar\Gamma_{\mathrm{M}}}{2}\left(-\hat{n}_{\mathrm{M}}\hat{\rho}^{\mathrm{loc}} - \hat{\rho}^{\mathrm{loc}}\hat{n}_{\mathrm{M}} + 2\hat{m}\hat{\rho}\hat{m}^{\dagger}\right). \tag{B.0.5}$$

Since the initial state is $|n_{\mathrm{A}}=2, n_{\mathrm{M}}=0\rangle$, the Hilbert space necessary for describing the dynamics of Eq. (B.0.1) is spanned by only three states, namely

$$\begin{cases} |n_{\mathrm{A}}=0, n_{\mathrm{M}}=0\rangle \\ |n_{\mathrm{A}}=2, n_{\mathrm{M}}=0\rangle \\ |n_{\mathrm{A}}=0, n_{\mathrm{M}}=1\rangle. \end{cases} \tag{B.0.6}$$

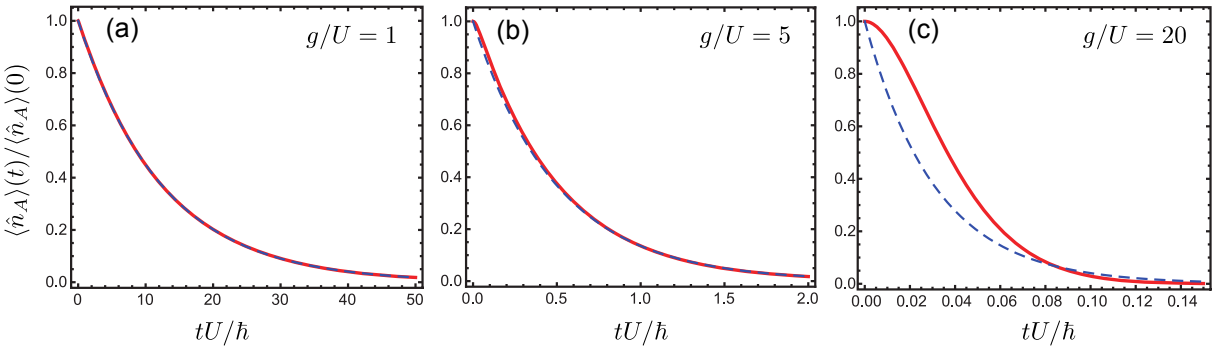

Figure B.0.1: Time evolution of the normalized atom density $\langle \hat{n}_{\rm A} \rangle(t)$ for $\langle \hat{n}_{\rm A} \rangle(0) = 2$. We take $\hbar\Gamma_{\rm M}/U = 100$ and $D/U = 1$. The red solid lines represent the numerical solution of Eq. (B.0.1) while the blue dashed line represent the analytical solution (B.0.11) of the effective model (B.0.7).

When $\hbar\Gamma_{\rm M} \gg |g|$, we can properly eliminate the state $|n_{\rm A} = 0, n_{\rm M} = 1\rangle$ by means of the perturbation theory used in the previous section, to derive the effective master equation,

$$\hbar \frac{d}{dt} \hat{\rho}_{\rm eff}^{\rm loc} = -i \left[\hat{H}_{\rm eff}^{\rm loc}, \hat{\rho}_{\rm eff}^{\rm loc} \right] + L_2^{\rm loc}(\hat{\rho}_{\rm eff}^{\rm loc}), \tag{B.0.7}$$

where

$$\hat{H}_{\rm eff}^{\rm loc} = \frac{U}{2} \hat{n}_{\rm A}(\hat{n}_{\rm A} - 1), \tag{B.0.8}$$

$$L_2^{\rm loc}(\hat{\rho}_{\rm eff}^{\rm loc}) = \frac{\hbar\tilde{\Gamma}_{\rm PA}}{4} \left(-\hat{a}^\dagger \hat{a}^\dagger \hat{a}\hat{a} \hat{\rho}_{\rm eff}^{\rm loc} - \hat{\rho}_{\rm eff}^{\rm loc} \hat{a}^\dagger \hat{a}^\dagger \hat{a}\hat{a} + 2\hat{a}\hat{a} \hat{\rho}_{\rm eff}^{\rm loc} \hat{a}^\dagger \hat{a}^\dagger \right), \tag{B.0.9}$$

and

$$\tilde{\Gamma}_{\rm PA} = \frac{8g^2}{\hbar^2 \Gamma_{\rm M}} \left[1 + 4 \left(\frac{D - U}{\hbar\Gamma_{\rm M}} \right)^2 \right]^{-1}. \tag{B.0.10}$$

In contrast to the case in the previous section, the effective model is valid without the condition that $\hbar\Gamma_{\rm M} \gg \max(|D|, |U|, |W|)$ and we could obtain the analytical expression of $\tilde{\Gamma}_{\rm PA}$, which includes the explicit dependence on U and D. It is obvious that when $\hbar\Gamma_{\rm M} \gg \max(|D|, |U|, |W|)$, $\tilde{\Gamma}_{\rm PA}$ coincides with $\Gamma_{\rm PA}$.

The dynamics of the effective master equation (B.0.7) involves only the two states such that we can easily obtain its analytical solution,

$$\langle \hat{n}_{\rm A} \rangle(t) = 2e^{-\tilde{\Gamma}_{\rm PA} t}. \tag{B.0.11}$$

In order to check the validity of the effective master equation (B.0.7), in Fig. B.0.1 we compare Eq. (B.0.11) with the numerical solution of the original master equation (B.0.1) including the molecular degree of freedom. We see that the analytical and numerical results agree when $\hbar\Gamma_{\rm M} \gg g$.

Appendix C

Gutzwiller mean-field approximation

In this appendix, we explain the Gutzwiller mean-field theory [144, 145, 36] which is used for the numerical calculation shown in Chapter 4. While the Gutzwiller approximation is a simple mean-field theory, it has been extensively used to study various phenomena and properties of Bose gases in optical lattices, including the quantum phase transitions [144, 97, 162], the elementary excitations [163, 164], the superfluid critical momentum [165, 166], and the non-equilibrium dynamics [167, 168, 169]. Recently, it has been applied for solving the master equation of the Bose-Hubbard system with dissipation terms [69, 70, 71, 72]. This approximation is more accurate in higher dimensions, where there are more mean fields to interact with. In the case of the Bose-Hubbard model on a cubic lattice, for instance, the Gutzwiller approximation gives the critical point for the superfluid-Mott insulator quantum phase transition at unit filling as $zJ/U = 0.1716$ while that by the quantum Monte Carlo method is $zJ/U = 0.2045$ [99], where z is the coordination number. Since the experimental system considered in our study is three dimensional, the Gutzwiller approximation can give reliable results at least qualitatively.

Here we explicitly explain the Gutzwiller mean-field theory applied to the atom-molecule mixture model of Eq. A.1.1. One can easily apply the same prescription to the effective Bose-Hubbard model of Eq. A.1.7 in a very similar manner.

In the Gutzwiller mean-field approximation, the many-body density matrix is assumed to be a single product of local density matrices,

$$\hat{\rho} = \prod_j \hat{\rho}_j^{\mathrm{GW}}, \tag{C.0.1}$$

where

$$\hat{\rho}_j^{\mathrm{GW}} = \sum_{l_j=1}^{2d} \sum_{m_j=1}^{2d} \rho_{l_j,m_j}^{(j)} |l_j\rangle\langle m_j|_j. \tag{C.0.2}$$

From the Gutzwiller density matrix, we define the local superfluid order parameter as

$$\psi_j = \langle \hat{a}_j \rangle = \mathrm{Tr}[\hat{\rho}_j^{\mathrm{GW}} \hat{a}_j]. \tag{C.0.3}$$

In the Gutzwiller mean-field approximation, we ignore the second order terms with respect to the fluctuation of $\hat{a}_j$ from its mean value ψ_j. In this way, the Hamiltonian is simplified

as

$$\hat{H} \simeq \sum_j \hat{H}_j^{\mathrm{GW}}, \tag{C.0.4}$$

where

$$\hat{H}_j^{\mathrm{GW}} = \hat{H}_{0,j}^{\mathrm{loc}} + \hat{H}_{\mathrm{am},j}^{\mathrm{loc}} + \hat{H}_{\mathrm{hop},j}^{\mathrm{GW}}, \tag{C.0.5}$$

$$\hat{H}_{\mathrm{hop},j}^{\mathrm{GW}} = -J \sum_{\langle k \rangle_j} \left(\psi_k^* \hat{a}_j + \hat{a}_j^\dagger \psi_k \right). \tag{C.0.6}$$

In Eq. (C.0.6), $\langle k \rangle_j$ means sites nearest-neighboring to j. It is worth noting that $\hat{H}_j^{\mathrm{GW}}$ includes only local operators at site j because one of field operators in the tunneling term is replaced with its mean value. Thanks to this property, the master equation under the Gutzwiller mean-field approximation is closed within local site j,

$$\hbar \frac{d}{dt} \hat{\rho}_j^{\mathrm{GW}} = -i \left[\hat{H}_j^{\mathrm{GW}}, \hat{\rho}_j^{\mathrm{GW}} \right] + L_{\mathrm{M}}^{\mathrm{loc}}(\hat{\rho}_j^{\mathrm{GW}}), \tag{C.0.7}$$

such that we can solve the master equation at a very low numerical cost.

Assuming that the system is homogeneous, we further simplify the master equation, i.e., we drop the dependence on the site index j. This assumption means that we neglect fluctuations other than the zero-momentum one and the effect of the trapping potential. Since the trapping potential is present in the actual experiment, our theoretical analyses within this simplification do not correspond to the experiment at a quantitative level. We emphasize that the main purpose of our theoretical analyses is to provide qualitative explanations for the interesting effects of the engineered dissipation observed in the experiment.

Appendix D

Measurement of the polarizability of the $^3P_2$ state of ^{174}Yb for the 532-nm light

In this appendix, we describe measurement of the polarizability of the $^3P_2$ state of ^{174}Yb for the 532-nm light. Here, we measure the ratio of the polarizability between the $^3P_2$ state and the $^1S_0$ state by spectroscopically determining the band gap in the 3D optical lattice with a 507-nm excitation laser. We can determine the polarizability of the $^3P_2$ state by precisely evaluating the lattice depth for the $^3P_2$ state from the excitation frequency and the known lattice depth for the $^1S_0$.

D.1 Band gap in the deep optical lattice

When the lattice beam forms the potential $V_g = s_g E_R$ for the $^1S_0$ state, it creates the potential $V_e = (\alpha_e/\alpha_g)s_g E_R$ for the $^3P_2$ state, where α_e and α_g represent the polarizability of the $^3P_2$ state and the $^1S_0$ state, respectively. Therefore, we can determine the ratio α_e/α_g by measuring the lattice depth s_e and comparing with the known lattice depth s_g. Here, we define the polarizability $\alpha_{g(e)}$ as follows:

$$V_{g(e)}\ [\mathrm{Hz}] = -\frac{1}{4}\alpha_{g(e)}\ [\mathrm{Hz/(W/cm^2)}]I\ [\mathrm{W/cm^2}], \tag{D.1.1}$$

where I is the intensity of the laser.

To measure the lattice depth s_e, we spectroscopically determine the band gap, which is a function of the lattice depth. In the excitation from the $^1S_0$ state to the $^3P_2$ state, we can observe the blue-sideband in addition to the carrier transition. In the blue-sideband transition, the excited state is the 1st vibrational level of the optical lattice for the $^3P_2$ state, which means that we can measure the band gap of the lattice for the $^3P_2$ state by measuring the difference between the excitation frequency to the carrier and the blue-sideband transitions. When the lattice depth is deep enough, the band gap can be described as $\Delta = \hbar\omega = 2\sqrt{s_e}E_R$ under the harmonic oscillator approximation. However, when the lattice depth is in the region below $\sim 30E_R$, which is the typical value for measurement, the harmonic oscillator approximation is not valid. Therefore, we

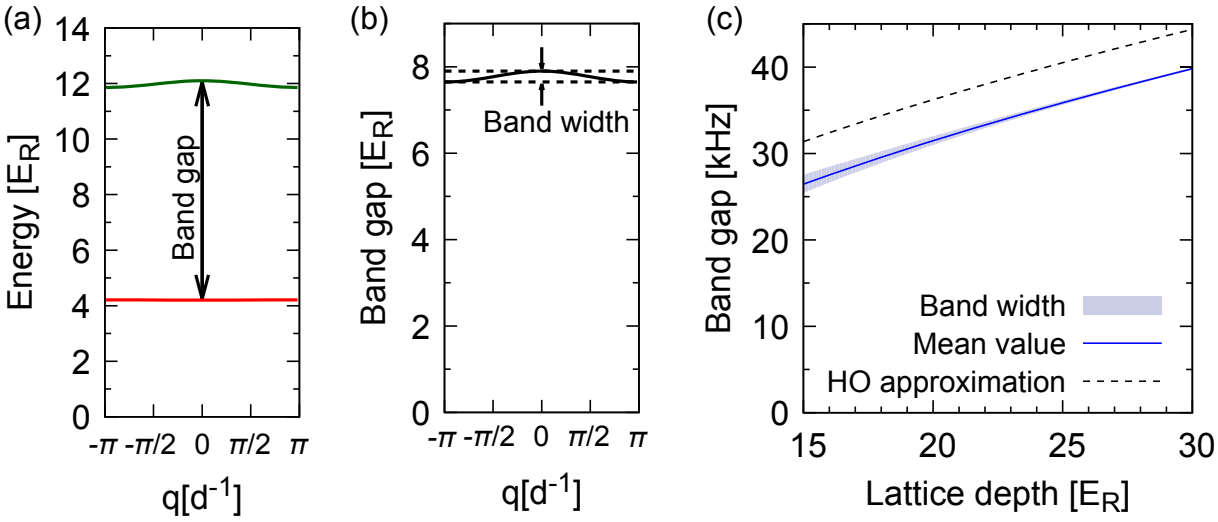

Figure D.1.1: (a) Band structure in the lattice depth of 20 E_R. The horizontal axis is the quasi momentum q. The red and green lines represent the 0th and the 1st band, respectively. (b) Band gap between the 0th and 1st band in the lattice depth of 20 E_R. Band width is defined as in the figure. (c) Band gap as a function of the lattice depth. The shaded area represents the band width, which shows that the band width decreases for deeper lattice depth compared with the mean value of the band gap. For comparison, the band gap calculated under the harmonic oscillator (HO) approximation is shown.

numerically calculate the band gap. Figure D.1.1 shows the band gap and the band width as a function of the lattice depth of the $^3P_2$ state.

In this calculation, we define the mean value of the band gap as the average over the quasi-momentum q in the 1st Brillouin zone. In the deep optical lattice, the 0th and 1st bands are flat enough to ignore the effect of the finite band width in the evaluation of the s_e from the result of the spectroscopy. For the $^3P_2$ state, the polarizability α_e depends on the magnetic sublevels m_J and the angle between the quantization axis and the polarization of the lattice beam θ. Thus, in the measurement, we perform the spectroscopy with five different conditions, varying m_J and θ.

D.2 Spectroscopy

Figure D.2.1 is the typical spectrum of the carrier and the blue-sideband transitions. The lattice depth is fixed at 20 E_R for the $^1S_0$ state, which is calibrated with the pulsed lattice method [170]. To precisely determine the band gap, we obtain four spectra in each condition. We fit the data to the multiple Gaussian functions and obtain the interval of the two peaks. The band gap is evaluated by calculating the weighted average of the four results. By comparing the measured band gap with the numerical calculation (Fig. D.1.1), we determine the lattice depth s_e for the $^3P_2$ state. Because the lattice depth is fixed at the 20 E_R for the $^1S_0$ state, the ratio of the polarizability can be derived as $\alpha_e/\alpha_g = s_e/20$.

Table D.2.1 shows the obtained ratio of the polarizability. We use these values in the

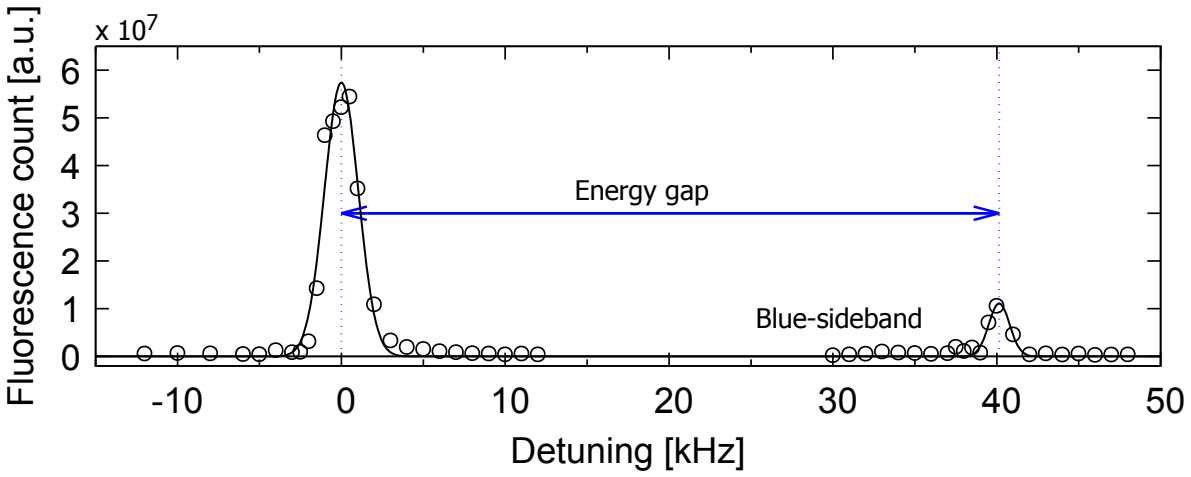

Figure D.2.1: Spectrum of the carrier and blue-sideband transitions. The lattice depth is $20E_R$ for the $^1S_0$ state. The magnetic sublevel is $m_J = -2$, and the angle between the magnetization axis and the polarization is $\theta = 0°$. We obtain four data sets in each condition.

measurement of the on-site interaction between the $^3P_2$ atoms.

We convert these values of the ratio into the polarizability of the $^3P_2$ state (Tab. D.2.2) with the known value of $\alpha_g = 37.9\text{Hz}/(\text{W}/\text{cm}^2)$ [171].

Table D.2.1: Ratio of the polarizability $\alpha_e^{(m_J)}/\alpha_g$. m_J is the magnetic sublevel and θ is the angle between the quantization axis and the polarization of the lattice beam θ.

	$\theta = 90°$	$\theta = 0°$
$\alpha_e^{(0)}/\alpha_g$	1.32(4)	1.023(10)
$\alpha_e^{(-1)}/\alpha_g$	1.22(8)	-
$\alpha_e^{(-2)}/\alpha_g$	1.132(8)	1.43(5)

Table D.2.2: Polarizability of the $^3P_2$ state $\alpha_e^{(m_J)}$.

	$\theta = 90°$	$\theta = 0°$	Unit
$\alpha_e^{(0)}$	49.8(1.4)	38.8(4)	Hz/(W/cm^2)
$\alpha_e^{(-1)}$	46(3)	-	Hz/(W/cm^2)
$\alpha_e^{(-2)}$	42.9(3)	54.1(1.7)	Hz/(W/cm^2)

Bibliography

[1] Michael A. Nielsen and Isaac L. Chuang. Quantum computation and quantum information.

[2] Christopher Monroe and Jungsang Kim. Scaling the ion trap quantum processor. *Science*, 339(6124):1164–1169, 2013.

[3] David D. Awschalom, Lee C. Bassett, Andrew S. Dzurak, Evelyn L. Hu, and Jason R. Petta. Quantum spintronics: engineering and manipulating atom-like spins in semiconductors. *Science*, 339(6124):1174–1179, 2013.

[4] Michel H. Devoret and Robert J. Schoelkopf. Superconducting circuits for quantum information: an outlook. *Science*, 339(6124):1169–1174, 2013.

[5] Andrew J. Daley. Quantum trajectories and open many-body quantum systems. *Advances in Physics*, 63(2):77–149, 2014.

[6] Markus Müller, Sebastian Diehl, Guido Pupillo, and Peter Zoller. Engineered open systems and quantum simulations with atoms and ions. In *Advances in atomic, molecular, and optical physics*, volume 61, pages 1–80. Elsevier, 2012.

[7] Jean Brossel, Alfred Kastler, and Jacques Winter. Gréation optique d'une inégalité de population entre les sous-niveaux zeeman de l'état fondamental des atomes. *J. phys. radium*, 13(12):668–668, 1952.

[8] WB Hawkins and RH Dicke. The polarization of sodium atoms. *Physical Review*, 91(4):1008, 1953.

[9] D. Leibfried, R. Blatt, C. Monroe, and D. Wineland. Quantum dynamics of single trapped ions. *Rev. Mod. Phys.*, 75:281–324, Mar 2003.

[10] P Oscar Boykin, Tal Mor, Vwani Roychowdhury, Farrokh Vatan, and Rutger Vrijen. Algorithmic cooling and scalable NMR quantum computers. *Proceedings of the National Academy of Sciences*, 99(6):3388–3393, 2002.

[11] Jonathan Baugh, Osama Moussa, Colm A Ryan, Ashwin Nayak, and Raymond Laflamme. Experimental implementation of heat-bath algorithmic cooling using solid-state nuclear magnetic resonance. *Nature*, 438(7067):470, 2005.

[12] Lukas M Sieberer, Michael Buchhold, and Sebastian Diehl. Keldysh field theory for driven open quantum systems. *Reports on Progress in Physics*, 79(9):096001, 2016.

[13] Rainer Blatt and Christian F Roos. Quantum simulations with trapped ions. *Nature Physics*, 8(4):277, 2012.

[14] Justin G. Bohnet, Brian C. Sawyer, Joseph W. Britton, Michael L. Wall, Ana Maria Rey, Michael Foss-Feig, and John J. Bollinger. Quantum spin dynamics and entanglement generation with hundreds of trapped ions. *Science*, 352(6291):1297–1301, 2016.

[15] Helmut Ritsch, Peter Domokos, Ferdinand Brennecke, and Tilman Esslinger. Cold atoms in cavity-generated dynamical optical potentials. *Rev. Mod. Phys.*, 85:553–601, Apr 2013.

[16] Iacopo Carusotto and Cristiano Ciuti. Quantum fluids of light. *Rev. Mod. Phys.*, 85:299–366, Feb 2013.

[17] Andrew A. Houck, Hakan E. Türeci, and Jens Koch. On-chip quantum simulation with superconducting circuits. *Nature Physics*, 8(4):292, 2012.

[18] Mattias Fitzpatrick, Neereja M. Sundaresan, Andy C. Y. Li, Jens Koch, and Andrew A. Houck. Observation of a dissipative phase transition in a one-dimensional circuit QED lattice. *Phys. Rev. X*, 7:011016, Feb 2017.

[19] Goran Lindblad. On the generators of quantum dynamical semigroups. *Communications in Mathematical Physics*, 48(2):119–130, 1976.

[20] Howard Carmichael. *An open systems approach to quantum optics: lectures presented at the Université Libre de Bruxelles, October 28 to November 4, 1991*, volume 18. Springer Science & Business Media, 2009.

[21] M. B. Plenio and P. L. Knight. The quantum-jump approach to dissipative dynamics in quantum optics. *Rev. Mod. Phys.*, 70:101–144, Jan 1998.

[22] Jean Dalibard, Yvan Castin, and Klaus Mølmer. Wave-function approach to dissipative processes in quantum optics. *Phys. Rev. Lett.*, 68:580–583, Feb 1992.

[23] Klaus Mølmer, Yvan Castin, and Jean Dalibard. Monte Carlo wave-function method in quantum optics. *JOSA B*, 10(3):524–538, 1993.

[24] R. Dum, P. Zoller, and H. Ritsch. Monte Carlo simulation of the atomic master equation for spontaneous emission. *Phys. Rev. A*, 45:4879–4887, Apr 1992.

[25] R. Dum, A. S. Parkins, P. Zoller, and C. W. Gardiner. Monte Carlo simulation of master equations in quantum optics for vacuum, thermal, and squeezed reservoirs. *Phys. Rev. A*, 46:4382–4396, Oct 1992.

[26] Inés de Vega and Daniel Alonso. Dynamics of non-markovian open quantum systems. *Rev. Mod. Phys.*, 89:015001, Jan 2017.

[27] Ramy El-Ganainy, Konstantinos G. Makris, Mercedeh Khajavikhan, Ziad H. Musslimani, Stefan Rotter, and Demetrios N. Christodoulides. Non-Hermitian physics and PT symmetry. *Nature Physics*, 14(1):11, 2018.

[28] Yuto Ashida, Shunsuke Furukawa, and Masahito Ueda. Quantum critical behavior influenced by measurement backaction in ultracold gases. *Phys. Rev. A*, 94:053615, Nov 2016.

[29] Yuto Ashida, Shunsuke Furukawa, and Masahito Ueda. Parity-time-symmetric quantum critical phenomena. *Nature communications*, 8:15791, 2017.

[30] Masaya Nakagawa, Norio Kawakami, and Masahito Ueda. Non-Hermitian Kondo effect in ultracold alkaline-earth atoms. *Phys. Rev. Lett.*, 121:203001, Nov 2018.

[31] Zongping Gong, Yuto Ashida, Kohei Kawabata, Kazuaki Takasan, Sho Higashikawa, and Masahito Ueda. Topological phases of non-Hermitian systems. *Phys. Rev. X*, 8:031079, Sep 2018.

[32] Mike H Anderson, Jason R Ensher, Michael R Matthews, Carl E Wieman, and Eric A Cornell. Observation of Bose-Einstein condensation in a dilute atomic vapor. *science*, 269(5221):198–201, 1995.

[33] C. C. Bradley, C. A. Sackett, J. J. Tollett, and R. G. Hulet. Evidence of Bose-Einstein condensation in an atomic gas with attractive interactions. *Phys. Rev. Lett.*, 75:1687–1690, Aug 1995.

[34] K. B. Davis, M. O. Mewes, M. R. Andrews, N. J. van Druten, D. S. Durfee, D. M. Kurn, and W. Ketterle. Bose-Einstein condensation in a gas of sodium atoms. *Phys. Rev. Lett.*, 75:3969–3973, Nov 1995.

[35] Brian DeMarco and Deborah S Jin. Onset of Fermi degeneracy in a trapped atomic gas. *Science*, 285(5434):1703–1706, 1999.

[36] D. Jaksch, C. Bruder, J. I. Cirac, C. W. Gardiner, and P. Zoller. Cold bosonic atoms in optical lattices. *Phys. Rev. Lett.*, 81:3108–3111, Oct 1998.

[37] Markus Greiner, Olaf Mandel, Tilman Esslinger, Theodor W Hänsch, and Immanuel Bloch. Quantum phase transition from a superfluid to a Mott insulator in a gas of ultracold atoms. *nature*, 415(6867):39, 2002.

[38] Markus Greiner, Olaf Mandel, Theodor W Hänsch, and Immanuel Bloch. Collapse and revival of the matter wave field of a bose–einstein condensate. *Nature*, 419(6902):51, 2002.

[39] S. Trotzky, L. Pollet, F. Gerbier, U. Schnorrberger, Immanuel Bloch, NV. Prokof ' Ev, Boris Svistunov, and M. Troyer. Suppression of the critical temperature for superfluidity near the Mott transition. *Nature Physics*, 6(12):998, 2010.

[40] Chen-Lung Hung, Xibo Zhang, Nathan Gemelke, and Cheng Chin. Observation of scale invariance and universality in two-dimensional Bose gases. *Nature*, 470(7333):236, 2011.

[41] Xibo Zhang, Chen-Lung Hung, Shih-Kuang Tung, and Cheng Chin. Observation of quantum criticality with ultracold atoms in optical lattices. *Science*, page 1217990, 2012.

[42] BJ Bloom, TL Nicholson, JR Williams, SL Campbell, M Bishof, X Zhang, W Zhang, SL Bromley, and J Ye. An optical lattice clock with accuracy and stability at the 10^{-18} level. *Nature*, 506(7486):71, 2014.

[43] Shinya Kato, Kensuke Inaba, Seiji Sugawa, Kosuke Shibata, Ryuta Yamamoto, Makoto Yamashita, and Yoshiro Takahashi. Laser spectroscopic probing of coexisting superfluid and insulating states of an atomic Bose-Hubbard system. *Nature communications*, 7:11341, 2016.

[44] Andrei Derevianko and Caleb C. Cannon. Quantum computing with magnetically interacting atoms. *Phys. Rev. A*, 70:062319, Dec 2004.

[45] Andrew J. Daley, Martin M. Boyd, Jun Ye, and Peter Zoller. Quantum computing with alkaline-earth-metal atoms. *Phys. Rev. Lett.*, 101:170504, Oct 2008.

[46] R. Stock, N. S. Babcock, M. G. Raizen, and B. C. Sanders. Entanglement of group-II-like atoms with fast measurement for quantum information processing. *Phys. Rev. A*, 78:022301, Aug 2008.

[47] K. Shibata, S. Kato, A. Yamaguchi, S. Uetake, and Y. Takahashi. A scalable quantum computer with ultranarrow optical transition of ultracold neutral atoms in an optical lattice. *Applied Physics B*, 97(4):753, 2009.

[48] A. V. Gorshkov, A. M. Rey, A. J. Daley, M. M. Boyd, J. Ye, P. Zoller, and M. D. Lukin. Alkaline-earth-metal atoms as few-qubit quantum registers. *Phys. Rev. Lett.*, 102:110503, Mar 2009.

[49] Andrew J Daley. Quantum computing and quantum simulation with group-II atoms. *Quantum Information Processing*, 10(6):865, 2011.

[50] G. Pagano, F. Scazza, and M. Foss-Feig. Fast and scalable quantum information processing with two-electron atoms in optical tweezer arrays, 2018.

[51] Michael Foss-Feig, Michael Hermele, and Ana Maria Rey. Probing the Kondo lattice model with alkaline-earth-metal atoms. *Phys. Rev. A*, 81:051603, May 2010.

[52] Masaya Nakagawa and Norio Kawakami. Laser-induced Kondo effect in ultracold alkaline-earth fermions. *Phys. Rev. Lett.*, 115:165303, Oct 2015.

[53] Ren Zhang, Deping Zhang, Yanting Cheng, Wei Chen, Peng Zhang, and Hui Zhai. Kondo effect in alkaline-earth-metal atomic gases with confinement-induced resonances. *Phys. Rev. A*, 93:043601, Apr 2016.

[54] Márton Kanász-Nagy, Yuto Ashida, Tao Shi, Cătălin Pa şcu Moca, Tatsuhiko N. Ikeda, Simon Fölling, J. Ignacio Cirac, Gergely Zaránd, and Eugene A. Demler. Exploring the anisotropic Kondo model in and out of equilibrium with alkaline-earth atoms. *Phys. Rev. B*, 97:155156, Apr 2018.

[55] Francesco Scazza, Christian Hofrichter, Moritz Höfer, PC De Groot, Immanuel Bloch, and Simon Fölling. Observation of two-orbital spin-exchange interactions with ultracold SU (N)-symmetric fermions. *Nature Physics*, 10(10):779, 2014.

[56] G. Cappellini, M. Mancini, G. Pagano, P. Lombardi, L. Livi, M. Siciliani de Cumis, P. Cancio, M. Pizzocaro, D. Calonico, F. Levi, C. Sias, J. Catani, M. Inguscio, and L. Fallani. Direct observation of coherent interorbital spin-exchange dynamics. *Phys. Rev. Lett.*, 113:120402, Sep 2014.

[57] M. Höfer, L. Riegger, F. Scazza, C. Hofrichter, D. R. Fernandes, M. M. Parish, J. Levinsen, I. Bloch, and S. Fölling. Observation of an orbital interaction-induced Feshbach resonance in ^{173}Yb. *Phys. Rev. Lett.*, 115:265302, Dec 2015.

[58] Xiaohang Zhang, Michael Bishof, Sarah L Bromley, Christina V Kraus, Marianna S Safronova, Peter Zoller, Ana Maria Rey, and J Ye. Spectroscopic observation of SU (N)-symmetric interactions in Sr orbital magnetism. *science*, 345(6203):1467–1473, 2014.

[59] L. Riegger, N. Darkwah Oppong, M. Höfer, D. R. Fernandes, I. Bloch, and S. Fölling. Localized magnetic moments with tunable spin exchange in a gas of ultracold fermions. *Phys. Rev. Lett.*, 120:143601, Apr 2018.

[60] Koki Ono, Jun Kobayashi, Yoshiki Amano, Koji Sato, and Yoshiro Takahashi. Antiferromagnetic interorbital spin-exchange interaction of ^{171}Yb. *arXiv preprint arXiv:1810.00536*, 2018.

[61] Shinya Kato, Seiji Sugawa, Kosuke Shibata, Ryuta Yamamoto, and Yoshiro Takahashi. Control of resonant interaction between electronic ground and excited states. *Phys. Rev. Lett.*, 110:173201, Apr 2013.

[62] Shintaro Taie, Shunsuke Watanabe, Tomohiro Ichinose, and Yoshiro Takahashi. Feshbach-resonance-enhanced coherent atom-molecule conversion with ultranarrow photoassociation resonance. *Phys. Rev. Lett.*, 116:043202, Jan 2016.

[63] Yosuke Takasu, Yoshiaki Fukushima, Yusuke Nakamura, and Yoshiro Takahashi. Magnetoassociation of a Feshbach molecule and spin-orbit interaction between the ground and electronically excited states. *Phys. Rev. A*, 96:023602, Aug 2017.

[64] Sebastian Diehl, A. Micheli, A. Kantian, B. Kraus, HP. Büchler, and P. Zoller. Quantum states and phases in driven open quantum systems with cold atoms. *Nature Physics*, 4(11):878, 2008.

[65] D. Witthaut, F. Trimborn, and S. Wimberger. Dissipation induced coherence of a two-mode Bose-Einstein condensate. *Phys. Rev. Lett.*, 101:200402, Nov 2008.

[66] Frank Verstraete, Michael M. Wolf, and J. Ignacio Cirac. Quantum computation and quantum-state engineering driven by dissipation. *Nature physics*, 5(9):633, 2009.

[67] Y.-J. Han, Y.-H. Chan, W. Yi, A. J. Daley, S. Diehl, P. Zoller, and L.-M. Duan. Stabilization of the p-wave superfluid state in an optical lattice. *Phys. Rev. Lett.*, 103:070404, Aug 2009.

[68] Emanuele G. Dalla Torre, Eugene Demler, Thierry Giamarchi, and Ehud Altman. Quantum critical states and phase transitions in the presence of non-equilibrium noise. *Nature Physics*, 6(10):806, 2010.

[69] Sebastian Diehl, Andrea Tomadin, Andrea Micheli, Rosario Fazio, and Peter Zoller. Dynamical phase transitions and instabilities in open atomic many-body systems. *Phys. Rev. Lett.*, 105:015702, Jul 2010.

[70] Andrea Tomadin, Sebastian Diehl, and Peter Zoller. Nonequilibrium phase diagram of a driven and dissipative many-body system. *Phys. Rev. A*, 83:013611, Jan 2011.

[71] Alexandre Le Boité, Giuliano Orso, and Cristiano Ciuti. Steady-state phases and tunneling-induced instabilities in the driven dissipative Bose-Hubbard model. *Phys. Rev. Lett.*, 110:233601, Jun 2013.

[72] Ivana Vidanović, Daniel Cocks, and Walter Hofstetter. Dissipation through localized loss in bosonic systems with long-range interactions. *Phys. Rev. A*, 89:053614, May 2014.

[73] K. Stannigel, P. Hauke, D. Marcos, M. Hafezi, S. Diehl, M. Dalmonte, and P. Zoller. Constrained dynamics via the Zeno effect in quantum simulation: Implementing non-Abelian lattice gauge theories with cold atoms. *Phys. Rev. Lett.*, 112:120406, Mar 2014.

[74] Niels Syassen, Dominik M. Bauer, Matthias Lettner, Thomas Volz, Daniel Dietze, Juan J. Garcia-Ripoll, J. Ignacio Cirac, Gerhard Rempe, and Stephan Dürr. Strong dissipation inhibits losses and induces correlations in cold molecular gases. *Science*, 320(5881):1329–1331, 2008.

[75] Baidyanath Misra and EC. George Sudarshan. The Zeno's paradox in quantum theory. *Journal of Mathematical Physics*, 18(4):756–763, 1977.

[76] Bo Yan, Steven A. Moses, Bryce Gadway, Jacob P. Covey, Kaden RA. Hazzard, Ana Maria Rey, Deborah S. Jin, and Jun Ye. Observation of dipolar spin-exchange interactions with lattice-confined polar molecules. *Nature*, 501(7468):521–525, 2013.

[77] G. Barontini, R. Labouvie, F. Stubenrauch, A. Vogler, V. Guarrera, and H. Ott. Controlling the dynamics of an open many-body quantum system with localized dissipation. *Phys. Rev. Lett.*, 110:035302, Jan 2013.

[78] Ralf Labouvie, Bodhaditya Santra, Simon Heun, Sandro Wimberger, and Herwig Ott. Negative differential conductivity in an interacting quantum gas. *Phys. Rev. Lett.*, 115:050601, Jul 2015.

[79] Ralf Labouvie, Bodhaditya Santra, Simon Heun, and Herwig Ott. Bistability in a driven-dissipative superfluid. *Phys. Rev. Lett.*, 116:235302, Jun 2016.

[80] Y. S. Patil, S. Chakram, and M. Vengalattore. Measurement-induced localization of an ultracold lattice gas. *Phys. Rev. Lett.*, 115:140402, Oct 2015.

[81] M. J. Mark, E. Haller, K. Lauber, J. G. Danzl, A. Janisch, H. P. Büchler, A. J. Daley, and H.-C. Nägerl. Preparation and spectroscopy of a metastable Mott-insulator state with attractive interactions. *Phys. Rev. Lett.*, 108:215302, May 2012.

[82] Henrik P. Lüschen, Pranjal Bordia, Sean S. Hodgman, Michael Schreiber, Saubhik Sarkar, Andrew J. Daley, Mark H. Fischer, Ehud Altman, Immanuel Bloch, and Ulrich Schneider. Signatures of many-body localization in a controlled open quantum system. *Phys. Rev. X*, 7:011034, Mar 2017.

[83] Antonio Rubio-Abadal, Jae-yoon Choi, Johannes Zeiher, Simon Hollerith, Jun Rui, Immanuel Bloch, and Christian Gross. Probing many-body localization in the presence of a quantum bath. *arXiv preprint arXiv:1805.00056*, 2018.

[84] Takafumi Tomita, Shuta Nakajima, Ippei Danshita, Yosuke Takasu, and Yoshiro Takahashi. Observation of the Mott insulator to superfluid crossover of a driven-dissipative Bose-Hubbard system. *Science advances*, 3(12):e1701513, 2017.

[85] Takafumi Tomita, Shuta Nakajima, Yosuke Takasu, and Yoshiro Takahashi. Dissipative Bose-Hubbard system with intrinsic two-body loss. *arXiv preprint arXiv:1809.09989*, 2018.

[86] Koen Sponselee, Lukas Freystatzky, Benjamin Abeln, Marcel Diem, Bastian Hundt, André Kochanke, Thomas Ponath, Bodhaditya Santra, Ludwig Mathey, Klaus Sengstock, and Christoph Becker. Dynamics of ultracold quantum gases in the dissipative Fermi-Hubbard model. *Quantum Science and Technology*, 4(1):014002, 2019.

[87] A. J. Daley, J. M. Taylor, S. Diehl, M. Baranov, and P. Zoller. Atomic three-body loss as a dynamical three-body interaction. *Phys. Rev. Lett.*, 102:040402, Jan 2009.

[88] Dirk Hansen and Andreas Hemmerich. Observation of multichannel collisions of cold metastable calcium atoms. *Phys. Rev. Lett.*, 96:073003, Feb 2006.

[89] A. Traverso, R. Chakraborty, Y. N. Martinez de Escobar, P. G. Mickelson, S. B. Nagel, M. Yan, and T. C. Killian. Inelastic and elastic collision rates for triplet states of ultracold strontium. *Phys. Rev. A*, 79:060702, Jun 2009.

[90] A. Yamaguchi, S. Uetake, D. Hashimoto, J. M. Doyle, and Y. Takahashi. Inelastic collisions in optically trapped ultracold metastable ytterbium. *Phys. Rev. Lett.*, 101:233002, Dec 2008.

[91] Satoshi Uetake, Ryo Murakami, John M. Doyle, and Yoshiro Takahashi. Spin-dependent collision of ultracold metastable atoms. *Phys. Rev. A*, 86:032712, Sep 2012.

[92] Purbasha Halder, Hannes Winter, and Andreas Hemmerich. Inelastic collisions of optically trapped metastable calcium atoms. *Phys. Rev. A*, 88:063639, Dec 2013.

[93] L. Franchi, LF. Livi, G. Cappellini, G. Binella, M. Inguscio, J. Catani, and L. Fallani. State-dependent interactions in ultracold ^{174}Yb probed by optical clock spectroscopy. *New Journal of Physics*, 19(10):103037, 2017.

[94] R. Bouganne, M. Bosch Aguilera, A. Dareau, E. Soave, J. Beugnon, and F. Gerbier. Clock spectroscopy of interacting bosons in deep optical lattices. *New Journal of Physics*, 19(11):113006, 2017.

[95] R. M. Bradley and S. Doniach. Quantum fluctuations in chains of Josephson junctions. *Phys. Rev. B*, 30:1138–1147, Aug 1984.

[96] Matthew P. A. Fisher, Peter B. Weichman, G. Grinstein, and Daniel S. Fisher. Boson localization and the superfluid-insulator transition. *Phys. Rev. B*, 40:546–570, Jul 1989.

[97] K. Sheshadri, HR. Krishnamurthy, Rahul Pandit, and TV. Ramakrishnan. Superfluid and insulating phases in an interacting-boson model: Mean-field theory and the RPA. *EPL (Europhysics Letters)*, 22(4):257, 1993.

[98] D. van Oosten, P. van der Straten, and H. T. C. Stoof. Quantum phases in an optical lattice. *Phys. Rev. A*, 63:053601, Apr 2001.

[99] B. Capogrosso-Sansone, N. V. Prokof'ev, and B. V. Svistunov. Phase diagram and thermodynamics of the three-dimensional Bose-Hubbard model. *Phys. Rev. B*, 75:134302, Apr 2007.

[100] Fabrice Gerbier, Artur Widera, Simon Fölling, Olaf Mandel, Tatjana Gericke, and Immanuel Bloch. Phase coherence of an atomic Mott insulator. *Phys. Rev. Lett.*, 95:050404, Jul 2005.

[101] Fabrice Gerbier, Artur Widera, Simon Fölling, Olaf Mandel, Tatjana Gericke, and Immanuel Bloch. Interference pattern and visibility of a Mott insulator. *Phys. Rev. A*, 72:053606, Nov 2005.

[102] Manuel Endres, Marc Cheneau, Takeshi Fukuhara, Christof Weitenberg, Peter Schauß, Christian Gross, Leonardo Mazza, Mari Carmen Banuls, L Pollet, Immanuel Bloch, et al. Observation of correlated particle-hole pairs and string order in low-dimensional Mott insulators. *Science*, 334(6053):200–203, 2011.

[103] Heinz-Peter Breuer, Francesco Petruccione, et al. *The theory of open quantum systems*. Oxford University Press on Demand, 2002.

[104] S. Dürr, J. J. García-Ripoll, N. Syassen, D. M. Bauer, M. Lettner, J. I. Cirac, and G. Rempe. Lieb-liniger model of a dissipation-induced Tonks-Girardeau gas. *Phys. Rev. A*, 79:023614, Feb 2009.

[105] J. D. Miller, R. A. Cline, and D. J. Heinzen. Photoassociation spectrum of ultracold Rb atoms. *Phys. Rev. Lett.*, 71:2204–2207, Oct 1993.

[106] P. D. Lett, K. Helmerson, W. D. Phillips, L. P. Ratliff, S. L. Rolston, and M. E. Wagshul. Spectroscopy of Na_2 by photoassociation of laser-cooled Na. *Phys. Rev. Lett.*, 71:2200–2203, Oct 1993.

[107] E. R. I. Abraham, W. I. McAlexander, C. A. Sackett, and Randall G. Hulet. Spectroscopic determination of the s-wave scattering length of lithium. *Phys. Rev. Lett.*, 74:1315–1318, Feb 1995.

[108] Y. B. Band and P. S. Julienne. Ultracold-molecule production by laser-cooled atom photoassociation. *Phys. Rev. A*, 51:R4317–R4320, Jun 1995.

[109] Tim Rom, Thorsten Best, Olaf Mandel, Artur Widera, Markus Greiner, Theodor W. Hänsch, and Immanuel Bloch. State selective production of molecules in optical lattices. *Phys. Rev. Lett.*, 93:073002, Aug 2004.

[110] Kevin M. Jones, Eite Tiesinga, Paul D. Lett, and Paul S. Julienne. Ultracold photoassociation spectroscopy: Long-range molecules and atomic scattering. *Rev. Mod. Phys.*, 78:483–535, May 2006.

[111] Reginaldo Napolitano, John Weiner, Carl J. Williams, and Paul S. Julienne. Line shapes of high resolution photoassociation spectra of optically cooled atoms. *Phys. Rev. Lett.*, 73:1352–1355, Sep 1994.

[112] John L. Bohn and P. S. Julienne. Semianalytic theory of laser-assisted resonant cold collisions. *Phys. Rev. A*, 60:414–425, Jul 1999.

[113] P. Pillet, A. Crubellier, A. Bleton, O. Dulieu, P. Nosbaum, I. Mourachko, and F. Masnou-Seeuws. Photoassociation in a gas of cold alkali atoms: I. perturbative quantum approach. *Journal of Physics B: Atomic, Molecular and Optical Physics*, 30(12):2801, 1997.

[114] John L. Bohn and P. S. Julienne. Prospects for influencing scattering lengths with far-off-resonant light. *Phys. Rev. A*, 56:1486–1491, Aug 1997.

[115] M. Borkowski, R. Ciuryło, P. S. Julienne, S. Tojo, K. Enomoto, and Y. Takahashi. Line shapes of optical Feshbach resonances near the intercombination transition of bosonic ytterbium. *Phys. Rev. A*, 80:012715, Jul 2009.

[116] M Borkowski. Optyczna kontrola oddziaływań miedzyatomowych w ultrazimnym iterbie. *Master thesis, Uniwersytet Mikołaja Kopernika*, 2010.

[117] Yosuke Takasu, Kenichi Maki, Kaduki Komori, Tetsushi Takano, Kazuhito Honda, Mitsutaka Kumakura, Tsutomu Yabuzaki, and Yoshiro Takahashi. Spin-singlet Bose-Einstein condensation of two-electron atoms. *Phys. Rev. Lett.*, 91:040404, Jul 2003.

[118] Takeshi Fukuhara, Seiji Sugawa, and Yoshiro Takahashi. Bose-Einstein condensation of an ytterbium isotope. *Phys. Rev. A*, 76:051604, Nov 2007.

[119] Takeshi Fukuhara, Seiji Sugawa, Yosuke Takasu, and Yoshiro Takahashi. All-optical formation of quantum degenerate mixtures. *Phys. Rev. A*, 79:021601, Feb 2009.

[120] Seiji Sugawa, Rekishu Yamazaki, Shintaro Taie, and Yoshiro Takahashi. Bose-Einstein condensate in gases of rare atomic species. *Phys. Rev. A*, 84:011610, Jul 2011.

[121] Takeshi Fukuhara, Yosuke Takasu, Mitsutaka Kumakura, and Yoshiro Takahashi. Degenerate fermi gases of ytterbium. *Phys. Rev. Lett.*, 98:030401, Jan 2007.

[122] Seiji Sugawa, Kensuke Inaba, Shintaro Taie, Rekishu Yamazaki, Makoto Yamashita, and Yoshiro Takahashi. Interaction and filling-induced quantum phases of dual Mott insulators of bosons and fermions. *Nature Physics*, 7(8):642, 2011.

[123] Sansonetti J. E. and W. C. Martin. *Handbook of Basic Atomic Spectroscopic Data*, 2013 (accessed October 10, 2018). https://www.nist.gov/pml/handbook-basic-atomic-spectroscopic-data.

[124] Y. Takasu, K. Komori, K. Honda, M. Kumakura, T. Yabuzaki, and Y. Takahashi. Photoassociation spectroscopy of laser-cooled ytterbium atoms. *Phys. Rev. Lett.*, 93:123202, Sep 2004.

[125] Satoshi Tojo, Masaaki Kitagawa, Katsunari Enomoto, Yutaka Kato, Yosuke Takasu, Mitsutaka Kumakura, and Yoshiro Takahashi. High-resolution photoassociation spectroscopy of ultracold ytterbium atoms by using the intercombination transition. *Phys. Rev. Lett.*, 96:153201, Apr 2006.

[126] K. Enomoto, M. Kitagawa, K. Kasa, S. Tojo, and Y. Takahashi. Determination of the s-wave scattering length and the C_6 van der waals coefficient of ^{174}Yb via photoassociation spectroscopy. *Phys. Rev. Lett.*, 98:203201, May 2007.

[127] Masaaki Kitagawa, Katsunari Enomoto, Kentaro Kasa, Yoshiro Takahashi, Roman Ciuryło, Pascal Naidon, and Paul S. Julienne. Two-color photoassociation spectroscopy of ytterbium atoms and the precise determinations of s-wave scattering lengths. *Phys. Rev. A*, 77:012719, Jan 2008.

[128] K. Honda, Y. Takahashi, T. Kuwamoto, M. Fujimoto, K. Toyoda, K. Ishikawa, and T. Yabuzaki. Magneto-optical trapping of Yb atoms and a limit on the branching ratio of the $^1P_1$ state. *Phys. Rev. A*, 59:R934–R937, Feb 1999.

[129] K.B. Blagoev and V.A. Komarovskii. Lifetimes of levels of neutral and singly ionized lanthanide atoms. *Atomic Data and Nuclear Data Tables*, 56(1):1 – 40, 1994.

[130] Dipankar Das, Sachin Barthwal, Ayan Banerjee, and Vasant Natarajan. Absolute frequency measurements in Yb with 0.08 ppb uncertainty: Isotope shifts and hyperfine structure in the 399-nm $^1S_0 \rightarrow {}^1P_1$ line. *Phys. Rev. A*, 72:032506, Sep 2005.

[131] Kanhaiya Pandey, Alok K. Singh, P. V. Kiran Kumar, M. V. Suryanarayana, and Vasant Natarajan. Isotope shifts and hyperfine structure in the 555.8-nm $^1S_0 \rightarrow {}^3P_1$ line of Yb. *Phys. Rev. A*, 80:022518, Aug 2009.

[132] S. G. Porsev, Yu. G. Rakhlina, and M. G. Kozlov. Electric-dipole amplitudes, lifetimes, and polarizabilities of the low-lying levels of atomic ytterbium. *Phys. Rev. A*, 60:2781–2785, Oct 1999.

[133] Sergey G. Porsev and Andrei Derevianko. Hyperfine quenching of the metastable $^3P_{0,2}$ states in divalent atoms. *Phys. Rev. A*, 69:042506, Apr 2004.

[134] Daniel A Steck. Quantum and atom optics. *Oregon Center for Optics and Department of Physics, University of Oregon*, 47, 2007.

[135] H Ozawa. Ultracold ytterbium atoms in a tunable non-primitive optical lattice. *Ph. D thesis, Kyoto University*, 2018.

[136] Michael M. T. Loy. Observation of population inversion by optical adiabatic rapid passage. *Phys. Rev. Lett.*, 32:814–817, Apr 1974.

[137] C. Haimberger, J. Kleinert, O. Dulieu, and NP. Bigelow. Processes in the formation of ultracold NaCs. *Journal of Physics B: Atomic, Molecular and Optical Physics*, 39(19):S957, 2006.

[138] S. D. Kraft, M. Mudrich, M. U. Staudt, J. Lange, O. Dulieu, R. Wester, and M. Weidemüller. Saturation of Cs_2 photoassociation in an optical dipole trap. *Phys. Rev. A*, 71:013417, Jan 2005.

[139] U. Schlöder, C. Silber, T. Deuschle, and C. Zimmermann. Saturation in heteronuclear photoassociation of $^6Li^7Li$. *Phys. Rev. A*, 66:061403, Dec 2002.

[140] M. Junker, D. Dries, C. Welford, J. Hitchcock, Y. P. Chen, and R. G. Hulet. Photoassociation of a Bose-Einstein condensate near a Feshbach resonance. *Phys. Rev. Lett.*, 101:060406, Aug 2008.

[141] V. G. Rousseau and P. J. H. Denteneer. Quantum phases of mixtures of atoms and molecules on optical lattices. *Phys. Rev. A*, 77:013609, Jan 2008.

[142] Gavin K. Brennen, Guido Pupillo, Ana Maria Rey, Charles W. Clark, and Carl J. Williams. Scalable register initialization for quantum computing in an optical lattice. *Journal of Physics B: Atomic, Molecular and Optical Physics*, 38(11):1687, 2005.

[143] Juan José García-Ripoll, Stephan Dürr, Niels Syassen, Dominik M. Bauer, Matthias Lettner, Gerhard Rempe, and J. Ignacio Cirac. Dissipation-induced hard-core boson gas in an optical lattice. *New Journal of Physics*, 11(1):013053, 2009.

[144] Daniel S. Rokhsar and B. G. Kotliar. Gutzwiller projection for bosons. *Phys. Rev. B*, 44:10328–10332, Nov 1991.

[145] Werner Krauth, Michel Caffarel, and Jean-Philippe Bouchaud. Gutzwiller wave function for a model of strongly interacting bosons. *Phys. Rev. B*, 45:3137–3140, Feb 1992.

[146] M. Aidelsburger, M. Atala, S. Nascimbène, S. Trotzky, Y.-A. Chen, and I. Bloch. Experimental realization of strong effective magnetic fields in an optical lattice. *Phys. Rev. Lett.*, 107:255301, Dec 2011.

[147] Ehud Altman and Assa Auerbach. Oscillating superfluidity of bosons in optical lattices. *Physical review letters*, 89(25):250404, 2002.

[148] Anatoli Polkovnikov, Krishnendu Sengupta, Alessandro Silva, and Mukund Vengalattore. Colloquium: Nonequilibrium dynamics of closed interacting quantum systems. *Rev. Mod. Phys.*, 83:863–883, Aug 2011.

[149] Tim Langen, Thomas Gasenzer, and Jörg Schmiedmayer. Prethermalization and universal dynamics in near-integrable quantum systems. *Journal of Statistical Mechanics: Theory and Experiment*, 2016(6):064009, 2016.

[150] Jens Eisert, Mathis Friesdorf, and Christian Gogolin. Quantum many-body systems out of equilibrium. *Nature Physics*, 11(2):124, 2015.

[151] Rahul Nandkishore and David A. Huse. Many-body localization and thermalization in quantum statistical mechanics. *Annu. Rev. Condens. Matter Phys.*, 6(1):15–38, 2015.

[152] Satoshi Uetake. Private Communication, 2015.

[153] H. Hara. Degenerate mixture of alkali and alkaline-earth-like atoms. *Ph. D thesis, Kyoto University*, 2013.

[154] Stefan Trotzky, Yu-Ao Chen, Andreas Flesch, Ian P. McCulloch, Ulrich Schollwöck, Jens Eisert, and Immanuel Bloch. Probing the relaxation towards equilibrium in an isolated strongly correlated one-dimensional bose gas. *Nature Physics*, 8(4):325, 2012.

[155] Alexander Petrov, Eite Tiesinga, and Svetlana Kotochigova. Anisotropy-induced Feshbach resonances in a quantum dipolar gas of highly magnetic atoms. *Phys. Rev. Lett.*, 109:103002, Sep 2012.

[156] Arko Roy and Kush Saha. Interacting bosons in two-dimensional lattices with localized dissipation. *arXiv preprint arXiv:1808.06505*, 2018.

[157] K. Aikawa, A. Frisch, M. Mark, S. Baier, A. Rietzler, R. Grimm, and F. Ferlaino. Bose-Einstein condensation of erbium. *Phys. Rev. Lett.*, 108:210401, May 2012.

[158] Svetlana Kotochigova and Alexander Petrov. Anisotropy in the interaction of ultracold dysprosium. *Physical Chemistry Chemical Physics*, 13(42):19165–19170, 2011.

[159] Albert Frisch, Michael Mark, Kiyotaka Aikawa, Francesca Ferlaino, John L Bohn, Constantinos Makrides, Alexander Petrov, and Svetlana Kotochigova. Quantum chaos in ultracold collisions of gas-phase erbium atoms. *Nature*, 507(7493):475, 2014.

[160] Georgios Kordas, Dirk Witthaut, and Sandro Wimberger. Non-equilibrium dynamics in dissipative Bose-Hubbard chains. *Annalen der Physik*, 527(9-10):619–628, 2015.

[161] T. D. Kühner and H. Monien. Phases of the one-dimensional Bose-Hubbard model. *Phys. Rev. B*, 58:R14741–R14744, Dec 1998.

[162] M. Iskin. Route to supersolidity for the extended Bose-Hubbard model. *Phys. Rev. A*, 83:051606, May 2011.

[163] Dmitry L. Kovrizhin, G. Venketeswara Pai, and Subhasis Sinha. Density wave and supersolid phases of correlated bosons in an optical lattice. *EPL (Europhysics Letters)*, 72(2):162, 2005.

[164] Konstantin V. Krutitsky and Patrick Navez. Excitation dynamics in a lattice bose gas within the time-dependent Gutzwiller mean-field approach. *Phys. Rev. A*, 84:033602, Sep 2011.

[165] E. Altman, A. Polkovnikov, E. Demler, B. I. Halperin, and M. D. Lukin. Superfluid-insulator transition in a moving system of interacting bosons. *Phys. Rev. Lett.*, 95:020402, Jul 2005.

[166] Takuya Saito, Ippei Danshita, Takeshi Ozaki, and Tetsuro Nikuni. Detecting the superfluid critical momentum of bose gases in optical lattices through dipole oscillations. *Phys. Rev. A*, 86:023623, Aug 2012.

[167] Michiel Snoek and Walter Hofstetter. Two-dimensional dynamics of ultracold atoms in optical lattices. *Phys. Rev. A*, 76:051603, Nov 2007.

[168] Ulf Bissbort, Sören Götze, Yongqiang Li, Jannes Heinze, Jasper S. Krauser, Malte Weinberg, Christoph Becker, Klaus Sengstock, and Walter Hofstetter. Detecting the amplitude mode of strongly interacting lattice bosons by Bragg scattering. *Phys. Rev. Lett.*, 106:205303, May 2011.

[169] Michiel Snoek. Rigorous mean-field dynamics of lattice bosons: Quenches from the Mott insulator. *EPL (Europhysics Letters)*, 95(3):30006, 2011.

[170] J Hecker Denschlag, JE Simsarian, H Häffner, C McKenzie, A Browaeys, D Cho, Kristian Helmerson, SL Rolston, and William D Phillips. A Bose-Einstein condensate in an optical lattice. *Journal of Physics B: Atomic, Molecular and Optical Physics*, 35(14):3095, 2002.

[171] Ryuta Yamamoto, Jun Kobayashi, Takuma Kuno, Kohei Kato, and Yoshiro Takahashi. An ytterbium quantum gas microscope with narrow-line laser cooling. *New Journal of Physics*, 18(2):023016, 2016.

Acknowledgements

本論文は、京都大学量子光学研究室において行った研究をまとめたものです。この場を借りて、本研究に携わってこられた方々に厚く御礼申し上げます。

高橋義朗教授には、修士 1 年から 5 年間にわたりご指導を頂きました。数え切れないほど多くのミーティングの場を設けていただき、そのたびに有益な議論をすることができたおかげで、研究を前に進めることができ、今日の博士課程修了を迎えることができました。ミーティングの中での実験結果に対する鋭いご指摘と次のステップの提案、物理の考察が無ければ、このような研究を成し得ることはできませんでした。また、論文執筆の際には、どのようにまとめればよいか分からずなかなか原稿を完成させない私に、適切な助言をして頂き、非常に助けられました。

中島秀太特定准教授には、私が研究室に入って右も左も分からないところからご指導を頂き、研究のあらゆる面でお世話になりました。実験の際には、装置の扱い方やトラブルの対処法に加えて、データ取得の際の見当の付け方など、実験をする際の心構えのようなものも教えていただきました。実験を始めたころ、私がつまらないミスをしても、失敗したという強い記憶が今後のミスを防ぐ、と励ましていただいたことが非常にありがたく印象に残っています。また、何か質問をするたびに、ホワイトボードの前で基礎的な部分から丁寧に解説をしていただき、質問の内容の何倍もの知識を提供していただきました。幅広い知識と経験、物理の理解の深さ、そして粘り強く研究を進める姿勢に刺激を受けました。その他にも、M1 の頃から研究会に誘っていただき量子エレクトロニクス分野の多くの方とのコミュニケーションを促していただいたことも、今思うと非常に貴重な経験だったと感じています。

高須洋介助教には、実験結果の解析や装置の使い方に関してご指導いただきました。特に、装置のインストールや水漏れトラブルなど、あまり頻度の高くないイベントについて、その長年の経験から適切な対処法を教えていただき、非常に助けられました。また、研究室内の備品の管理や計算機係の仕事に関しても、その時々にアドバイスを下さり、お世話になりました。

段下一平現近畿大学准教授には、本研究の理論的な解析において大変お世話になりました。散逸のあるボース・ハバード系という、私個人の力では取り扱いの困難な物理系に対して、明快に理論を組み上げていただき、実験と理論の比較を詳細に行うことができ、実験結果に対して深い考察を行うことができました。また、何度も議論を行う過程で、実験で観測された現象の物理的なメカニズムを妥協無く検証する姿勢を学びました。私の度重なる数値計算のお願いや要領を得ない質問に対応していただき、ありがとうございました。

秘書の寺川公美子さんには、旅費や物品購入の手続き等をしていただき、非常に助かりました。寺川さんのおかげで研究をスムーズに進めることができました。また、季節のイベントの準備をしていただいたり、お菓子を下さったりと、日常に癒しを提供していただきました。ありがとうございました。

その他にも、研究を進める中で多くの方のお世話になりました。ウィークリー・ミー

ティングでの発表内容や研究についての質問に対応し、助言をしていただき、議論につきあっていただいた全ての人に感謝申し上げます。また、多くの方に雑談につき合わせてしまい、皆様の時間を奪ってしまったことを申し訳なく思っております。特に山下和也さん、奥野大地君、高田佳弘君とはQGMグループで一緒に実験をさせていただき、有益な議論に加えて多くのくだらない話を聞いていただきました。皆さんの精力的に実験を進めていく姿は、常に自分自身の研究への姿勢を律してきました。ありがとうございました。

研究室外では、とりわけ同期の高三和晃君、草場哲君、今村征央君の3人にお世話になりました。理論と実験の垣根を超えてお互いの研究について話をすることで、物理の幅広い世界を知ることができ、高いモチベーションを保ちつつ研究を進めることができました。また、物理以外にも、人文・社会・文化などありとあらゆるテーマで豊かな議論ができたことは、息抜きになると同時に良い刺激になりました。

また、博士課程在学中、日本学術振興会から経済的な援助を頂き、集中して研究に取り組むことができたことを深く感謝致します。

最後に、博士課程修了まで私を見守ってくれた家族に心より感謝いたします。